PROBING THE MICROSTRUCTURE OF YIELD-STRESS FLUIDS USING MULTIPLE PARTICLE TRACKING

FELIX K. OPPONG

Probing the Microstructure of Yield-Stress Fluids Using Multiple Particle Tracking

by

© Felix K. Oppong

B.Sc.(Hons.) (University of Cape Coast, Cape Coast, Ghana) 2001

A thesis submitted to the
School of Graduate Studies
in partial fulfilment of the
requirements for the degree of
Master of Science

Department of Physics and Physical Oceanography

Memorial University of Newfoundland

(March, 2005)

St. John's Newfoundland

Abstract

We have studied the microstructure of carbopol, a polymer, and laponite, a colloidal clay suspension, using multiple particle tracking and fluorescence video microscopy. From measurements of the positions of fluorescent spheres suspended in these fluids over a period of time, we obtain information about the microscopic properties of the fluids.

For carbopol at low concentrations, the spheres diffuse freely in the fluid without any hindrance and the fluid environment is homogeneous. At intermediate concentrations, as the fluid gels, the environment becomes heterogeneous and the motion of the spheres becomes subdiffusive as the fluid structure starts to restrict their motion. At higher concentrations, stiffer gels are formed, the mean square displacement is low and the spheres are almost completely trapped by the fluid structure. From our data we estimate the length scales of the structures in the fluid to be on the order of 1 to 2 μm.

The properties of laponite depend on both age and concentration. At small age and low concentrations, the motion of the spheres is diffusive and the fluid is homogeneous. At intermediate ages and concentrations, the motion is subdiffusive at short lag times but close to diffusive at longer lag times, which may be a signal of the sol-gel transition. At higher ages and concentrations the spheres are completely confined by the stiff gels formed and the fluid environment is heterogeneous. We were unable to determine a characteristic length scale for laponite, probably due to its

fractal structure.

Contents

List of Tables

List of Figures

Acknowledgements

I am highly indebted to my supervisor, Dr. John de Bruyn, for the opportunity, the great working environment, and his great patience in guiding me through this research.

Special thanks go to the Canadian Space Agency for funding this research. The Faculty of Medicine, Memorial University of Newfoundland allowed the use of their fluorescence microscope for this research. Mr. Mike Goldsworthy at the Faculty of Medicine, the microscope lab supervisor, offered a lot of assistance in the course of the research and his help is very much appreciated. Special thanks also go to Dr. Eric Weeks of Emory University for his very useful discussions and suggestions during the data analysis stage of the research.

I deeply appreciate the loving care and encouragement of my parents, Sam and Margaret Oppong. Without them, it would have been impossible to make it this far. My special thanks go to my fiancee, Miss Joyce Badu-Nkansah, for her love, encouragement and great patience in coping with the long period of loneliness. I thank my siblings Daniel, Priscilla, Anna, and Andrew for their friendship and encouragement.

Chapter 1

Introduction

1.1 Complex Fluids and their Flow Properties

Fluids are a subset of the phases of matter that includes liquids, gases, plasmas and to some extent plastic solids. Fluids have the general property that they can be deformed and made to flow on the application of sufficient force. The classification of fluids is mostly based on their response to an applied force [2]. In Newtonian fluids, response to an applied force or stress is linear and the viscosity of the fluid is independent of the shear rate (see Fig. 1.1). Examples of Newtonian fluids include simple fluids such as water, ethanol and glycerine. On the other hand, non-Newtonian or complex fluids have a non-linear response to an applied stress. By definition, complex fluids are characterized by structural features and relaxations that vary over a wide range of length and time scales. The microstructures constituting the fluid are often very sensitive to subtle physical and chemical perturbations. The presence of multiple structure relaxation times contributes to a corresponding variation of the

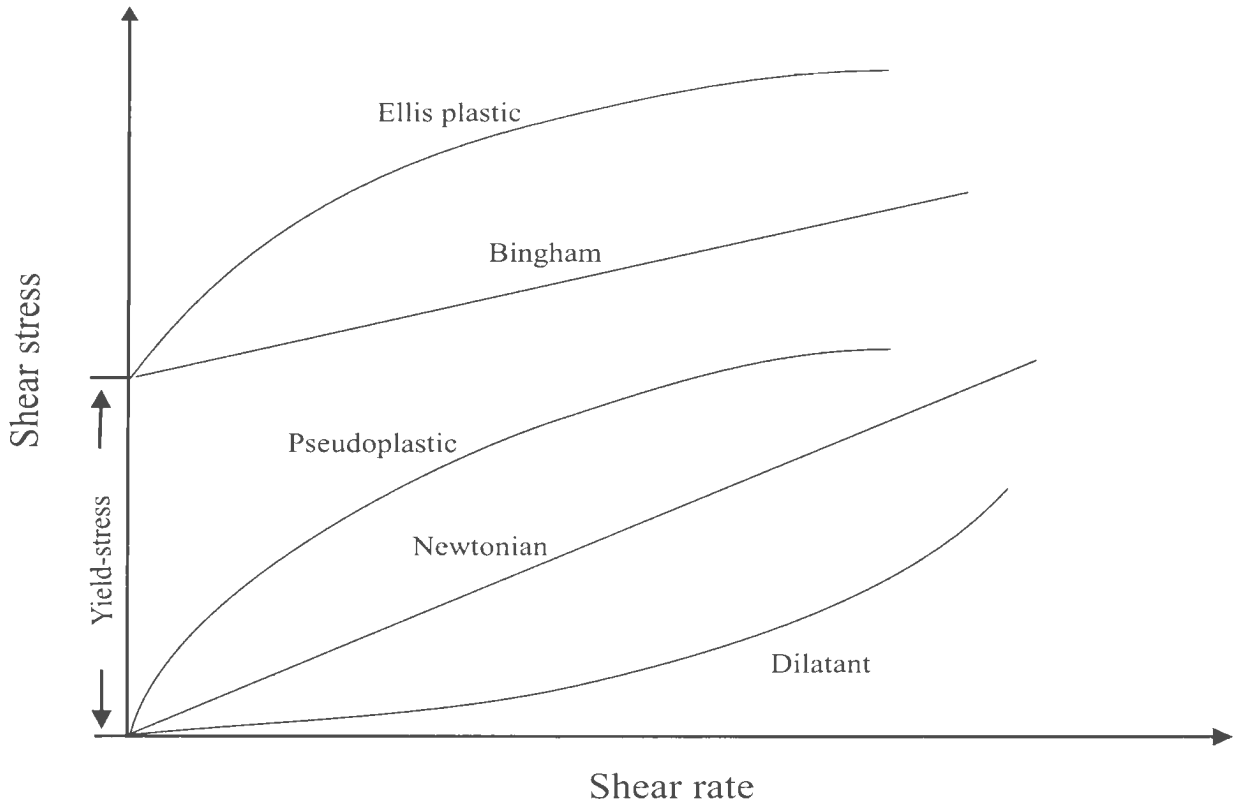

Figure 1.1: Types of flow behaviour in fluids [2].

rheological properties depending on the time scales over which they are measured [3, 4]. Complex fluids typically consist of large dissolved or solvated molecules or suspended particles in a solvent. There can be a wide range of interactions between the molecules or particles themselves and between the molecules or particles and the solvent [2, 5]. Some of the most common interactions include van der Waals, electrostatic, hydrogen bonding and hydrophobic interactions [5].

Complex fluids exhibit different types of flow behaviour depending on the structural features and the type of interactions inherent in the fluid. Figure 1.1 shows some of the flow behaviour observed in complex fluids. Dilatant behaviour occurs in suspensions that contain high concentrations of closely packed solids. In such materials, the viscosity increases as the shear rate is increased. Dilatant fluids are therefore referred to as shear-thickening fluids. Corn starch is an example of a dilatant fluid. In contrast, for pseudoplastic and Ellis plastic fluids, viscosity decreases with increasing shear rate. Examples of pseudoplastic fluids includes solutions of guar gum and cellulosic thickeners. Carbopol, which is one of the materials studied in this thesis, is an example of Ellis plastic. This type of flow behaviour is referred to as shear thinning. Certain types of fluids will only flow when the shear stress exceeds a critical value, known as the yield stress. Such fluids are referred to as yield-stress fluids. Bingham plastic and Ellis plastic materials are examples of yield-stress fluids [2]. Common examples of yield-stress fluids include mayonnaise, ketchup and toothpaste.

1.2 Gelation, Polymers and Colloids

1.2.1 Gelation in Complex Fluids

Two types of complex fluids that are investigated in this research are polymers and colloids. They both have the ability to form gels, and during the process of gelation there is a rapid change in the flow behaviour of these fluids. The conversion of a liquid to a disordered solid by the formation of a network of chemical or physical bonds between the molecules or particles comprising the liquid is referred to as gelation [5]. The liquid-like precursor of a gel is referred to as a sol.

1.2.2 Polymers

A polymer may be defined as a long repeating chain of atoms, formed through the linkage of many molecules called monomers. The monomers can be identical or different. Polymers formed out of identical monomers are called homopolymers, while those formed from different monomers are referred to as copolymers [5].

Gelation in polymers occurs as a result of intermolecular association leading to the formation of a network. Polymeric gels often show strong viscoelastic effects such as shear thinning or time-dependent rheology. Their rheology is also very dependent on the concentration of the polymers. At high concentrations, polymeric gels become extremely viscous. Polymers have a critical molecular weight beyond which there is a steep increase in the viscosity. Such an increase is normally due to chain

entanglements in the fluid leading to increased interactions [5].

1.2.3 Colloids

Colloids are microscopic particles, typically in the size range of 10 nm to 5 μm in diameter [6]. Colloidal suspensions consist of colloidal particles suspended in another medium. These can take many forms, as each of the colloidal particles or the suspending medium may be gas, liquid or solid.

Interparticle interactions play a key role in influencing the flow behaviour of colloidal suspensions. Some of the most common interactions are steric repulsion, van der Waals attraction and electrostatic repulsion or attraction. In the presence of attractive interactions, the particles aggregate to form a gel. Gelation in colloidal suspensions may be reversible or irreversible. Colloidal suspensions with reversible gel transitions are also known to be yield-stress fluids [6, 7] .

1.3 Multiple Particle Tracking

Multiple particle tracking (MPT), is a recently developed technique for studying the microscopic structure and dynamics of fluids [8, 9, 10, 11, 12, 13, 14]. MPT involves the passive observation of probe particles suspended in the fluid of interest. In this technique, the probe particles are not manipulated with any external forces. Their motion is simply due to the thermal fluctuations of suspending fluid [8].

The most important quantity that can be extracted from MPT measurements is

the mean square displacement (MSD) of the probe particles. The nature of the MSD will depend on the microenvironments probed by the particles. For fluids that are inhomogeneous on the length scale of the probe particle, it is possible to directly infer from the MSD the nature of the microstructures in the fluid and how they evolve with time. The size of these microstructures can be estimated from the MSD. Local viscoelastic parameters for the fluid can also be calculated from the MSD. For homogeneous fluids, bulk rheological parameters such as the elastic modulus can be extracted from the MSD, depending on the nature of the fluid. Thanks to the recently developed two-point microrheology technique, it is possible to obtain the bulk parameters of an inhomogeneous fluid [15]. Several methods have been developed to calculate the local and bulk viscoelastic parameters of complex fluids from the MSD [4, 9, 13]. It is also possible to obtain further information from the trajectories of individual probe particles.

The main advantage of the MPT technique is that it is possible to study the microstructure of complex fluids while conventional macrorheological techniques give only bulk properties [8, 13]. Another strength of the technique is the fact that, unlike in conventional rheometry, measurements are made without actually deforming the fluid [13, 16]. Wall slip effects, which can be a major problem in macrorheology, are not an issue in MPT. This technique also offers the convenience of using only small volumes of test solutions and is therefore very appropriate in cases where the fluid is scarce or expensive.

There are a number of restrictions on the MPT technique. A major drawback is the fact that the fluid to be studied must be soft enough to allow the probe particles to move detectably as a result of thermal fluctuations. It is therefore very difficult, if not impossible, to study very thick gels with this method [8, 13, 16]. The temporal resolution of the experiments is determined by the frequency at which particle positions can be recorded. This is dependent on the camera and frame grabber used as well as on available computer memory. Another operational limit is the fact that when the viscosity of the suspending fluid is low, particles can diffuse so fast that the average residence time in the depth of focus of the optical system is too short [16]. The time that a particle will stay in focus is estimated by [16]

$$t_{\max} = \frac{3\pi a d_f^2 \eta}{2k_B T} \tag{1.1}$$

where a is the radius of the particle, d_f is the depth of focus, η is the viscosity of the fluid, k_B is the Boltzmann constant and T is the temperature. The restriction posed by the limited residence time becomes pronounced when small particles are suspended in low viscosity fluids.

1.4 Summary of Previous Work

The MPT technique has been used to study a number of complex systems. For example, Wong et al. have used this technique to study anomalous diffusion and microstructure in entangled F-actin networks [14]. Weeks et al. have investigated

cage effects near the glass transition in hard sphere colloids using MPT [17, 18]. The mechanical properties of living cells have been studied with MPT by Tseng et al. [19]

Extensive theoretical work has been done on diffusion in complex fluids. Several models have been developed to describe various types of motion in complex fluids. Using Monte Carlo simulations, Saxton has studied anomalous diffusion due to binding [20] and obstacles [21]. Other theoretical work on diffusion in complex fluids includes Refs. [10, 11, 22, 23, 24].

The rheological properties of carbopol have been extensively studied [25, 26, 27, 28, 29, 30]. However, as far as we know, microstructural studies of carbopol have been very limited. The rheological properties of three types of carbopol hydrogels (ETD2001, ETD2020 and ETD2050) have been studied by Hernández et al. [31] They found that ETD 2050 possesses the most shear-thinning character of the three. Kim et al. studied the rheology and microstructure of carbopol 941 [32]. They concluded from their cryoscanning electron microscopy measurements that the microstructure of carbopol was dependent on the concentration of the polymer in solution. At low concentrations, very thin physically entangled fibers were observed. Highly-cross linked honeycomb-like structures were observed at higher concentrations. The properties of carbopol, which makes it a model for the study of yield-stress fluids, have been investigated by Curran et al. [33].

The details of the microstructure of laponite gels remain a matter of debate. Pignon et al. performed static light scattering experiments and found a correlation

between the fractal dimension of the gel and the yield-stress [34]. This has been disputed by Bonn et al. [35] and Abou et al. [36]. Kroon et al. have used both static and dynamic light scattering to study the transition in time from fluid-like sol to solid-like gel in laponite [1, 37]. They observed that gelation in laponite occurs as a result of reorientation of the charged colloidal particles. Similar results for the aging process in laponite have been reported by Willenbacher et al. [38] and Bonn et al. [36, 39]. From rheological measurements Ramsay concluded that the development of elastic behaviour in laponite during the gelation process arises from osmotic swelling and the formation of an equilibrium structure due to electrostatic repulsion between individual clay particles [40].

1.5 Motivation and Scope

Many complex materials that are encountered in everyday life derive their macroscopic flow behaviour from their structure on a microscopic length scale [9]. However, little is known about the microscopic structures of these materials in general [8]. Though the phenomenon of yield-stress is well known, a quantitative understanding of the physical processes behind it is still lacking.

The goal of this research was to study the micron-scale structure of some yield-stress fluids using multiple particle tracking and fluorescence video microscopy. Our results will contribute to a better understanding of yield-stress fluids in general.

Two types of complex fluids are considered in this work: carbopol, which is a

polymer, and laponite, a colloidal clay suspension. These fluids gel at sufficiently high concentrations. The properties of carbopol are studied as a function of concentration and probe particle size. Laponite, on the other hand, is studied as a function of both concentration and age as the gelation process proceeds.

In Chapter 2, a theoretical overview of Brownian motion and diffusion in complex fluids is presented. Chapter 3 is dedicated to a detailed description of the experimental materials and methods. The results obtained for carbopol and laponite are presented and discussed in Chapters 4 and 5 respectively. Finally, a summary of our findings and our conclusions are presented in Chapter 6.

Chapter 2

Theory

2.1 Brownian Motion

2.1.1 Historical Background

When powdered charcoal is sprinkled on the surface of alcohol and viewed under a microscope, the charcoal particles move about randomly. This motion is due to the alcohol molecules colliding with the larger charcoal grains. Jan Ingenhauz, who is best known as the discoverer of photosynthesis, was the first to report this observation in 1785. This type of random motion was named after Robert Brown who published on this subject in 1828 after an extensive investigation. In 1905, Albert Einstein gave a mathematical interpretation of this motion and argued that it was direct evidence for the atomic nature of matter. Einstein was able to determine the mean square displacement (MSD) of a Brownian particle in terms of Avogadro's number. Jean Perrin won the Nobel Prize in 1926 for determining Avogadro's number using this

method [41, 42, 43].

2.1.2 Random Walks and Brownian Motion

A Random walk is a simple model stochastic process that involves successive steps in random directions. Typically, each step in the walk is of constant length but the direction of the walk from one point to the next is completely random and there is no preferred direction. Brownian motion is an example of a random walk [43, 44].

We let l be the step-length of a particle undergoing a random motion. We let the origin be at $\mathbf{r}_0 = 0$. After N steps, the particle will be at the point $\mathbf{r}_N$. After $N+1$ steps, the position of the particle will be

$$\mathbf{r}_{N+1} = \mathbf{r}_N + l\mathbf{n}. \tag{2.1}$$

where $\mathbf{n}$ is the direction of the $(N+1)$th step, that is, the direction of the step taken by the particle located at the point $\mathbf{r}_N$.

Since the direction of each step is random,

$$\langle \mathbf{n} \rangle = 0, \tag{2.2}$$

where the averaging is over all steps. As a result, if we take the average of both sides in Eq. (2.1), we have

$$\langle \mathbf{r}_{N+1} \rangle = \langle \mathbf{r}_N \rangle . \tag{2.3}$$

Eq. (2.3) implies that

$$\langle \mathbf{r}_N \rangle = \langle \mathbf{r}_{N-1} \rangle = ... = \langle \mathbf{r}_0 \rangle = 0,$$

hence

$$\langle \mathbf{r}_N \rangle = 0 \tag{2.4}$$

for all N.

On the other hand, the average of the squared displacement of a particle undergoing a random walk is not zero but grows linearly with time, that is,

$$\left\langle \mathbf{r}^2 \right\rangle = \xi t, \tag{2.5}$$

where ξ is a proportionality constant. Based on assumptions involving the atomic nature of matter, Einstein was able to express the proportionality constant in Eq. (2.5) in terms of other quantities derived from kinetic theory [41, 44]. This is described in Sec. 2.1.4 and 2.1.6 below.

2.1.3 The Gaussian Distribution and the Central Limit Theorem

The Gaussian or normal distribution function is a probability density function of a random variable. It represents the likelihood of occurrence of each value of the random variable x and is given by by

$$f(x) = \frac{1}{\sigma\sqrt{2\pi}} e^{-(x-\mu)^2/2\sigma^2}, \tag{2.6}$$

where μ is the mean and σ is the standard deviation of the distribution [43, 44].

The central limit theorem (CLT) expresses the fact that any sum of many statistically independent random variables is normally distributed. This important theorem has made it possible to apply the Gaussian distribution function to describe many random processes [44].

As discussed in Sec. 2.1.2, the displacement of a particle performing Brownian motion is purely random and so by virtue of the CLT, can be described by the Gaussian distribution function. When a Gaussian is fitted to the histogram of displacements of a Brownian particle, the mean of the distribution μ measures the net drift in the motion of the particles [45]. The standard deviation is related to the self-diffusion coefficient D of the particle by [43, 44, 45]

$$\sigma(\tau) = \sqrt{2D\tau} \tag{2.7}$$

in one dimension. τ is the lag time between measurements of the displacement.

2.1.4 The Mean Square Displacement in Terms of the Diffusion Constant

Let $n_1(x,t)$ be the mean number of molecules or particles per unit volume located at time t near the position x. The one dimensional diffusion equation for $n_1(x,t)$ is given by

$$\frac{\partial n_1}{\partial t} = D\frac{\partial^2 n_1}{\partial x^2}. \tag{2.8}$$

D is the self-diffusion constant [44].

We now seek to calculate the mean square displacement of a particle in terms of D based on Eq. (2.8). Conservation of the total number of particles requires that

$$\int_{-\infty}^{\infty} n_1(x,t)\,dx = N_1 \tag{2.9}$$

where N_1 is the total number of labeled particles per unit area. By definition,

$$\left\langle x^2 \right\rangle = \frac{1}{N_1}\int_{-\infty}^{\infty} x^2 n_1(x,t)\,dx. \tag{2.10}$$

Multiplying Eq. (2.8) by x^2 and integrating over x, we have

$$\int_{-\infty}^{\infty} x^2 \frac{\partial n_1}{\partial t}dx = D\int_{-\infty}^{\infty} x^2 \frac{\partial^2 n_1}{\partial x^2}dx. \tag{2.11}$$

Using Eq. (2.10) the left side of Eq. (2.11) becomes

$$\int_{-\infty}^{\infty} x^2 \frac{\partial n_1}{\partial t}dx = \frac{\partial}{\partial t}\int_{-\infty}^{\infty} x^2 n_1 dx = N_1 \frac{\partial}{\partial t}\left\langle x^2 \right\rangle. \tag{2.12}$$

The right side of Eq. (2.11) can be simplified by successive integration by parts as follows:

$$\begin{aligned}
\int_{-\infty}^{\infty} x^2 \frac{\partial^2 n_1}{\partial x^2}dx &= \left[x^2 \frac{\partial n_1}{\partial x}\right]_{-\infty}^{\infty} - 2\int_{-\infty}^{\infty} x \frac{\partial n_1}{\partial x}dx \\
&= 0 - 2\left[x n_1\right]_{-\infty}^{\infty} + 2\int_{-\infty}^{\infty} n_1 dx \\
&= 0 + 2N_1,
\end{aligned} \tag{2.13}$$

where we have assumed that as $|x|$ approaches infinity, both n_1 and $(\partial n_1/\partial x)$ approach zero. Using Eqs. (2.12) and (2.13), Eq. (2.11) becomes

$$\frac{\partial}{\partial t}\left\langle x^2 \right\rangle = 2D. \tag{2.14}$$

Integrating both sides of Eq. (2.14) with respect to t and setting $\left\langle x\left(0\right)^{2}\right\rangle = 0$, we have

$$\left\langle x^{2}\right\rangle = 2Dt, \tag{2.15}$$

which gives the MSD in terms of the self-diffusion constant.

Similarly, starting with the three dimensional diffusion equation

$$\frac{\partial n_{1}}{\partial t} = D\left(\frac{\partial^{2} n_{1}}{\partial x^{2}} + \frac{\partial^{2} n_{1}}{\partial y^{2}} + \frac{\partial^{2} n_{1}}{\partial z^{2}}\right) \tag{2.16}$$

will lead to $\left\langle r^{2}\right\rangle = 6Dt$, and in general,

$$\left\langle r^{2}\right\rangle = 2dDt, \tag{2.17}$$

where d is the dimensionality of the motion.

2.1.5 The Langevin Equation

For simplicity, we consider here the motion of a particle in one dimension. We consider a particle of mass m whose center-of-mass coordinate at time t is $x\left(t\right)$ and with velocity $v = dx/dt$. This particle is immersed in a fluid of temperature T. We define $F\left(t\right)$ as the net force acting on the particle due to interaction with the fluid in which it is suspended. The particle may also be subject to external forces, for example due to gravity or an electric field, and we denote such forces by $\zeta\left(t\right)$.

From Newton's second law of motion, we have

$$m\frac{dv}{dt} = F\left(t\right) + \zeta\left(t\right). \tag{2.18}$$

$F(t)$ is a fluctuating force which depends on the positions of very large number of atoms of the suspending medium, which are in constant motion [44]. From equation Eq. (2.18), it follows that if $F(t)$ fluctuates with time, then v must also fluctuate in time. We let $\bar{v}$ be the ensemble average of the velocity. $\bar{v}$ is a more slowly varying function of time than v itself, and we can write

$$v = \bar{v} + v', \tag{2.19}$$

where v' denotes the part of v which fluctuates rapidly with time. v' must as often be positive as negative and its mean vanishes.

$\bar{v}$ is important because it can describe the behaviour of the particle over a long period of time. To investigate its dependence on time, we integrate Eq. (2.18) over some time interval τ' which is small on macroscopic scale but long compared to the time scale of the fluctuations of $F(t)$. Then we have

$$m\left[v\left(t+\tau'\right)-v\left(t\right)\right]=\zeta\left(t\right)\tau'+\int_{t}^{t+\tau'}F\left(t'\right)dt', \tag{2.20}$$

where we have assumed that $\zeta(t)$ is varying slowly enough that it changes by a negligible amount during the time τ'. The last integral term in Eq. (2.20) must be small since $F(t)$ changes in sign many times in the time τ'. This implies that the slowly varying part of v must be due to only the slowly varying external force, $\zeta(t)$, and one may write

$$m\frac{d\bar{v}}{dt}=\zeta\left(t\right), \tag{2.21}$$

but this approximation is an over-simplification which fails to describe the whole physical situation. If we suppose that the external force $\zeta(t)$ is zero, the only force acting on the particle will then be $F(t)$. $F(t)$ must be such that if $\bar{v} \neq 0$ at some initial time, it causes $\bar{v}$ to gradually approach the equilibrium value of $\bar{v} = 0$. Clearly, Eq. (2.21) fails to predict this behaviour and the definition of $F(t)$ must be modified to reflect this. $F(t)$ must itself be affected by the motion of the particle such that it contains a slowly varying part $\bar{F}$ tending to restore the particle to equilibrium. It follows that $\bar{F}$ must be some function of $\bar{v}$ which is such that $\bar{F}(\bar{v}) = 0$ at equilibrium when $\bar{v} = 0$ [44]. Consequently, $F(t)$ becomes

$$F(t) = \bar{F} + F' \tag{2.22}$$

where as before, F' is the rapidly fluctuating part of F and has a vanishing average.

Provided that $\bar{v}$ is not too large, $\bar{F}(\bar{v})$ can be expanded in a power series in $\bar{v}$, whose first non-vanishing term must be linear in $\bar{v}$. To first order in $\bar{v}$, $\bar{F}$ therefore has the general form

$$\bar{F} = -\beta\bar{v}, \tag{2.23}$$

where β is some positive constant called the friction constant. The negative sign indicates that $\bar{F}$ acts in such a direction that it reduces $\bar{v}$ to zero.

The slowly varying part of Eq. (2.18) then becomes

$$m\frac{d\bar{v}}{dt} = \zeta + \bar{F} = \zeta - \beta\bar{v}. \tag{2.24}$$

Including v' and F', the rapidly fluctuating parts of $v(t)$ and $F(t)$, in Eq. (2.24), we get

$$m\frac{dv}{dt} = \zeta - \beta v + F'(t). \tag{2.25}$$

Here $\beta\bar{v} \approx \beta v$ with negligible error, since $\beta v'$ can be neglected compared to the more dominant fluctuating term $F'(t)$. Eq. (2.25) is the Lagenvin equation which describes the behaviour of the Brownian particle if all the initial conditions are given [44].

2.1.6 The Stokes-Einstein Relation

In the absence of external forces, Eq. (2.25) becomes

$$m\frac{dv}{dt} = -\beta v + F'(t). \tag{2.26}$$

We consider the particle as a macroscopic sphere of radius a moving with velocity v through a fluid of viscosity η. Then from macroscopic hydrodynamic considerations, we have a frictional force $-\beta v$ where

$$\beta = 6\pi\eta a. \tag{2.27}$$

Eq. (2.27) is referred to as Stokes's Law.

To calculate the MSD ($\langle x^2 \rangle$), we make use of Eq. (2.26) under conditions of thermal equilibrium and note that the mean displacement $\langle x \rangle$ of the particle vanishes as discussed in Sec. 2.1.2. Setting $v = \dot{x}$ and $dv/dt = d\dot{x}/dt$ and multiplying both sides of Eq. (2.26) by x we get

$$mx\frac{d\dot{x}}{dt} = m\left[\frac{d}{dt}(x\dot{x}) - \dot{x}^2\right] = -\beta x\dot{x} + xF'(t), \tag{2.28}$$

where

$$\frac{d}{dt}\left(x\dot{x}\right) = x\frac{d\dot{x}}{dt} + \dot{x}^2.$$

Taking the ensemble average of both sides of the second equation in Eq. (2.28), we have

$$m\left(\left\langle \frac{d}{dt}\left(x\dot{x}\right)\right\rangle - \left\langle \dot{x}^2\right\rangle\right) = -\beta\left\langle x\dot{x}\right\rangle + \left\langle xF'\left(t\right)\right\rangle. \tag{2.29}$$

But from Sec. 2.1.5, the mean value of the fluctuating force, F' always vanishes irrespective of the values of v and x. Hence x and F' are uncorrelated and $\langle xF'\rangle = \langle x\rangle\langle F'\rangle = 0$. Also from the equipartition theorem, $1/2(m\langle\dot{x}^2\rangle) = 1/2(k_BT)$. Therefore Eq. (2.29) becomes

$$m\left\langle \frac{d}{dt}\left(x\dot{x}\right)\right\rangle - k_BT = -\beta\left\langle x\dot{x}\right\rangle. \tag{2.30}$$

But

$$\left\langle \frac{d}{dt}\left(x\dot{x}\right)\right\rangle = \frac{d}{dt}\left\langle x\dot{x}\right\rangle,$$

so Eq. (2.30) becomes

$$m\frac{d}{dt}\left\langle x\dot{x}\right\rangle = k_BT - \beta\left\langle x\dot{x}\right\rangle. \tag{2.31}$$

Eq. (2.31) is a simple differential equation which can be solved for the quantity $\langle x\dot{x}\rangle = 1/2\left(d\left\langle x^2\right\rangle/dt\right)$, yielding

$$\left\langle x\dot{x}\right\rangle = Ce^{-\gamma t} + \frac{k_BT}{\beta} \tag{2.32}$$

where C is a constant of integration and $\gamma \equiv \beta/m$. γ^{-1} denotes a characteristic time constant of the system.

To calculate the constant C, we assume that each particle in the ensemble starts out at $t = 0$ at position $x = 0$, so that x measures the displacement from the initial position. C must then be such that $0 = C + k_B T/\beta$, hence Eq. (2.32) becomes

$$\langle x\dot{x}\rangle = \frac{1}{2}\frac{d}{dt}\left\langle x^2\right\rangle = \frac{k_B T}{\beta}\left(1 - e^{-\gamma t}\right), \tag{2.33}$$

integrating further we have

$$\left\langle x^2\right\rangle = \frac{2k_B T}{\beta}\left[t - \gamma^{-1}\left(1 - e^{-\gamma t}\right)\right]. \tag{2.34}$$

In the limit $t \gg \gamma^{-1}$, $e^{-\gamma t} \to 0$ and Eq. (2.34) reduces to

$$\left\langle x^2\right\rangle = \frac{2k_B T}{\beta}t. \tag{2.35}$$

As before, the MSD is proportional to time, hence the particle is a diffusing particle executing a random walk. The above result only holds under this condition.

Comparing Eqs. (2.35) and (2.15), the self-diffusion coefficient becomes

$$D = \frac{k_B T}{\beta} \tag{2.36}$$

and from Stokes law, Eq. (2.27), we finally have

$$D = \frac{k_B T}{6\pi\eta a}. \tag{2.37}$$

Eq. (2.37) is referred to as the Stokes-Einstein equation and gives the self-diffusion coefficient of a spherical particle of radius a undergoing Brownian motion in a fluid of viscosity η and temperature T [44, 46].

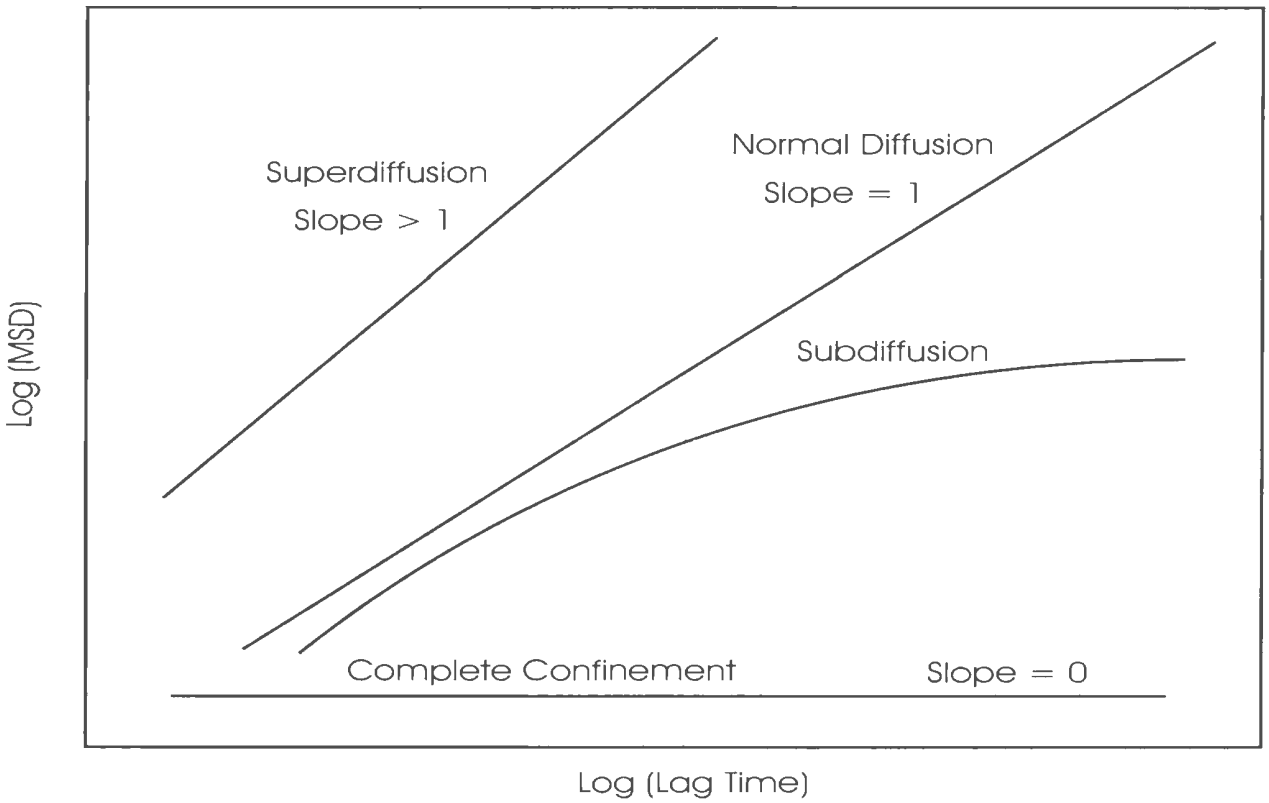

Figure 2.1: A log-log plot of log MSD vs. lag time for the various modes of diffusion in complex fluids.

2.2 Modes of Diffusion in Complex Fluids

In this section, we discuss the various modes of diffusion of a particle moving in a complex fluid. The different modes of diffusion are characterized by the slope of the log-log plot of the MSD, shown schematically in Figure 2.1.

2.2.1 Normal Diffusion

Normal or simple diffusion occurs when a particle moves randomly and freely in a material without any hindrance. This corresponds to normal Brownian motion as

described previously. For this type of motion, the MSD is directly proportional to the lag time, t, and the slope of the log-log plot is one. The plot for a particle undergoing normal diffusion is shown in Figure 2.1.

2.2.2 Subdiffusion

Subdiffusion occurs when the MSD increases more slowly than linearly in time. The slope of a log-log graph of MSD vs lag time in this case is less than one [21, 22, 47, 48, 49]. Subdiffusion is normally encountered in fluids that are inhomogeneous on the length scale of the probe particle. It results from interactions between the particles and other mobile and immobile structures in the fluid [11, 21, 48, 49, 50]. In this case diffusion is no longer a simple homogeneous process but depends on the structures as well as the size of the probe particle. Consequently, the particle motion is not described by a random walk.

The MSD may take several forms depending on the size of the probe particle, as well as the nature, concentration, and length-scale of the fluid structures. Structure within the fluid constrains the motion of a diffusing particle and leads to an MSD that increases more slowly than linearly in time, i.e., $\langle x^2 \rangle \propto t^{\alpha}$ with the diffusive exponent $\alpha < 1$ [10, 11]. In some complex systems, a particle can undergo diffusion in a finite region. At short times, the particles diffuses freely but at long times, its motion is restricted by the structures in the fluid [8, 11]. In that case, $\left\langle x\left(\infty\right)^2 \right\rangle$ which is the MSD value at long times, is proportional to the size of the region accessible to the

particles [8, 11]. If the length scale of the fluid structures is comparable to the size of the particle, the structures act as barriers, confining the motion of the sphere and leading to much lower diffusive exponents. A typical MSD plot for confined motion shows a plateau at long times, as shown in Fig. 2.1. Depending on the size of the probe particle and the barriers, it is possible that the particle may escape from the confining domain over long enough times [11]. In this case, the MSD will begin to increase again.

In subdiffusive motion, the particle displacements are correlated rather than being random. As a result the CLT breaks down, and a non-Gaussian distribution of the displacements is observed [8]. Consequently, the MSD can no longer be described by Eq. (2.35) but by a power law relationship defined by

$$\left\langle x^2 \right\rangle = \frac{2D_\alpha}{\Gamma\left(1+\alpha\right)} t^\alpha \tag{2.38}$$

where D_α is the generalized diffusion coefficient of dimensions $[D_\alpha] = \mu\mathrm{m}^2 s^{-\alpha}$ and Γ is the gamma function. The exponent satisfies $0 < \alpha < 1$ [23, 47]. In addition, α and hence D_α can be functions of lag time. When $\alpha = 1$, Eq. (2.35) is recovered. A generalization of the Stokes-Einstein equation leads to

$$D_\alpha = \frac{k_B T}{m\eta_\alpha} \tag{2.39}$$

which is referred to as the Stokes-Einstein-Smolochowski relation [23]. η_α is the generalized friction coefficient and has dimensions $[\eta_\alpha] = \mathrm{s}^{\alpha-2}$. The mass of the particle is m.

Subdiffusive motion has been reported in a number of materials including amorphous semiconductors [51], proteins and cells in biological systems [12, 50], disordered materials such as glass beads, quartz sand, and naturally occurring sponge [52], and in polymer networks [53].

2.2.3 Diffusion with Flow

Diffusion with flow, also known as superdiffusion, occurs when the diffusive exponent has a value greater than one [11, 12]. This results when the fluid in which the particle is suspended moves with a constant mean velocity $\bar{v}$, so diffusion is superposed on a steady drift or flow. Mobile cells and proteins in biological systems can exhibit this kind of behaviour. Several theoretical models describing anomalous diffusion in biological systems has been developed by Saxton [20, 21, 48, 50]. The MSD in this case is given by

$$\left\langle x^2 \right\rangle = 2Dt + v^2t^2. \tag{2.40}$$

A typical log-log graph of this type of motion is shown in Fig. 2.1.

Chapter 3

Materials and Experimental Methods

3.1 Materials

3.1.1 Carbopol ETD 2050

Carbopol ETD 2050 belongs to the family of carbopol resins which are insoluble polyacrylic acid polymers [25, 32, 33, 54]. They are supplied as dry tightly coiled acidic molecules. The coiled structure of carbopol is shown schematically in Figure 3.1. Once dispersed in water, the molecules begin to hydrate and partially uncoil and in the presence of a neutralizing agent such as NaOH, the dispersion thickens to form a very thick gel [55]. The addition of the base facilitates the formation of hydrogen bonds between the swelling microgels and water both inside and outside the microgels [33]. The thickness of the gel depends on the concentration of the polymer as well as the pH.

The microstructure of the carbopol gel consists of individually gelled concentrated

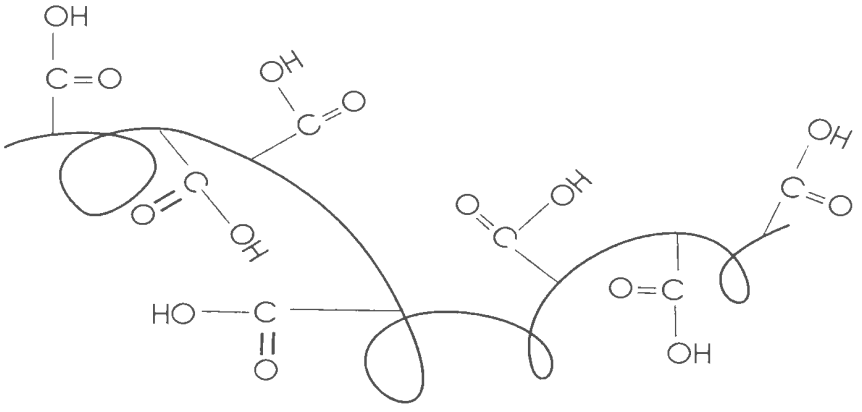

Figure 3.1: The coiled structure of carbopol.

dispersions of highly-cross-linked polymer particles. The exterior of an individual microgel consists of dangling free ends of polymer molecules which interact strongly with similar strands from nearby microgel particles. This leads to the formation of a highly networked microgel structure [54]. The microgel structure of carbopol is shown in a simplified form in Figure 3.2.

The chemical structure and properties of carbopol have a direct influence on its rheology and applications. For example, it has been reported that the shear modulus G° represents interactions between swollen microgel particles and is proportional to the cross-linking density [26, 32]. The rheology also depends on such parameters as temperature and pH. An increase in temperature leads to a decrease in the viscosity while the maximum viscosity is reached in the pH range of 5 to 10 [54, 56]. Carbopol dispersions have been used for many years to improve the rheological properties of some materials [25, 32]. In the pharmaceutical industry, they are regarded as excellent vehicles for drug delivery [28]. They are also used in everyday products such as tile

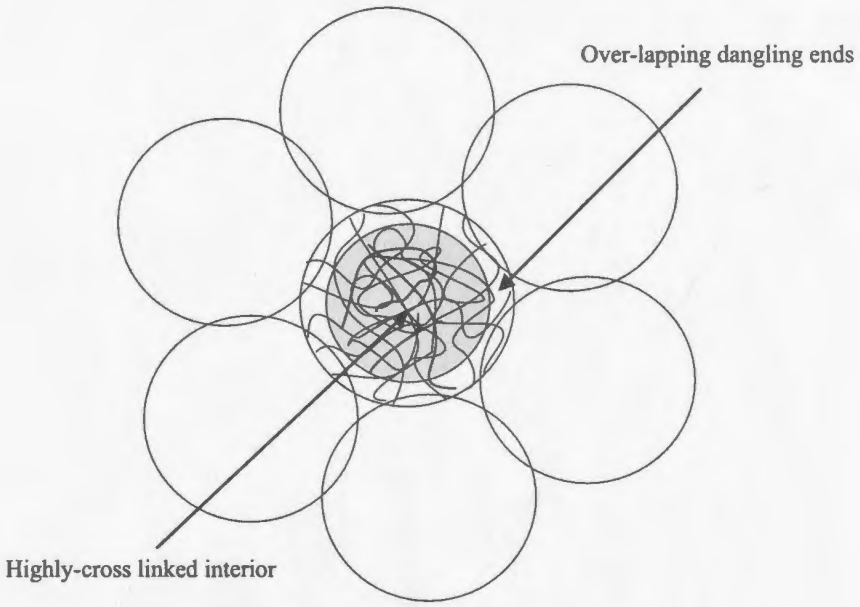

Figure 3.2: Schematic representation of the microgel structure of carbopol.

cleaners and toothpastes [25]. Carbopol has also been used extensively by rheologists as a model for the study of yield-stress fluids because it overcomes many of the complications associated with other fluids of similar properties [33]. For example, it forms a clear gel in water and is therefore very useful for light scattering and video microscopy experiments where clarity of the material is important [25].

3.1.2 Laponite RD

Laponite RD is a synthetic hectorite clay product made of disk-shaped particles. It is formed by combining sodium and magnesium salts together with sodium silicate to give an amorphous precipitate which is partially crystallized at high temperature. It is then filtered, washed, dried and milled to give a finished product of fine white

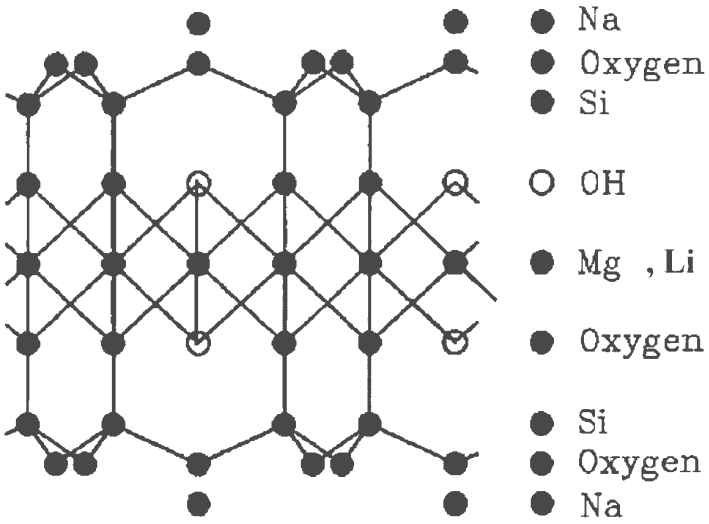

Figure 3.3: The chemical structure of laponite (from Ref. [1]).

powder [57].

Laponite particles are on average 30 nm in diameter and 1-4 nm in height [38]. The chemical formula for this grade of laponite is $Na^{+}_{0.7}[(Si_8Mg_{5.5}Li_{0.3})O_{20}(OH)_4]^{-0.7}$ [57]. The corresponding chemical structure is shown in Figure 3.3. The unit cell consists of two layers of four tetrahedral silicon atoms sandwiching six octahedral magnesium ions. Some of the magnesium ions are substituted by lithium ions. There is a charge deficiency of 0.7 per unit cell. These groups are balanced by twenty oxygen atoms and four hydroxyl groups. The height of the unit cell represents the thickness of the laponite particle. This unit cell is repeated many times in two directions, giving rise to the disk shape of the laponite particles. It has been estimated that a laponite particle contains some 30,000-40,000 unit cells [57].

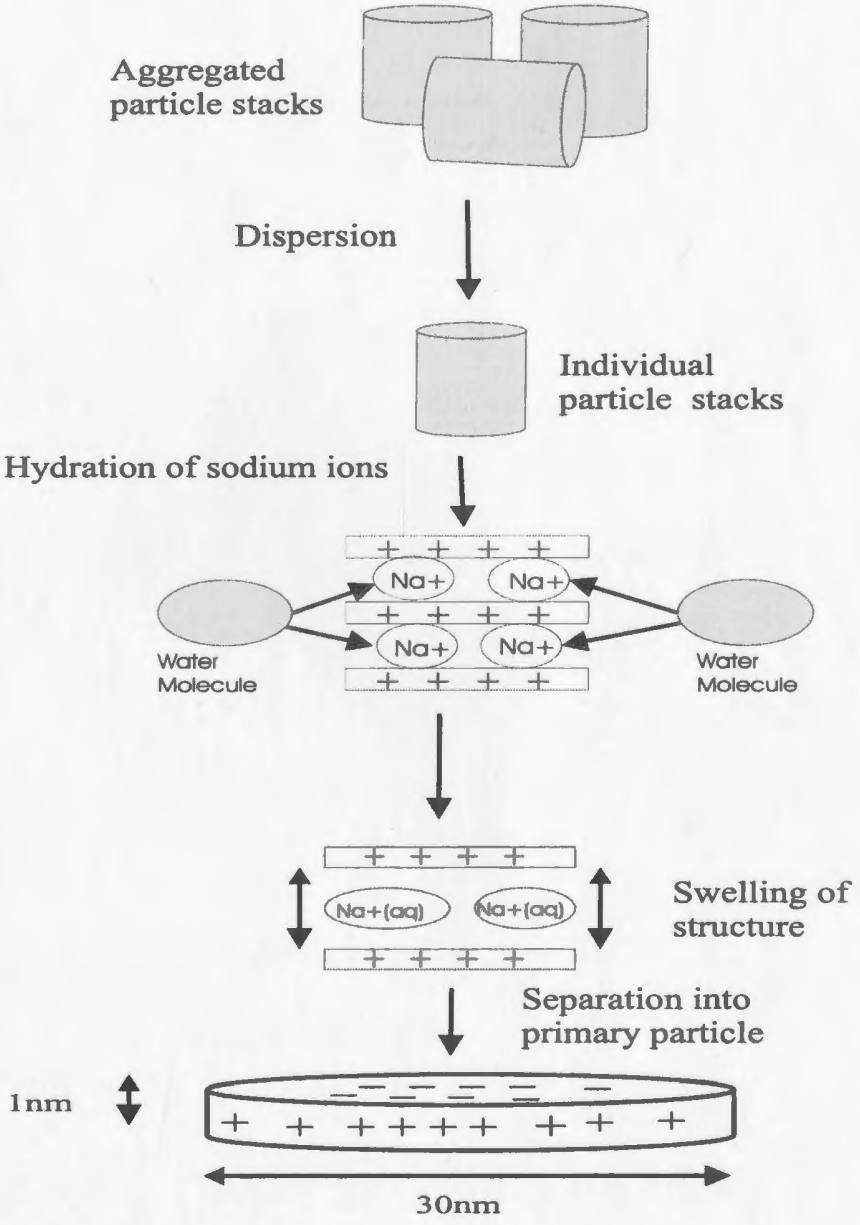

Figure 3.4: A schematic diagram of the hydration process in laponite. The dry aggregated particle stacks get dispersed in water and the sodium ions become hydrated. This leads to a swelling of the structure and separation into the disk-shaped primary laponite particles.

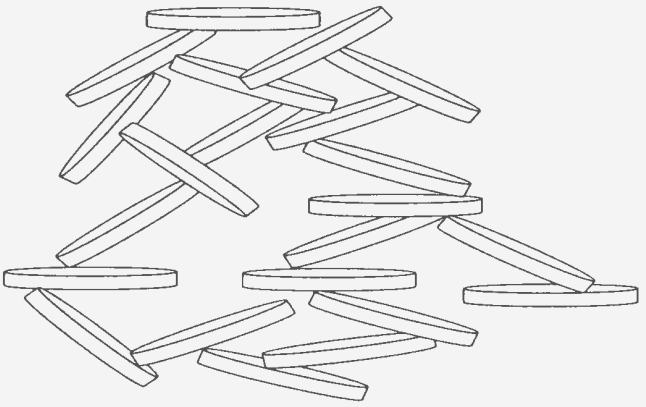

Figure 3.5: The "house of cards" structure of laponite showing edge-to-surface and surface-to-edge arrangements of the laponite disks.

Dry laponite consists of aggregates of particle stacks. Introduction of laponite powder into water leads to the dispersion of these aggregates into individual particle stacks. With time, the sodium ions become hydrated. This leads to a swelling of the structure, resulting in the stacks separating into individual disc-shaped particles. The hydration process is shown schematically in Figure 3.4. The primary laponite particle has a negative charge on the faces while the edges have small localized positive charge due to the absorption of hydroxyl groups from the particle. In deionized water, the sodium ions are held in equilibrium in diffuse regions on both sides of the dispersed particle by the opposing forces of electrostatic attraction and osmotic pressure from the bulk of the water. In dilute dispersions, laponite will remain a low-viscosity Newtonian fluid of non-interacting particles for a long time as electrostatic repulsion generated by surface-to-surface or edge to edge contacts coupled with osmotic pressure keeps particles apart from each other. The addition of polar compounds such as simple salts leads to a reduction in the osmotic pressure holding the sodium ions

away from the particle surface. This allows the weaker positive charge on the edge of the particles to interact with the negative surfaces of adjacent particles. With time this interaction may give rise to the so-called "house of cards" structure shown in Figure 3.5. This structure, once formed, can easily be broken down by the application of shear stress, but once the shear is removed, the structure will re-form with time. Thus in rheological terms, laponite forms a thixotropic gel in which the particles are held together by weak electrostatic forces [57].

Although laponite is a synthetic clay, it has properties similar to those of naturally occurring clays. In water, it forms a colourless, transparent thixotropic gel free of contaminants such as quartz that are found in natural clays. It can be prepared reproducibly and is easy to handle under experimental conditions. Because of these attributes, laponite has been used as a model for rheological studies of clay colloid behaviour [1, 37, 38, 40, 58]. Outside rheology, laponite is used as a thickening agent in the manufacture of household, agricultural, paper, polymer, personal care and building products, just to mention a few [57].

3.2 Fluorescence Microscopy

3.2.1 Fluorescence

The ability of a material to emit light when excited by another light source is called luminescence [59]. Fluorescence is a type of luminescence in which light is emitted

from molecules for a short period of time following the absorption of light. The delay time for fluorescence is typically of the order of 10^{-8} seconds. Similar processes with delay times of the order 10^{-6} and 10^{-4} s are called delayed fluorescence and phosphorescence respectively [60, 61].

The mechanism of the absorption-emission process was described by Sir George Stokes in 1852. He was also responsible for naming fluorescence after the mineral fluorite, which exhibits a bluish-white fluorescence under ultraviolet irradiation [61]. The absorption of light by matter occurs in discrete amounts called quanta. The energy in a quantum is given by

$$E = \hbar\nu = \hbar c/\lambda \tag{3.1}$$

where $\hbar$ is Planck's constant over 2π, c is the velocity of light in a vacuum, λ is the wavelength of the light and ν is its frequency. A valence electron is boosted up to a higher energy level when it absorbs a quantum of light. A quantum of light may then be emitted when the excited electron returns to the lower energy state. Stokes showed that the wavelength of the emitted fluorescence is longer than the wavelength of the absorbed light.

Figure 3.6 shows the various paths to deexcitation available to an electron excited by a photon A. The absorption process is shown by B while fluorescence, delayed fluorescence and phosphorescence are shown by C, D and E respectively. Permanent destruction of fluorescence can occur when, by light-induced conversion, a fluorescent material is chemically transformed into a non-fluorescent material. This process is

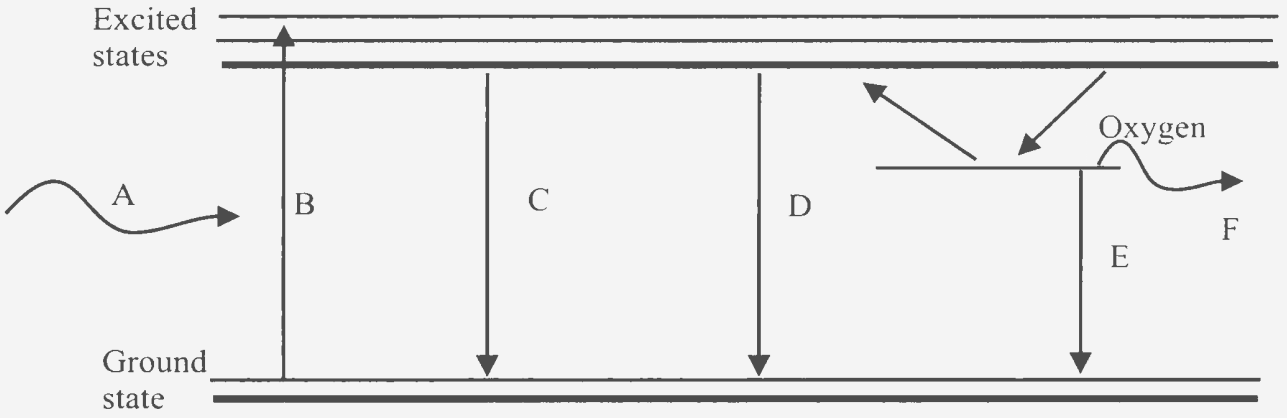

Figure 3.6: The deexcitation pathways available to an excited electron. The photon A interacts with the material ,and the absorption process is shown by B. The other processes are fluorescence(C). delayed fluorescence(D). phosphorescence(E), photo bleaching(F).

referred to as photobleaching and is depicted by F. The real cause of photobleaching remains evasive, but factors such as the nature of the fluorescent dye, chemical environment and the intensity of the quantum energy are known to be contributing factors [61].

3.2.2 The Working Principle of a Fluorescence Microscope

The German microscopist Köhler is credited as the inventer of fluorescence microscopy. In 1904, Köhler discovered that tissue is fluorescent when irradiated with ultraviolet light. With time, it was observed that stained sections of tissue could be examined in a fluorescence microscope if the dyes used in staining were fluorescent [61]. Over the years, this technique has been extensively exploited for research in the life sciences and has recently been employed in the physical science as well.

Modern fluorescence microscopes work on the principle of incident or epiillumi-

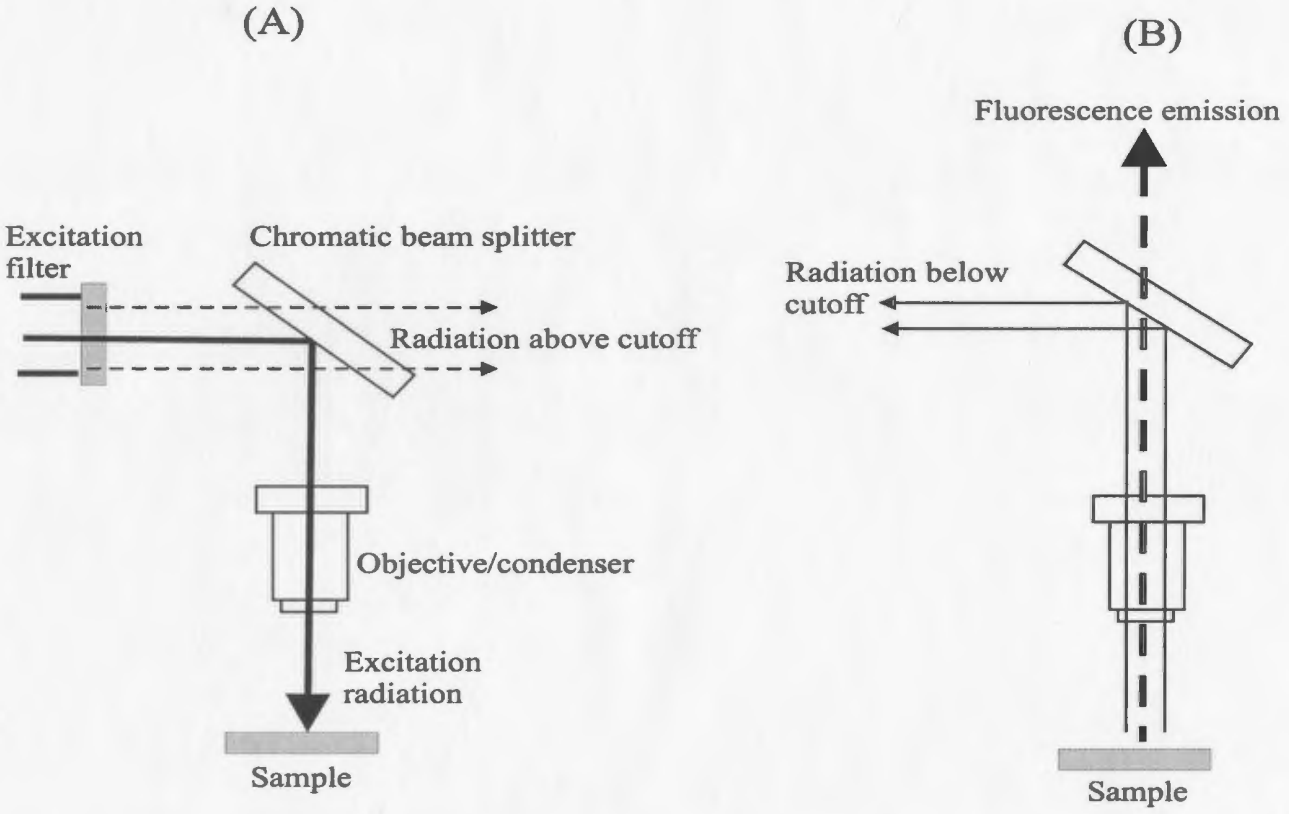

Figure 3.7: A schematic diagram of the working principle of a fluorescence microscope. A: Light below a cutoff wavelength is reflected through the objective and excites the sample (heavy black line). B: The emitted light that enters the objective above the cutoff passes to the detector as fluorescence emission (heavy dashed line).

nation [60]. A schematic diagram illustrating the working principle of an incident fluorescence microscope is shown in Figure 3.7. Epiillumination refers to the situation where the light that illuminates a specimen is directed through the objective lens of the microscope [61]. The specimen is excited by using the objective as a condenser. The chromatic beam splitter shown reflects light with a wavelength below a cutoff through the objective to excite the sample. The excitation radiation is shown by the heavy black line. The emitted fluorescence (heavy dashed line) that has a wavelength above the cutoff is not reflected but instead passes through the beam splitter to the detector. Emitted or reflected light below the cutoff wavelength is reflected away from the detector [60]. This ensures that only the fluorescence is detected, not any reflected excitation light.

3.3 Preparation of Samples

3.3.1 Fluorescent Microspheres

The fluorescent microspheres used for the experiments were purchased from Duke Scientific Corporation [62]. These spheres were made from polystyrene with fluorescent dye incorporated into the polymer matrix. Two microsphere diameters (0.49 and 1.0 μm) were used for the experiments. They have an excitation maximum of 542 nm (green) and an emission maximum of 612 nm (red) implying a Stokes shift of 70 nm [62]. The spheres have a density of 1.05 g/cm^3 and a refractive index of 1.59 at

589 nm.

In video microscopy only small amounts (of the order of a few microlitres) of the fluid are needed to make measurements, hence approximately 20 ml of each sample was prepared at a given time. The spheres are first sonicated for approximately 10 minutes to break down any clumping or coagulation resulting from long periods of refrigeration. To ensure that the spheres are well incorporated into the fluid structure, they are added to deionized water immediately after sonication at a volume fraction of typically $5.0 \times 10^{-3}\%$ for all samples. This volume fraction is dictated by the fact that for multiple particle tracking, the field of view should contain many particles at any time, yet few enough to keep collisions between spheres minimal. At this concentration the solutions appear slightly pink due to the presence of the microspheres. Typically about 50 to a few hundred spheres were in the field of view at any given time, depending on the concentration and the magnification used. The spheres are chemically neutral and are therefore not expected to react chemically with their environment.

3.3.2 Preparation of Carbopol ETD 2050 samples

Pre-determined amounts of carbopol powder were measured using an analytical balance and introduced carefully into the slowly agitated deionized water-sphere mixture. Care was taken not to add the powder too rapidly to prevent the formation of clumps. Once all the powder was introduced into the solution, stirring with a

glass rod was continued until all the resins were fully wet, which is evidenced by the transformation of all the white particles into transparent flakes in the solution. Any flakes that settled on the walls of the beaker were transferred into the solution with the glass rod.

As mixed, unneutralized carbopol solutions normally have a pH in the range 2.0 to 3.5, depending on the concentration, and have a relatively low viscosity, especially at low concentrations. To maximize gelation of the solution, 1.0N NaOH solution (Fischer Scientific, Catalogue No. SS266B-1 [63]) was added dropwise while the solution was being stirred until the pH was in the range of 5.8 to 6.3. Stirring is continued until all the transparent flakes disappear. The presence of remaining flakes is a signal of incomplete neutralization. Carbopol is known to reach its maximum thickness in this pH range [55]. At higher polymer concentrations. air bubbles will form as the gel traps air during stirring. To get rid of these, concentrated samples are centrifuged using a table-top centrifuge. Though the effect of this on the gel structure is not very clear, it is critical to remove the bubbles to allow accurate experimental measurements. The solution is then covered and allowed to stand overnight to ensure complete gelation before measurements are made. Four concentrations of carbopol. namely 0.01, 0.1, 0.5 and 1.0% carbopol by weight, were prepared for each of the two sphere sizes.

3.3.3 Preparation of Laponite RD samples

Laponite, which comes in the form of an easy-to-disperse white powder, was acquired free of charge from Southern Clay Products Inc., Texas [64]. Depending on the concentration desired, laponite powder is weighed and gently added to the deionized water mixture while it is being stirred with a magnetic stirrer. In this case 1M NaCl was added to the deionized water at a concentration of 1ml/l before the microspheres and clay were introduced. The Na^+ ions in the solution are supposed to prevent slow chemical reactions of the clay particles with atmospheric oxygen [34]. After the desired amount of laponite has been added, the solution is covered tightly and stirring is continued overnight to ensure complete dispersion and hydration of the laponite particles and to prevent immediate gelation. At the very early stages in the mixing the solution is cloudy, but with time it forms a very transparent gel (in this case slightly colored by the presence of the microspheres). The pH of the solution is then adjusted to the range 9.8 to 10 by the dropwise addition of 0.1M NaOH (Aldrich Chemicals, Catalogue No. 31,948-1 [65]) to ensure chemically stable samples [36, 39]. The solution is then sonicated for approximately 10 minutes to break down any gel structures. It is then again covered and allowed to stand undisturbed for a minimum period of 48 hours to allow the gel structure to reform slowly. In all, six different concentrations were prepared: 0.3, 0.5, 1.0, 1.5, 2.0 and 2.5% by weight. For investigation of the time dependence of gelation of laponite dispersions, measurements were made using a 1.5% concentration over a 24 hour period starting approximately 30 minutes after

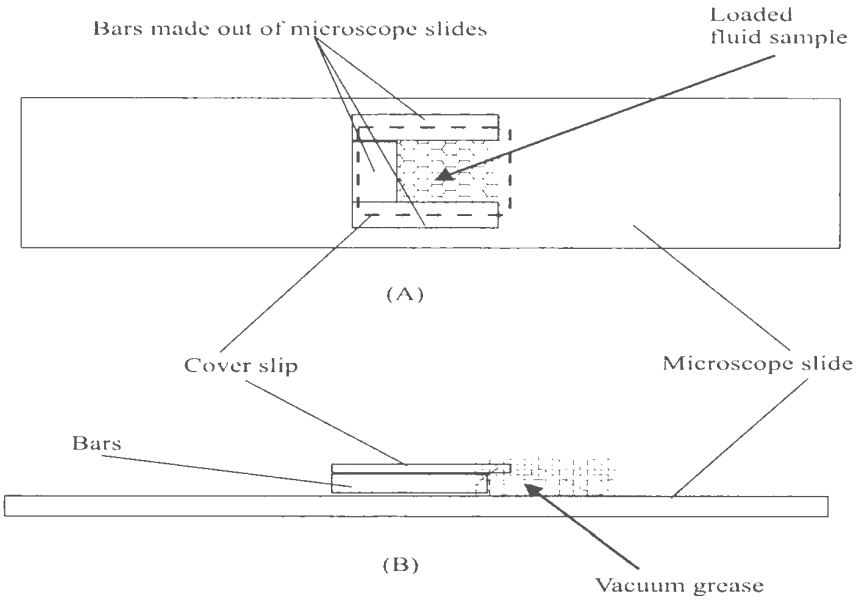

Figure 3.8: A schematic representation of the construction of a chamber for holding a sample on a microscope slide for imaging. (A): A three-sided wall is made out of small bars cut out of a microscope slide. This is glued firmly to the surface of another slide using optical glue. A coverslip is attached to the top of the walls to form a chamber with one side open, where the fluid is introduced. (B): A side view of the slide, showing the chamber sealed with vacuum grease.

sonication.

3.4 Experimental Procedure

The sample to be imaged is loaded into a chamber constructed on the surface of a microscope slide. The chamber was made to hold the fluid in place and to prevent any leakage which might induce flow in the sample. Three small glass bars cut out of a second microscope slide are glued together firmly on the first slide to form a three sided wall. A cover slip is then glued on top of these bars to form a chamber with one end open to allow introduction of the fluid. A mounting medium called

Micromount [66] is used for the construction of the chamber. This glue is a very strong adhesive, with the same refractive index as glass, hence it is ideal for imaging studies. The chamber is made to stand for at least 24 hours to allow the glue to set. A schematic representation of the chamber is shown in Figure 3.8. The fluid is loaded into the chamber by means of a glass dropper. The chamber is then firmly sealed with silicon-based high vacuum grease (Dow Corning [67]) which is known to be chemically inert. Once loaded, the fluid is allowed to equilibrate for 30 minutes to 1 hour before measurements are made.

An upright epiillumination fluorescence microscope (Olympus model BX50Wi) is used to image the samples. The spheres suspended in the fluid are excited by green light from a mercury lamp and give off red fluorescence. Images of the spheres are captured with a TM200 monochrome CCD camera (Pulnix Inc.) at a rate of 30 frames per second (fps) and recorded onto a VHS video cassette. Recording times ranged from 10 to 20 minutes depending on the concentration of the sample. Before images are recorded, it is ensured that there is no drift in the sample. Drift would make the spheres tend to move in one direction and thus obscure the diffusive component of their motion. Samples for which drift was observed were discarded. To minimize wall effects, the objective was focused roughly halfway into the sample.

The recorded images are digitized off line using a IMAQ PCI 1407 frame grabber (National Instruments [68]). Images are digitized at different frame rates, chosen so that the motion of the tracer spheres between frames can be detected by the particle

tracking software. The frame grabber could only digitize 1800 frames at a time, so for longer runs the frame rate had to be reduced to compensate for this. Images from the video were digitized at typical frame rates of 15, 10, 6 and 2 fps.

3.5 Image Processing

Image processing and data analysis were done using particle tracking software written in IDL [69] by Crocker et al. [45, 70] The time evolution of the distribution of particles can be described by

$$\rho(\mathbf{r}, t) = \sum_{i=1}^{N} \delta(\mathbf{r} - \mathbf{r}_i(t)) \tag{3.2}$$

where $\mathbf{r}_i$ is the location of the ith particle in a field of N particles at time t. The image analysis package enables the extraction of the trajectories $\mathbf{r}_i(t)$ of individual microspheres from a set of images.

A typical raw digitized image is shown in Figure 3.9. The bright spots are the fluorescent microspheres. The brightness varies depending on whether the sphere is in focus, below or above the plane of focus or even photobleached. Digitized images may contain imperfections such as geometric distortions, non-uniform contrast and noise. The imperfections introduce error in the determination of $\rho(\mathbf{r}, t)$. The first step in the image processing is the restoration of the images with a view to reducing these imperfections as much as possible. The software filters the image and subtracts the background off. The bright spots are transformed into sharply peaked circular blobs,

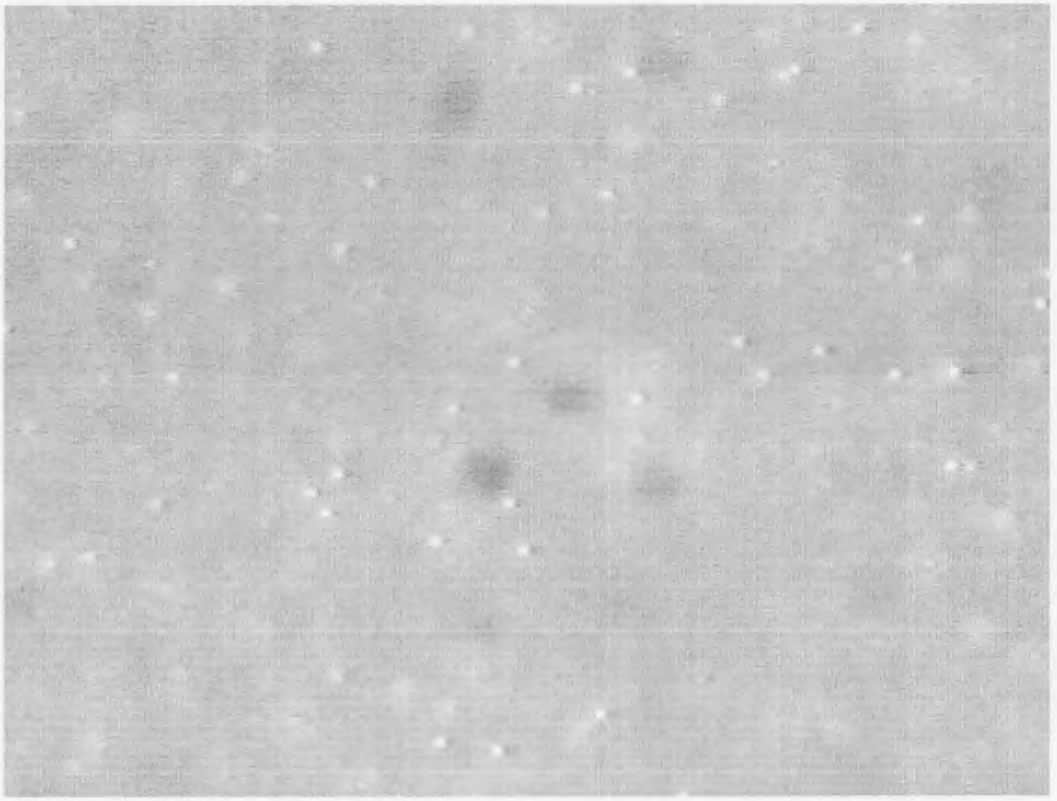

Figure 3.9: A representative raw image of the fluorescent spheres.

Figure 3.10: The restored image corresponding to Fig. 3.9. The background has been subtracted off.

making it easier for the software to discriminate between noise and real particles. The restored version of Figure 3.9 is shown in Figure 3.10.

Local brightness maxima within the restored image are considered as candidate particles. The software adopts a particular pixel as a candidate particle position if no other pixel within a specified distance w is brighter. w is an integer which is larger than the apparent radius (in pixels) of a single sphere or blob but smaller than the average inter-sphere separation. To discriminate true particles from noise, only the brightest pixels are considered as particle positions. A cutoff is set and all pixels with brightness below this value are rejected. Optional parameters, such as the

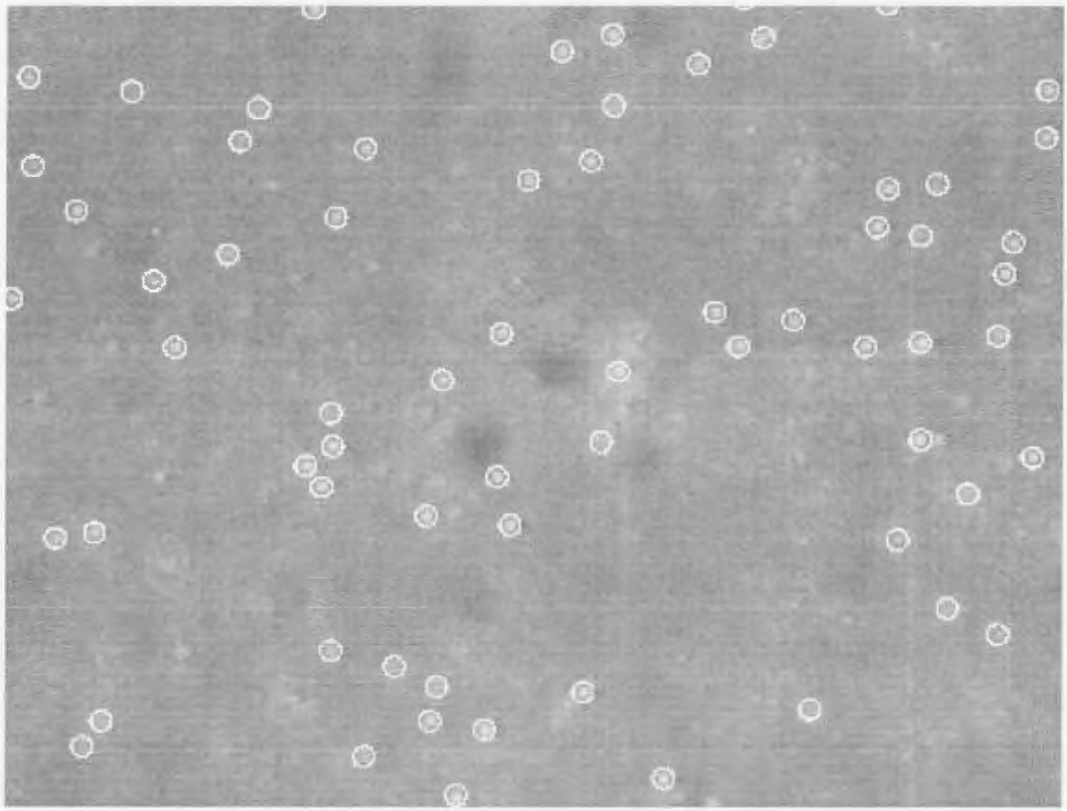

Figure 3.11: The same image as Fig. 3.9, with circles drawn around blobs selected by the particle tracking software as particle positions.

eccentricity and particle size, may be used to further discriminate true particles from doubtful ones in cases where the images are very noisy and particle misidentification is a worry. To test the accuracy of the particle locations, it is possible to make the software draw circles around the blobs in the original image that have been selected as particle locations. Figure 3.11 shows this for the image of Figure 3.9. Once the particle positions have been satisfactorily determined, other sub-routines in the software refine the particle positions to reduce the uncertainty of the position measurements.

The final stage in the particle tracking procedure is to match up locations in each image with corresponding locations in later images to produce the trajectories in

$\rho(\mathbf{r}, t)$. This is achieved by identifying which particle in a given image most likely corresponds to one in the preceding image. For indistinguishable particles, this is only possible by proximity.

Given that dr is the distance that a particle moves between frames, the most likely assignment of particle labels from one frame to the other is the one which minimises $\sum_{i=1}^{N} dr_i^2$, where N is the number of particles. The process of label assignment may be considered as drawing bonds between pairs of particles in consecutive frames. Only bonds shorter than a length L are allowed as possible candidates for the assignment of particle labels between two frames. L is chosen to be slightly higher than the maximum absolute displacement of the particles between frames. This value can be estimated from a plot of the distribution of displacements. Linking of particles is possible only if the typical particle displacement dr in one timestep is sufficiently small compared to the typical interparticle spacing a. The optimal value of L is in the range $dr < L < a/2$.

3.6 Calibration and Error Analysis

Samples containing the 0.49 and 1.0 μm spheres were imaged using $\times 60$ and $\times 20$ objectives, respectively. A C-mount attached to the microscope with a magnification of $\times 2.5$ leads to final magnifications of $\times 150$ and $\times 50$ respectively. A calibration slide etched with a 1 mm mark further divided into 100 divisions was used to get the conversion factor from pixels to microns for the various magnifications. The slide was

imaged at $\times 150$ and $\times 50$ and the corresponding conversion factors were found to be 0.217 μm and 0.625 μm per pixel respectively. Uncertainties in the particle positions were calculated by imaging immobile particles at magnifications of $\times 150$ and $\times 50$. The mean squared displacement (MSD) of a Brownian particle motion can be written as

$$\left\langle x\left(\tau\right)^2\right\rangle = 2D\tau + \sigma^2 \tag{3.3}$$

where σ is the mean random error in determining the particle position. For immobile particles, $D = 0$ and hence $\left\langle x\left(\tau\right)^2\right\rangle = \sigma^2$ [71]. The uncertainties were found to be 0.02 μm and 0.08 μm respectively.

The accuracy of the tracking software as well as the experimental setup was verified by analyzing the motion of the two sizes of spheres in water using the same experimental conditions as used for the main experiments. Since water is a Newtonian fluid, it is expected that the mean squared displacements for the two spheres will both have logarithmic slopes of 1.0 and that the distribution of their displacements at a specific lag time will be Gaussian. The MSD as a function of lag time for the two sphere sizes in water is shown in Figure 3.12. The logarithmic slopes of the MSD for the 0.49 and 1.0 μm spheres were 0.95 ± 0.14 and 0.96 ± 0.07 respectively. The corresponding diffusion coefficients for the spheres as calculated from the intercept of the MSD were 0.77 ± 0.02 and 0.41 ± 0.08 μm^2/s respectively. The solid line in Figure 3.12 shows the MSD for the 0.49 μm sphere scaled by the particle size. It falls directly on the MSD for the 1.0 μm sphere. This is expected, since the scaled MSD

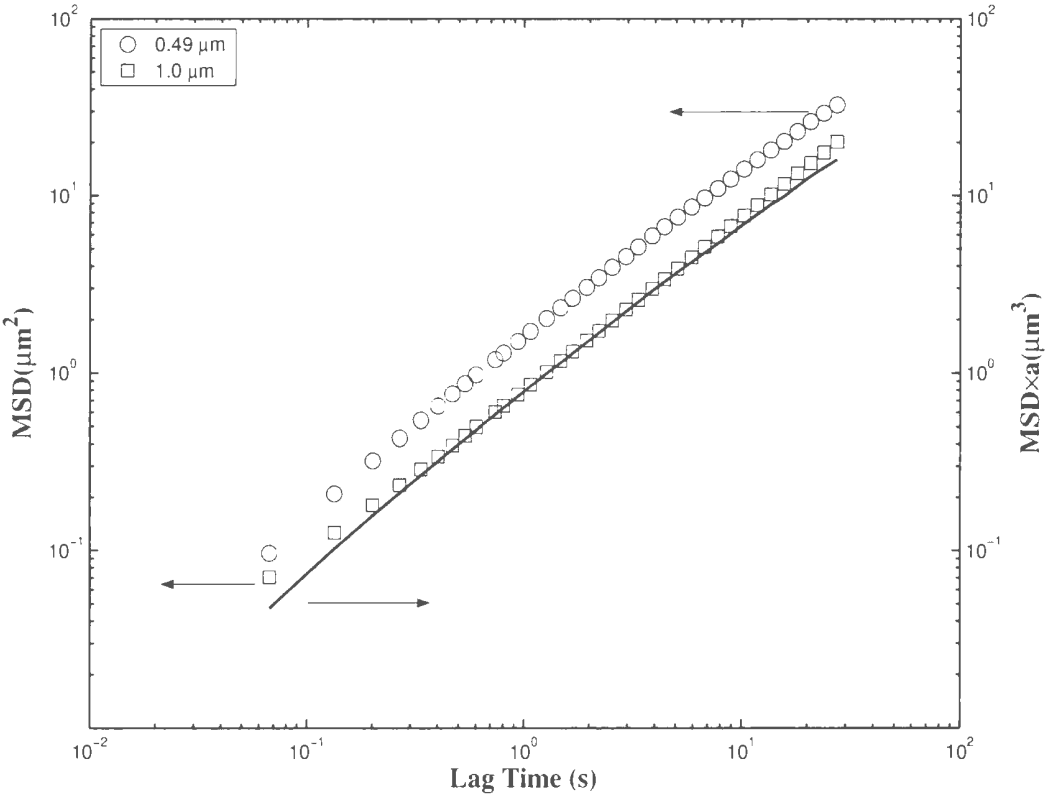

Figure 3.12: MSD for the 0.49 and 1.0μm spheres in water. The solid line is the MSD data for the 0.49μm normalized by the sphere size. It compares very well with the 1.0μm data.

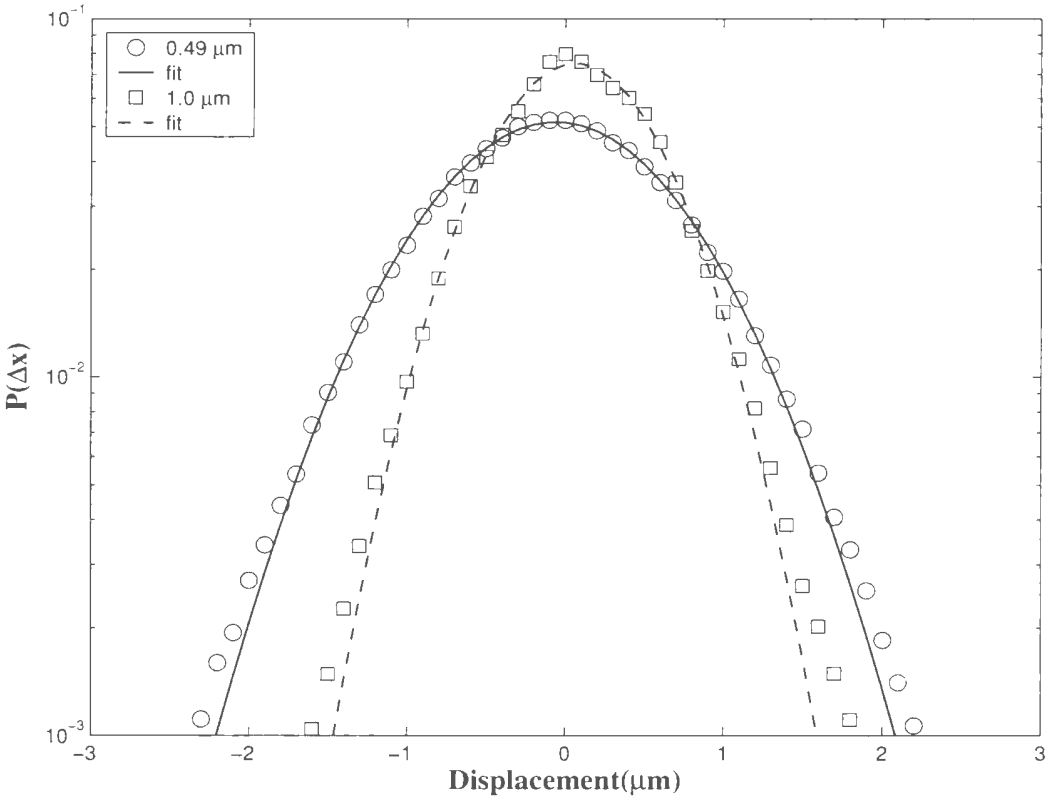

Figure 3.13: The distribution of the displacements of the 0.49 and 1.0 μm spheres in water at a lag time of 0.33 s. The curves are the Gaussian fits to the data.

should be independent of particle size for purely diffusive motion. The distributions of particle displacements are shown for a lag time of 0.33 s in Figure 3.13. They are well described by Gaussian distributions, which give the diffusion coefficient for the 0.49 μm sphere as 0.82$\pm$0.06 $\mu m^2/s$ and that of the 1.0 μm sphere as 0.41$\pm$0.06 $\mu m^2/s$. These values are in agreement with those calculated from the fits to the MSD data. It has been reported in literature that 1.02 μm spheres in water have a diffusion coefficient of 0.402$\pm$0.06 $\mu m^2/s$ [43] and 0.98 μm spheres has a value of 0.43 μm^2 [72]. Our results obtained for the 1.0 μm sphere are in good agreement with these results. Although no values were found in literature for 0.49 μm spheres, the diffusion coefficient is inversely proportional to the particle size [45], so we expect a diffusion coefficient of approximately 0.84 $\mu m^2/s$. Our results for the 0.49 μm sphere are consistent with this.

Chapter 4

Results and Discussion: Carbopol

4.1 Introduction

In this chapter, the experimental results for carbopol are presented and discussed. This material was studied both as a function of probe particle size (0.49 and 1.0 μm) and polymer concentration (0.01, 0.1, 0.5 and 1.0% carbopol by weight). We first present the trajectories of the two sizes of spheres as they move in the different concentration samples and interpret them in terms of the local properties of the fluid. The ensemble-averaged mean square displacement (MSD) is then presented and discussed. To get an idea of how the motion of the spheres depends on lag time, we calculate the instantaneous logarithmic slope of the MSD for our data. Spatial heterogeneity in the fluid can be investigated through the distribution of the particle displacements as a function of lag time. We present results for two lag times for each particle size. We also studied the dynamical heterogeneities in the fluid as a function of time by calculating the non-Gaussian parameter (NGP) which is related

to the fourth moment of the distribution. In fact the lag times for the distributions were partly chosen to correspond to time-scales at which the spheres begin to respond to structures in the fluid, as indicated by high NGP values. We also analyzed the correlations between successive displacements at a given lag time, and used the results to estimate the strength and length scales of the pores in the fluid.

4.2 Particle Trajectories

A wealth of information relating to the local environments of fluids can be extracted from the nature of the trajectories of small tracer particles probing them. When a particle moves in a purely Newtonian fluid, the trajectories are purely random with no preferred direction of movement. The trajectories of particles in complex fluids may not always be random. In the course of their motion, the particles can bump into, or be confined to, certain regions of the fluid by the structure of the fluid. Under such circumstances, the particles tend to stay in the confining regions longer than they would if they were moving freely. The trajectories under such circumstances will be non-uniform with some areas of the sample visited more often than other areas. The particles can also become trapped and prevented from moving away from the confining region. Trapped particles are characterized by highly compact and localized trajectories.

Two-dimensional projections of the trajectories of the tracer spheres were measured by fluorescence microscopy, as discussed in Sec. 3.3.1. Typical results are shown

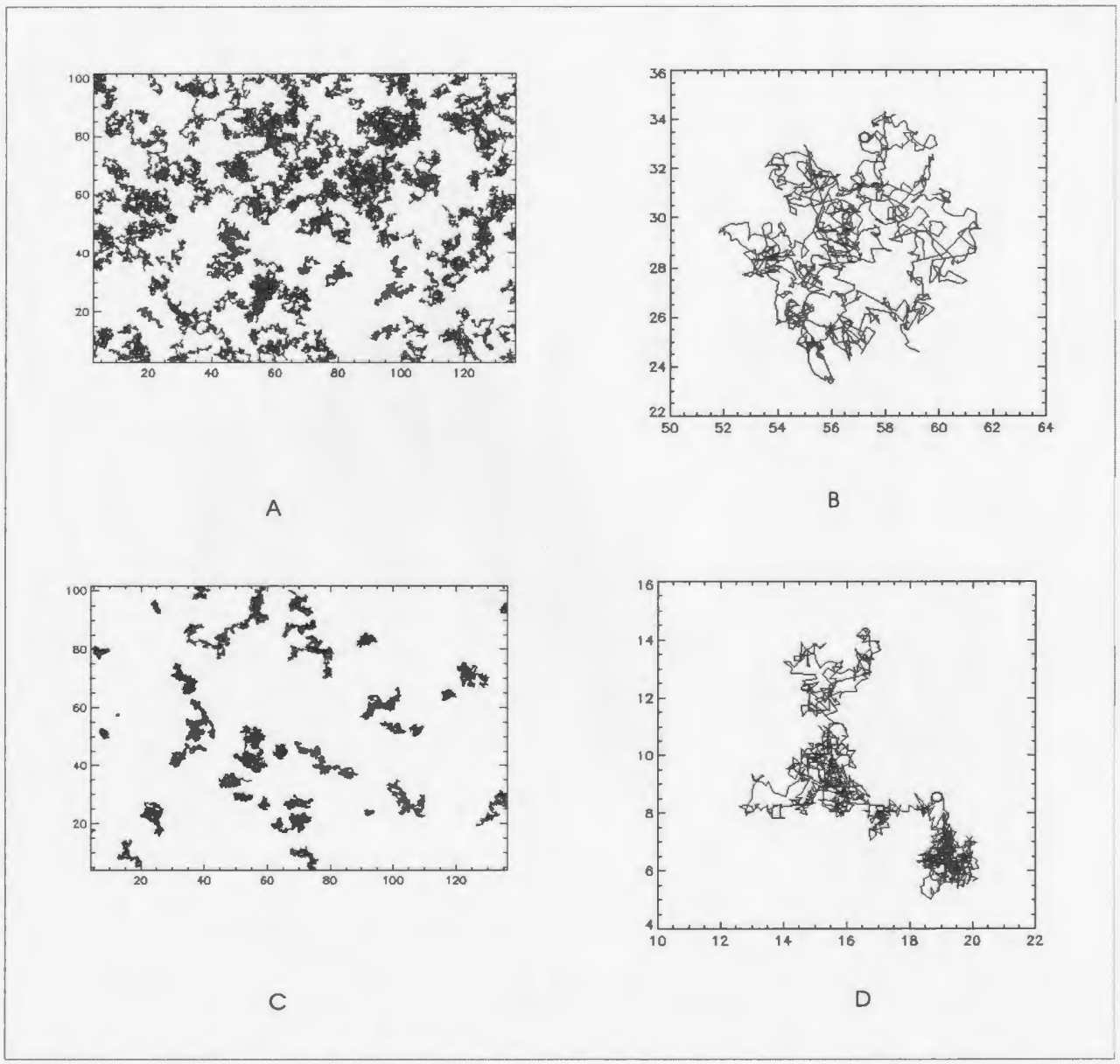

Figure 4.1: Trajectories for 0.49 μm spheres in carbopol with concentrations of 0.01% (A and B) and 0.1% (C and D). A and C show the trajectories for all the spheres within the field of view of the fluorescence microscope, while B and D are typical trajectories for a single sphere. The durations for B and D are 120 s and 300 s respectively. Both the x and y axes are in microns.

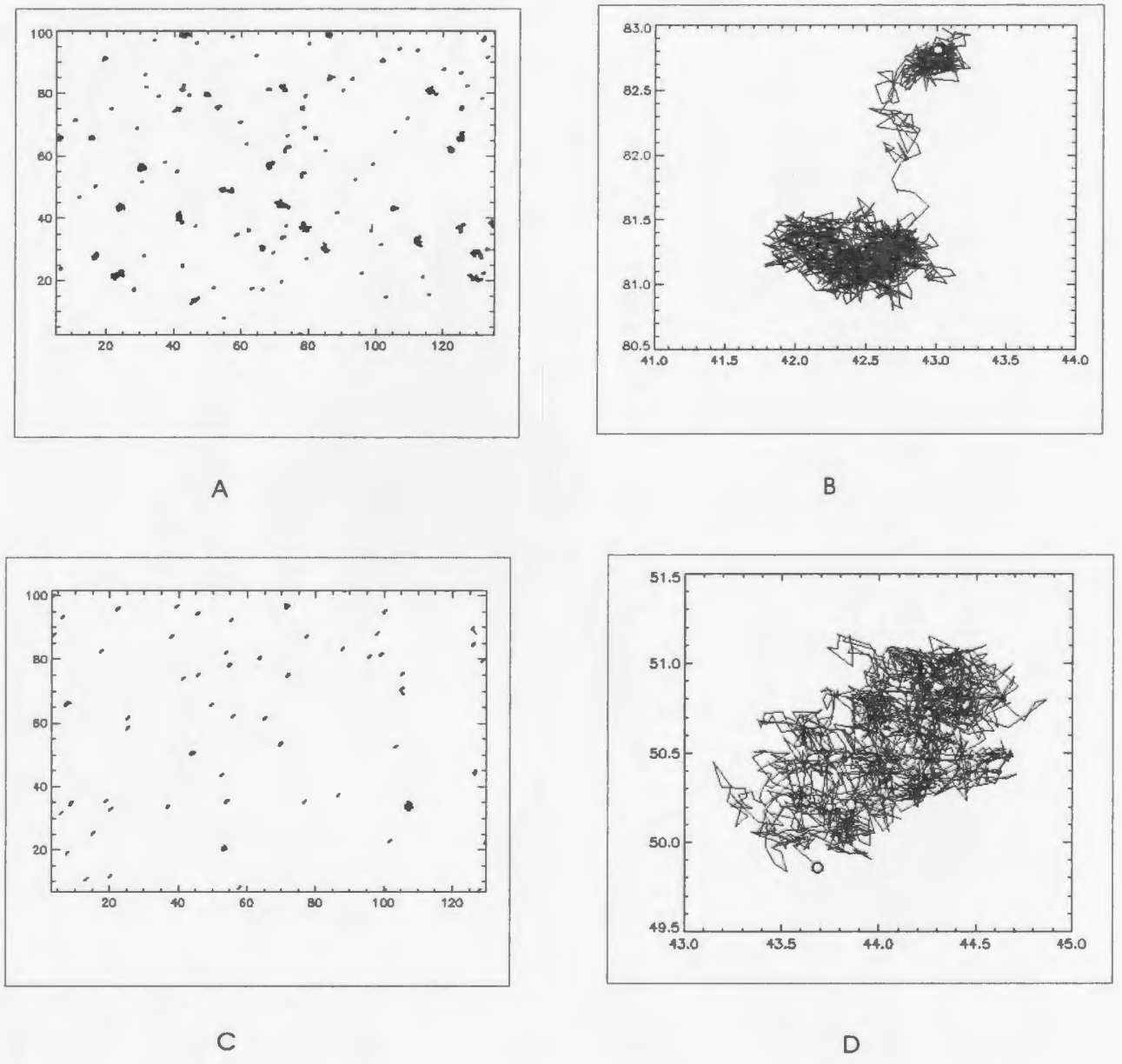

Figure 4.2: Trajectories for 0.49 μm spheres in carbopol with concentrations of 0.5% (A and B) and 1.0% (C and D). A and C show the trajectories for all the spheres within the field of view of the fluorescence microscope, while B and D are typical trajectories for a single sphere. The duration for both B and D is 300 s. Both the x and y axes are in microns.

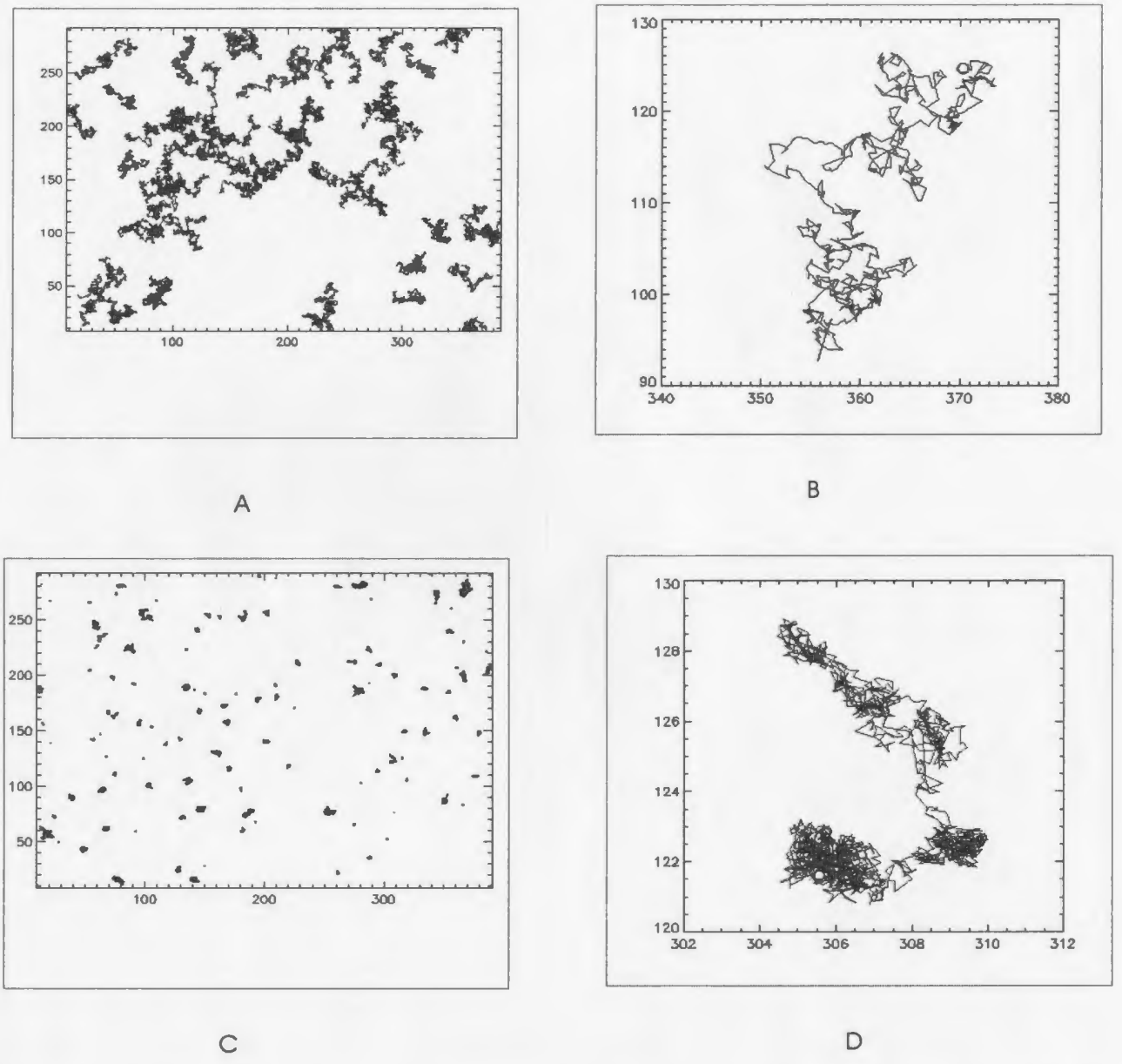

Figure 4.3: Trajectories for 1.0 μm spheres in carbopol with concentrations of 0.01% (A and B) and 0.1% (C and D). A and C show the trajectories for all the spheres within the field of view of the fluorescence microscope, while B and D are typical trajectories for a single sphere. The duration for B and D is 900 s. Both the x and y axes are in microns.

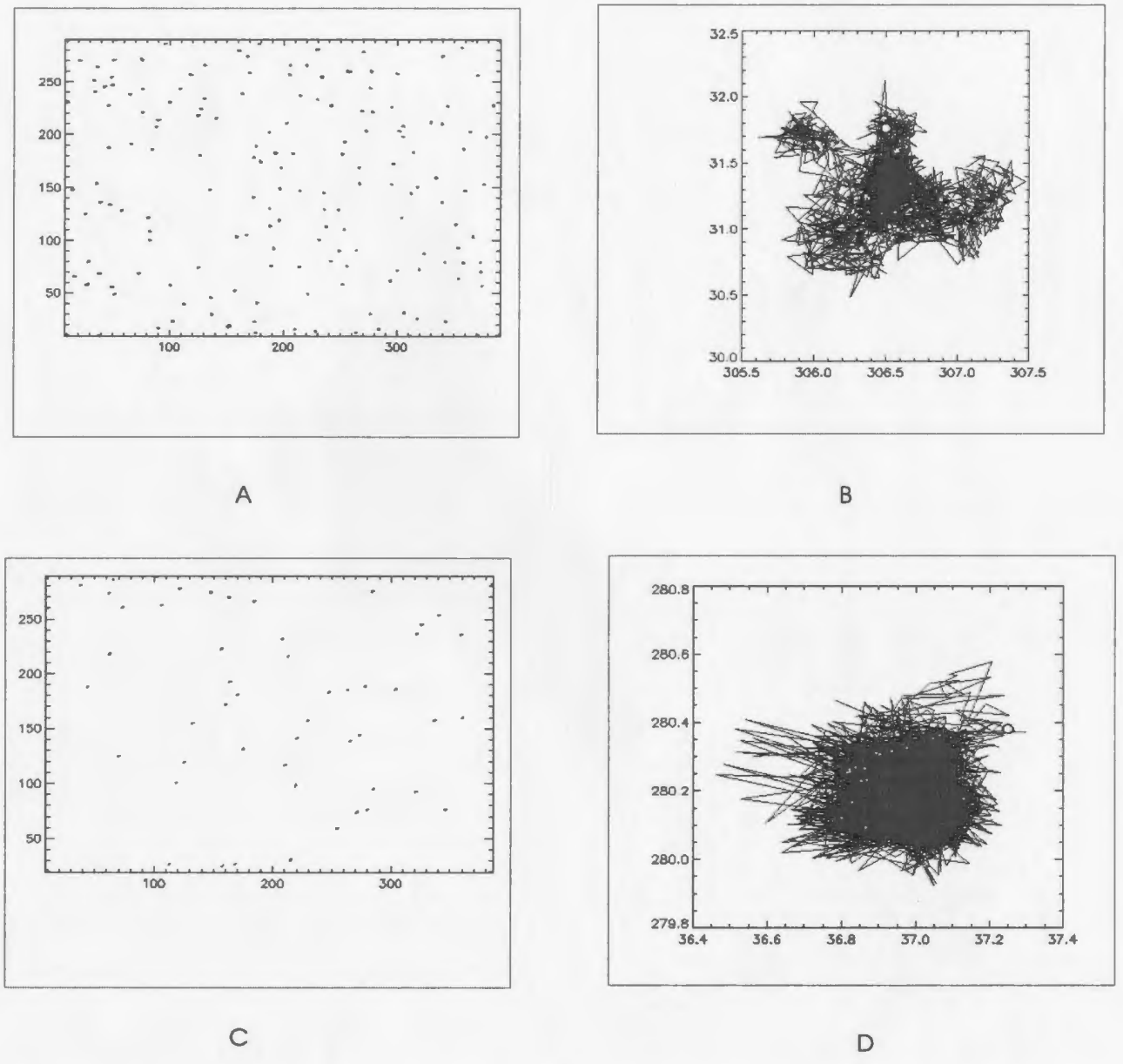

Figure 4.4: Trajectories for 1.0 μm spheres in carbopol with concentrations of 0.5% (A and B) and 1.0% (C and D). A and C show the trajectories for all the spheres within the field of view of the fluorescence microscope, while B and D are typical trajectories for a single sphere. The duration for B and D is 900 s. Both the x and y axes are in microns.

in Figs. 4.1-4.4. The figures on the left show all the trajectories for all particles tracked in the field of view while those on the right show representative individual particle trajectories. The spikes in the trajectories seen particularly in Fig. 4.4 may be due to error in particle measurement or to jiggling of the optical system. The trajectories for the 0.49 μm spheres are shown in Figures 4.1 and 4.2. The duration of the single trajectory shown for the 0.01% concentration in Fig. 4.1B is 120 s. All the other single trajectories shown in Figs. 4.1 and 4.2 have a duration of 300 s. Trajectories for the 1.0 μm spheres are shown in Figures 4.3 and 4.4. The trajectories for the 1.0 μm spheres all have a duration of 900 s.

Comparing the trajectories, we observe that they become more compact and localized with increasing concentration. This implies that the motion of the particles becomes more constrained with increasing concentration. As discussed in Chapter 3, carbopol consists of swollen microgels with water-containing pores between these microgels. We therefore suspect that the restricted motion at higher concentrations is due to the particles being confined to pores in between these microgels. As the concentration of the polymer is increased, the concentration of the microgels also increases and the pores become smaller, so the particles are constrained much more strongly at higher concentrations. Except for the 0.01% concentration, shown in Figs. 4.1(A) and 4.3(A), we observe that the trajectories are non-uniform in the sense that some are more compact than others. This suggests that different particles experience different microenvironments and hence we conclude the fluid is inhomogeneous on

these length scales and at these concentrations.

The trajectories for the 0.01% concentrations (Figs. 4.1B and 4.3B) are uniform and completely random. This suggests that the particles at this concentration move freely and the motion is diffusive. At intermediate concentrations, close examination of the individual trajectories suggests that they are non-uniform. There are areas where the trajectories are more condensed. This implies that the motion of the particles are constrained by structures in the fluid. There are also areas where the particle moves more freely, which is evidenced by a less condensed trajectory. This implies that there is a possibility that particles can move from pore to pore. This behaviour is very clear for the single trajectories shown for the 0.1 and 0.5 % concentrations (Figs. 4.1D, 4.2B, 4.3D, 4.4B). The trajectories for the 1.0% concentrations (Figs. 4.2D and 4.4D) are more compact suggesting that the particles are confined to a certain region of the fluid, presumably within a pore. The trajectories of the 1.0 μm particles are much more localized than those for the 0.49 μm spheres. This means that the 1.0 μm spheres move less than the 0.49 μm spheres. The 0.49 μm sphere trajectory spans roughly 1.5 μm in both the x and y directions. Our data suggest that at this concentration, the pores are small enough to prevent the particle from escaping, yet large enough compared to the size of the particle to permit some degree of motion within the pore. In Figure 4.4(D), the trajectory spans a distance of roughly 0.4 μm in the y direction and 0.7 μm in the x direction, which is less than the particle size. This suggests that the particle size is comparable to the pore

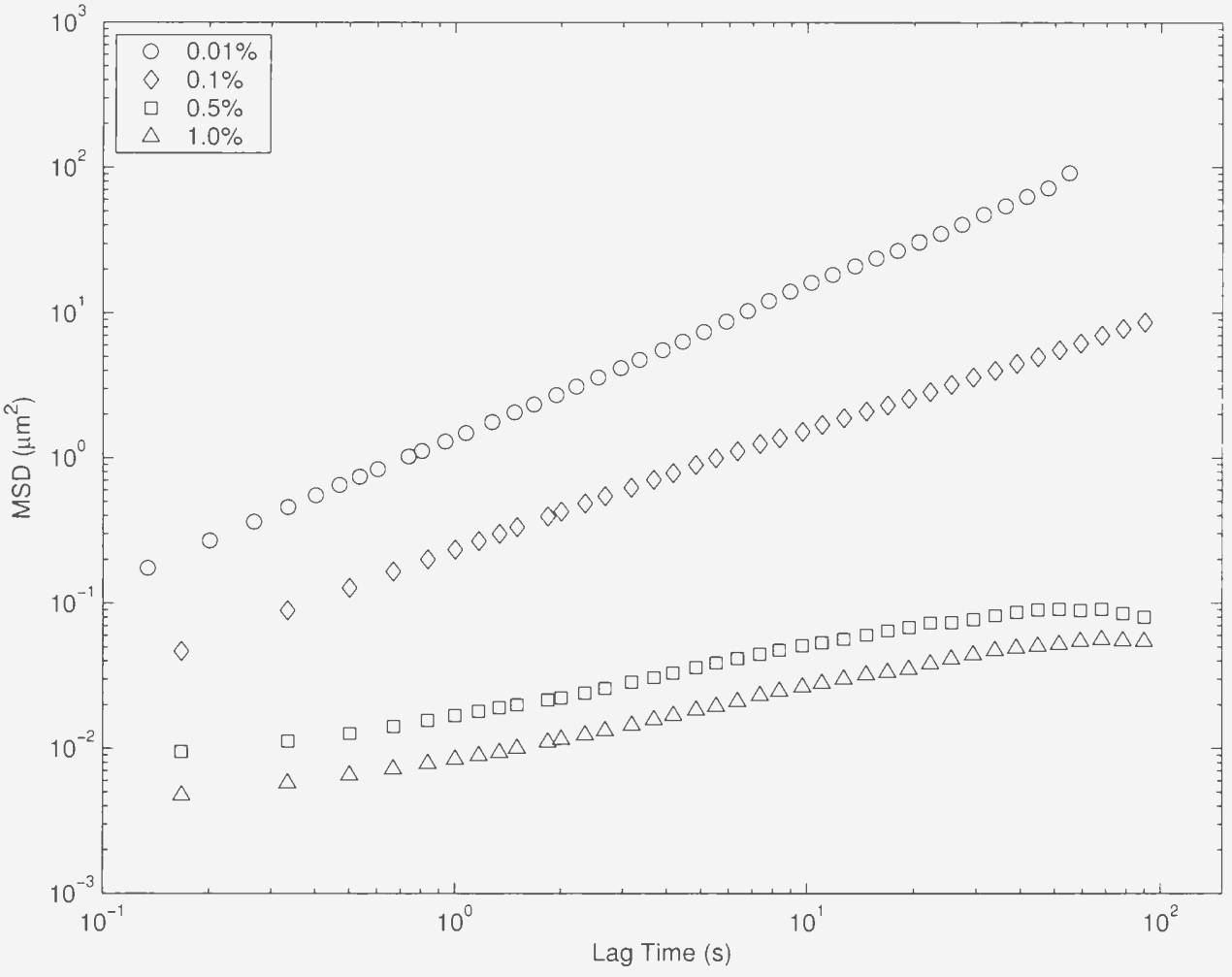

Figure 4.5: A log-log plot of the mean square displacement for the 0.49 μm spheres. The different symbols indicate different concentrations of carbopol.

size and that the sphere is completely trapped, at best jiggling around slightly within the pore but without any appreciable large scale motion.

4.3 Mean Square Displacement

Log-log plots of the one-dimensional mean square displacement $\langle x^2(\tau)\rangle$ for the 0.49 μm and 1.0 μm spheres are shown in Figures 4.5 and 4.6 respectively. x^2

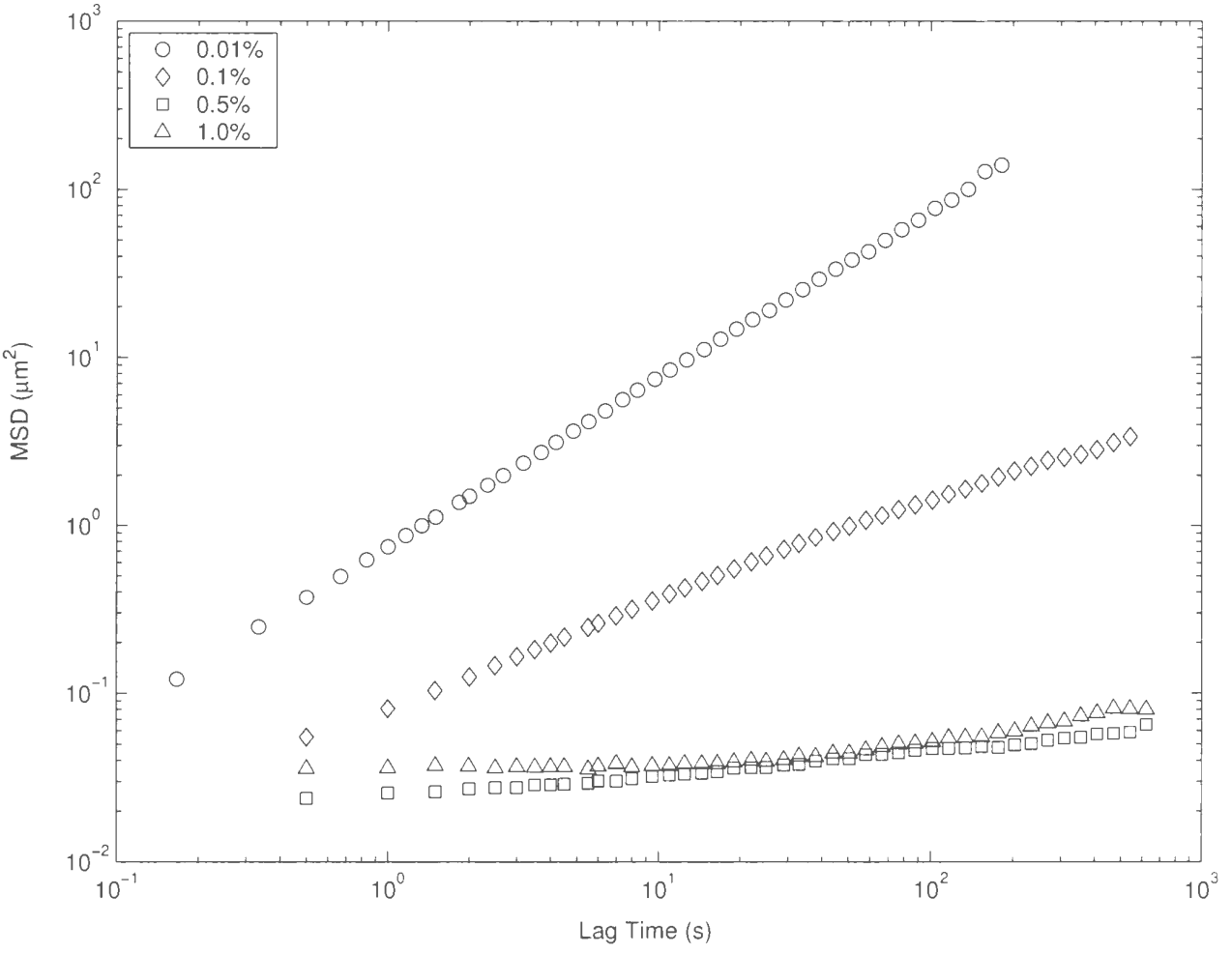

Figure 4.6: A log-log plot of the mean square displacement for the 1.0 μm spheres. The different symbols indicate different concentrations of carbopol.

was averaged over all pairs of points a time τ apart as well as over all the tracked particles [8, 49]. As discussed in Chapter 2, the motion of the spheres can in general be described by $\langle x^2(\tau)\rangle \approx \tau^\alpha$. For simple diffusion, $\alpha = 1$, but in general α can be a function of lag time τ. Here the values of α were calculated from the slopes of straight lines fit to the log-log plots of the MSD for the 0.01% samples. The τ dependence of α is discussed below.

We consider first the MSD for the 0.49 μm spheres as function of concentration shown in Fig. 4.5. The 0.01% data follow a good straight line on the log-log plot and the diffusive exponent was found to be 1.03 ± 0.01. This implies that the motion of the spheres at this concentration is diffusive. For the 0.1% concentration, although the plot is slightly concave downwards, the MSD shows no true plateau. This means that while the motion of the spheres is affected by the local microenvironments, there is no evidence of permanent entrapment by the pores at this concentration. This result is consistent with observations we made based on the particle trajectories in the previous section.

The MSDs for 0.5 and 1.0% concentrations can be best described by three time regimes. For very short times ($\tau < 0.5$ s) the spheres move only short distances, leading to a low slope at the earlier times. At intermediate times ($0.5 < \tau < 20$ s), the slope increases implying the spheres move more freely although still subdiffusing on these time scales. At long times ($\tau > 20$ s) the MSD approaches a plateau, indicating that the spheres are being constrained from moving any further. This

suggests that at these concentrations the spheres are confined to pores within the fluid, again consistent with our earlier observations.

The log-log plot of the MSD for the 1.0 μm sphere at a concentration of 0.01% is a straight line, i.e., a power law relationship holds over the time range studied. The diffusive exponent was found to be 1.00 ± 0.01, again indicating diffusive motion. For the 0.5 and 1.0% concentrations, the MSDs are small and almost independent of time. This indicates that at these concentrations the pores in the fluid have trapped the spheres, preventing them from escaping or moving. At long time we observe a slight increase in slope of the MSD indicating that the spheres are able to move slightly at long lag times.

As discussed in Chapter 1, the mean square displacement is a very important quantity that can be used to interpret the average mechanics of the microenvironments in complex systems. Plateaus in the MSD at long times indicate that the particles are constrained by the fluid in which they are suspended. The nature and cause of the constraint is, however, not always obvious. To understand the constraint, further analysis is necessary, depending on the nature of the fluid under study. If the fluid is homogeneous, then the plateau can be interpreted in terms of the elastic modulus of the fluid. In the case of heterogeneous environments, however, the plateau may be either a measure of the local elasticity or a measure of the size of the local constraining volume or pore, depending on how $\langle x^2(\infty) \rangle$ scales with particle radius a. If the plateau measures the local elasticity, then $\langle x^2(\infty) \rangle$ scales with $1/a$. If it

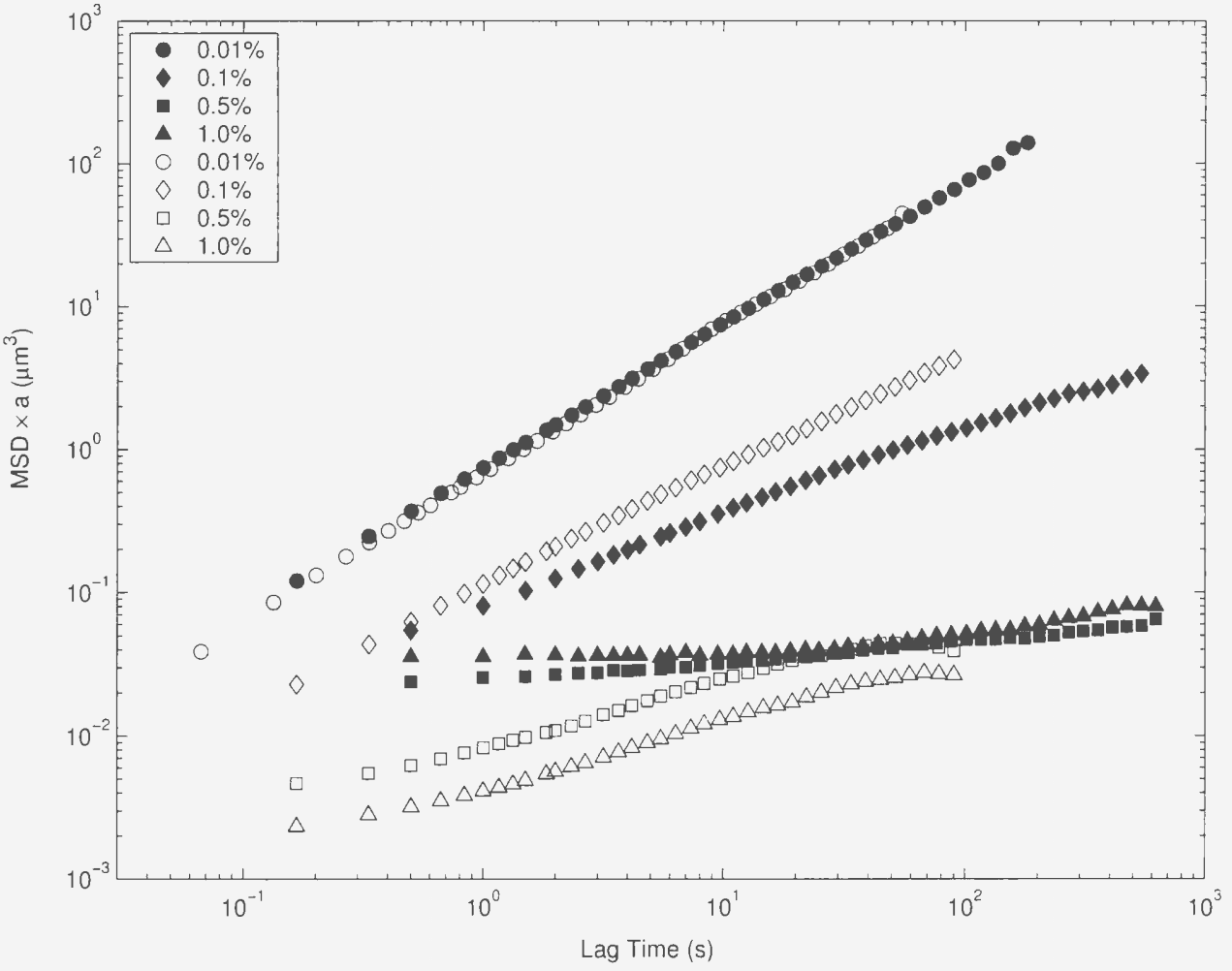

Figure 4.7: Comparison of the MSD for the two sphere sizes scaled with the sphere radius a. The closed symbols are for the 1.0 μm spheres while the open symbols are for the 0.49 μm spheres.

is measure of the pore size d, then $d \approx 2a + h$, where h is the size of the fluid filled gap between the particle surface and the pore wall. In this case h is approximated by $\langle x^2(\infty)\rangle^{1/2}$ [8].

We investigated the scaling of the MSD with particle radius a . and the result is shown in Fig. 4.7. In normal diffusion, the diffusion coefficient, $D \propto 1/a$, so if the scaled data overlap at short times then D behaves as expected for normal diffusion.

If the data do not scale, then other factors such as the structure of the fluid affect the motion of the tracer particles. From our results, the scaled MSDs overlap at all lag times for the 0.01% concentration. This means that at this concentration, the motion of the spheres are diffusive at all lag times studied. At 0.1% concentration, the scaled MSD overlap at short lag times but deviate from each other at longer lag times. This indicates that the motion of the spheres is diffusive at short lag times, but at long lag times, as the spheres feel the effect of the structures in the fluid, their motion become subdiffusive. For the 0.1% concentration, the scaled MSD for the 0.49 μm spheres is higher than that of the 1.0 μm spheres at longer lag times indicating a higher mobility for the 0.49 μm spheres. The difference between the two increases with lag time. This shows that at longer lag times, the motion of the 1.0 μm spheres is constrained to a greater extent than that of the 0.49 μm spheres. For the 0.5% concentration, the scaled MSD for the 1.0 μm spheres remains constant at all times while that of the 0.49μm spheres increases gradually until it collapses onto the 1.0 μm data at long times. After this time both spheres maintain the same MSD for all subsequent times. For the 1.0% concentration, the behaviour for short lag times is similar to that at 0.5% concentration, except that the data do not overlap at long lag times. Thus while the scaling behaviour of the MSDs at 0.5% seems to suggest that the spheres are measuring the local elasticity, that at 1.0% suggests a measurement of the pore size. While further work will be needed to clearly establish the nature of constraint at these long times, the trapping effects seen in the trajectories at these

Sphere Diameter(μm)	Pore Size (0.5%) μm	Pore Size (1.0%) μm
0.49	0.79 ± 0.01	0.73 ± 0.01
1.0	1.20 ± 0.01	1.22 ± 0.01

Table 4.1: Estimates of the pore size calculated from the plateaus in the MSD for the 0.5% and 1.0% carbopol samples.

concentrations suggest that the plateau is more of a measurement of the pore size than local elasticity. Using the analysis above, the pore sizes were estimated. The results are shown in Table 4.1. To the nearest micron we find that pores in the fluid are on the order of 1 μm in size.

The diffusion coefficients are calculated from the intercepts obtained from the fits to the log-log MSD plots for the 0.01% data for both spheres. We had 0.70±0.01 μm^2/s for the 0.49 μm spheres and 0.37±0.01 μm^2/s for the 1.0 μm spheres. These values are lower than those calculated for the spheres in water. This is because the presence of the polymer leads to an increase in viscosity of the fluid.

The diffusive exponent α describes the logarithmic slope of $\langle x^2(\tau)\rangle$ at the time τ and may be defined as

$$\alpha(\tau) = \frac{d \ln \langle x^2(\tau)\rangle}{d \ln t}. \tag{4.1}$$

To investigate the dependence of the diffusive exponent on τ, we calculated this quantity at each lag time using simple differences, smoothing over two neighboring values to reduce scatter. The results are shown in Figures 4.8 and 4.9. This quantity is identical to the slope of the log-log plots of the MSD data, but in this case, α has been evaluated at each τ.

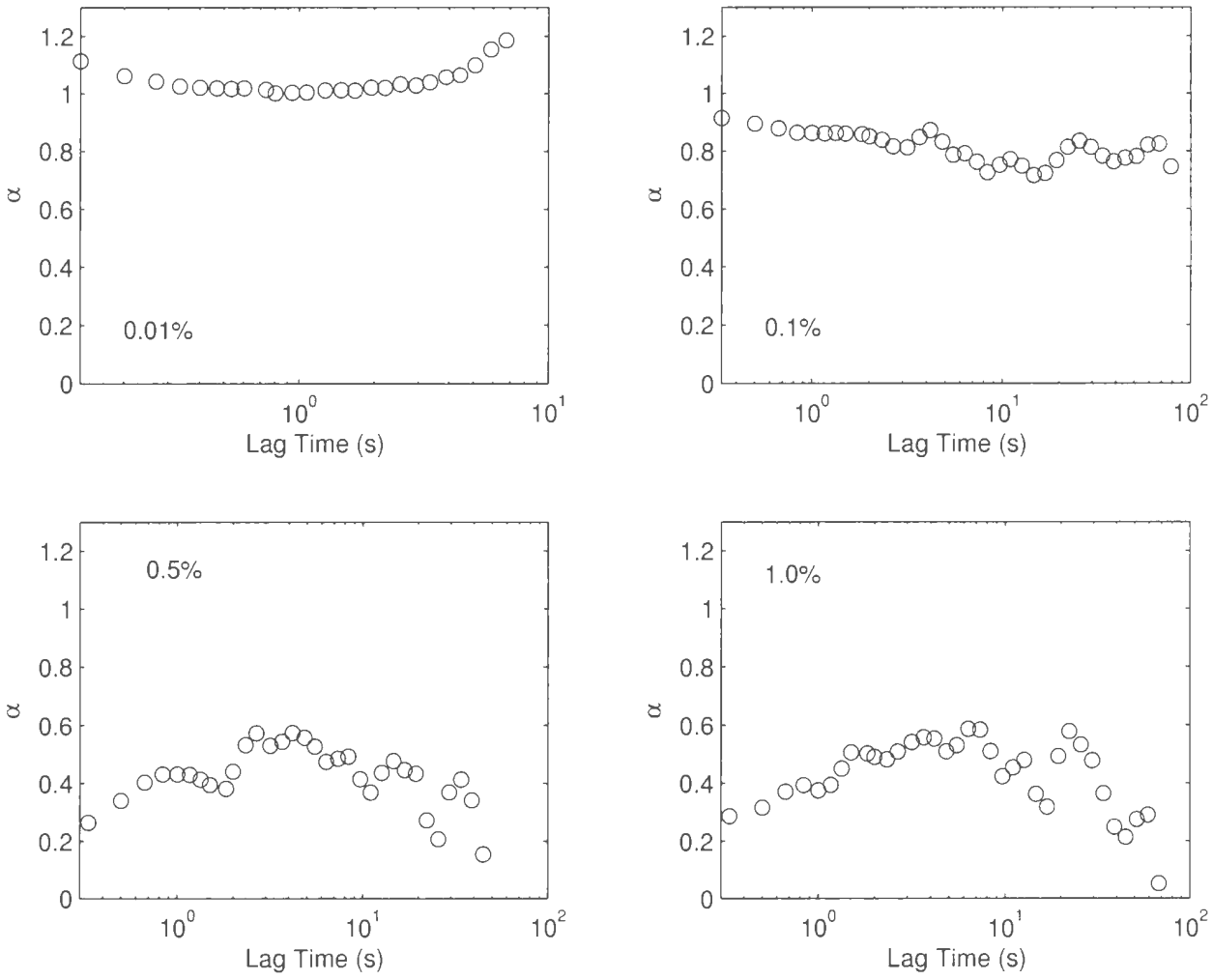

Figure 4.8: The diffusive exponent of the 0.49 μm spheres as a function of lag time for different concentrations of carbopol.

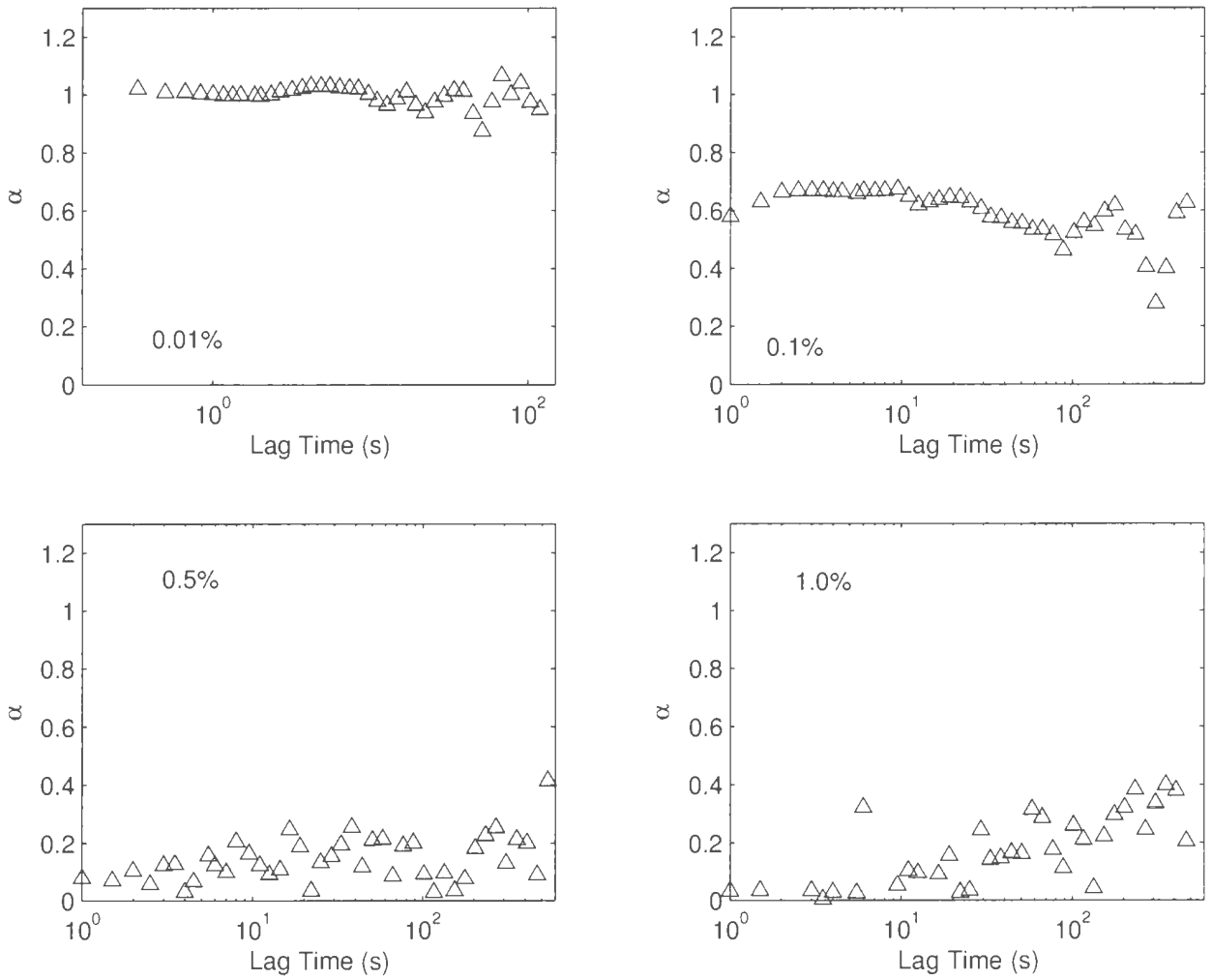

Figure 4.9: The diffusive exponent of the 1.0 μm spheres as a function of lag time for different concentrations of carbopol.

$\alpha(\tau)$ for both spheres in the 0.01% samples is close to one at all lag times studied, indicating diffusive motion in both cases. For the 0.1% concentrations, $\alpha < 1$ at all times for both spheres. This indicates subdiffusive motion. The values of α are high enough to suggest a significant degree of motion for the spheres at all times. This means that, as found above, the motion of the spheres is affected by the microenvironment, but the effect at this concentration is not strong enough to completely prevent the sphere from moving. At this concentration the motion of the spheres is just slightly restricted. Even if caging does occur, it is not permanent, but the spheres are able to escape with time. This behaviour is consistent with the trajectories observed at this concentration (see Fig. 4.1D and 4.3D). The particles are able to wander away with time, probably because the pores are not well formed or small enough to confine the spheres. At this concentration, α tends to decrease slightly with increasing τ. This means that at longer lag times, as the particle moves longer distances, the tendency for the structures in the fluid to constrain its motion becomes stronger.

For the 0.5 and 1.0% concentrations we observe that α is relatively low compared to the lower concentrations and also shows a higher degree of variability. There is a systematic variation in the values for the 0.49 μm spheres. They are low at small lag times, rise to a maximum around $\tau = 3$ s , then approach zero at longer times. This behaviour confirms our earlier conclusions that the spheres are confined within pores in the fluid. At small times they are less diffusive, they become more

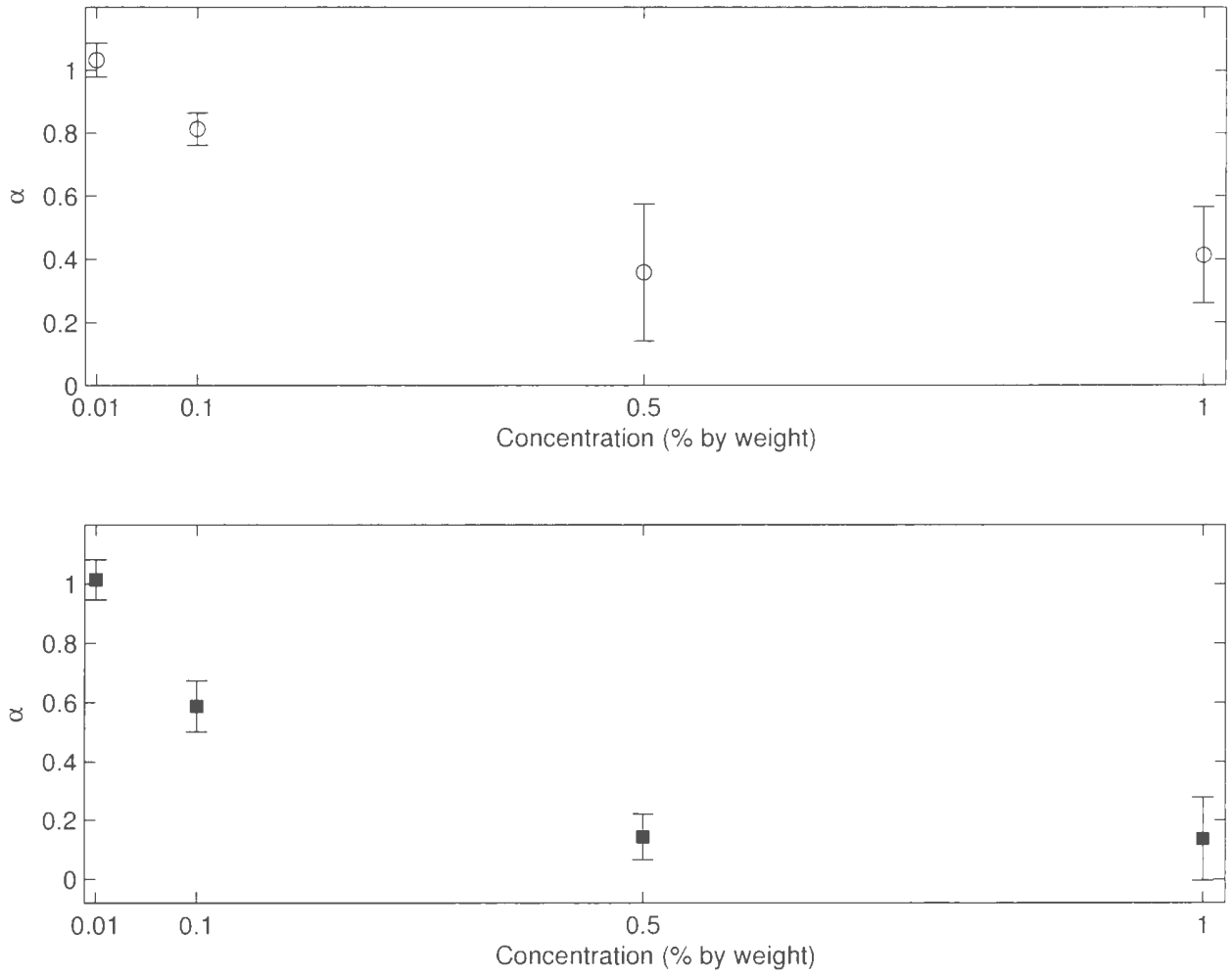

Figure 4.10: The diffusive exponent averaged over lag time and shown as a function of concentration. The top plot (open circles) represents the 0.49 μm spheres while the bottom plot (closed squares) represents the 1.0 μm spheres.

diffusive at intermediate times and at very long times, they are more constrained by the structures in the fluid and become less diffusive again. The 1.0 μm spheres have α close to zero at all lag times suggesting very little or no motion at all. This supports our earlier claim that the spheres are trapped within the pores and therefore cannot move appreciably.

The time-averaged diffusive exponents are shown in Fig. 4.10 as a function of

concentration. The error bars are the standard deviations. The errorbars are larger for the higher concentrations due to the systematic variation in α as discussed above. We observe for both spheres that decreases with increasing concentration. At high concentrations as the fluid becomes more structured, the motion of the spheres becomes more constrained. At all concentrations above 0.01%, the 0.49 μm spheres have higher values of α than the 1.0 μm spheres. This implies that the smaller spheres have a higher mobility as suggested earlier. In structured fluids, the smaller sphere stands a better chance of moving around the obstacles in the fluid that prevent free motion, compared to the larger spheres.

4.4 The van Hove Correlation Function

We investigate the distribution of the displacements as a function of lag times using the van Hove correlation function. The van Hove correlation function $P(\Delta x, \tau)$ is the probability that in a lag time τ, a particle has moved a displacement Δx. Δx is measured from the particle's initial position at $\tau = 0$. $P(\Delta x, \tau)$ is given by

$$\begin{aligned} P(\Delta x, \tau) &= \frac{1}{N}\left\langle \sum_{i=1}^{N} \delta\left[\Delta x + x_i(0) - x_i(\tau)\right]\right\rangle \\ &= \frac{N(\Delta x, \tau)}{N} \end{aligned} \tag{4.2}$$

where $N(\Delta x, \tau)$ is the number of particles with displacements Δx in lag time τ, and N is the total number of particle displacements. The angle brackets denote canonical averaging [73]. Experimentally, $P(\Delta x, \tau)$ is measured as the histogram of

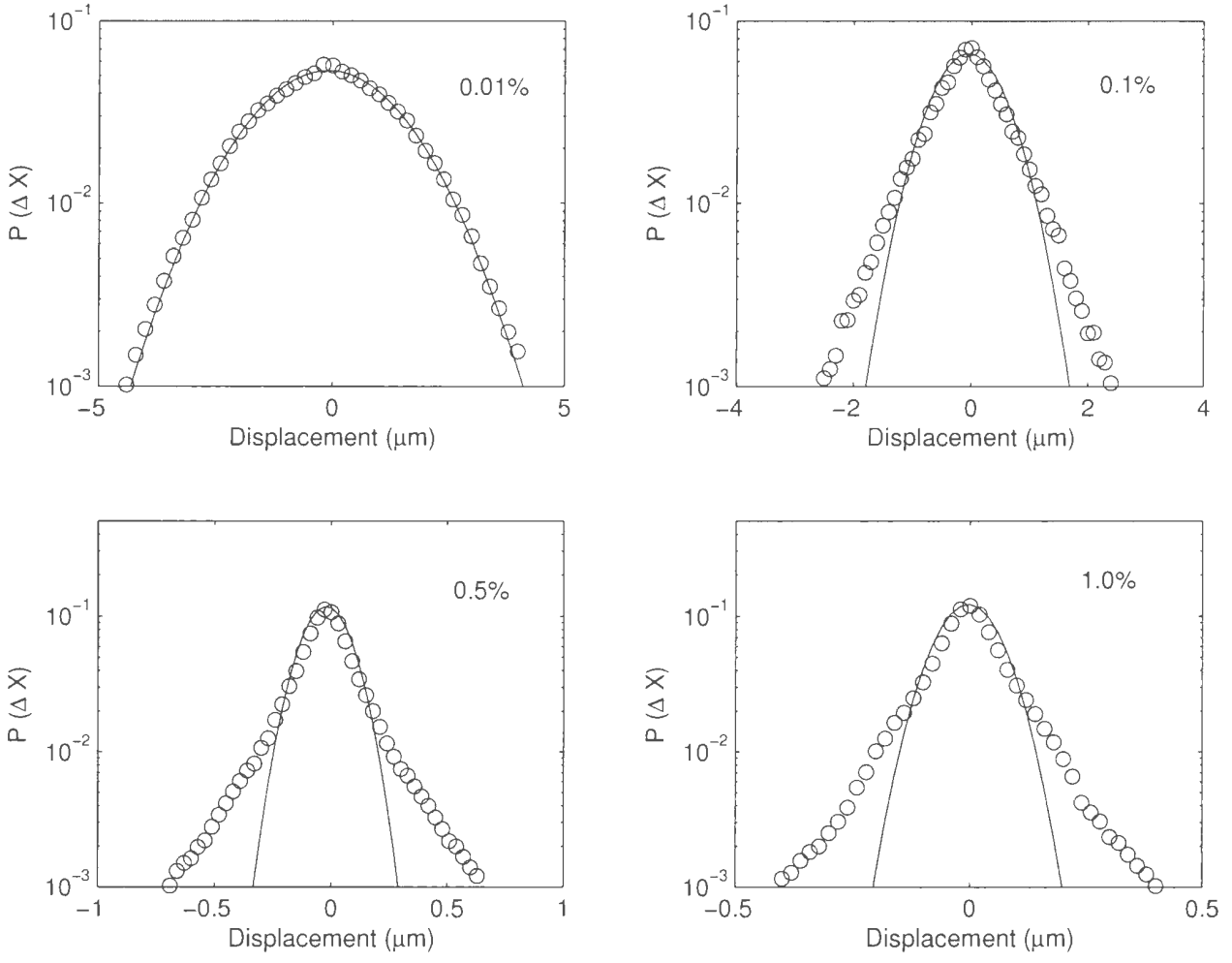

Figure 4.11: The van Hove correlation function for the 0.49 μm spheres as a function of carbopol concentration at a lag time of 3 s. The solid lines are Gaussian fits to the data.

the distribution of displacements.

The van Hove correlation functions for the 0.49 μm spheres at lag times of 3 and 10 s are shown in Figures 4.11 and 4.12 respectively. At the 0.01 % concentration, the distributions are Gaussian for both lag times. This signifies that the displacements are uniformly distributed and all particles experience the same microenvironments and undergo normal diffusion. The material is therefore homogeneous at this length scale

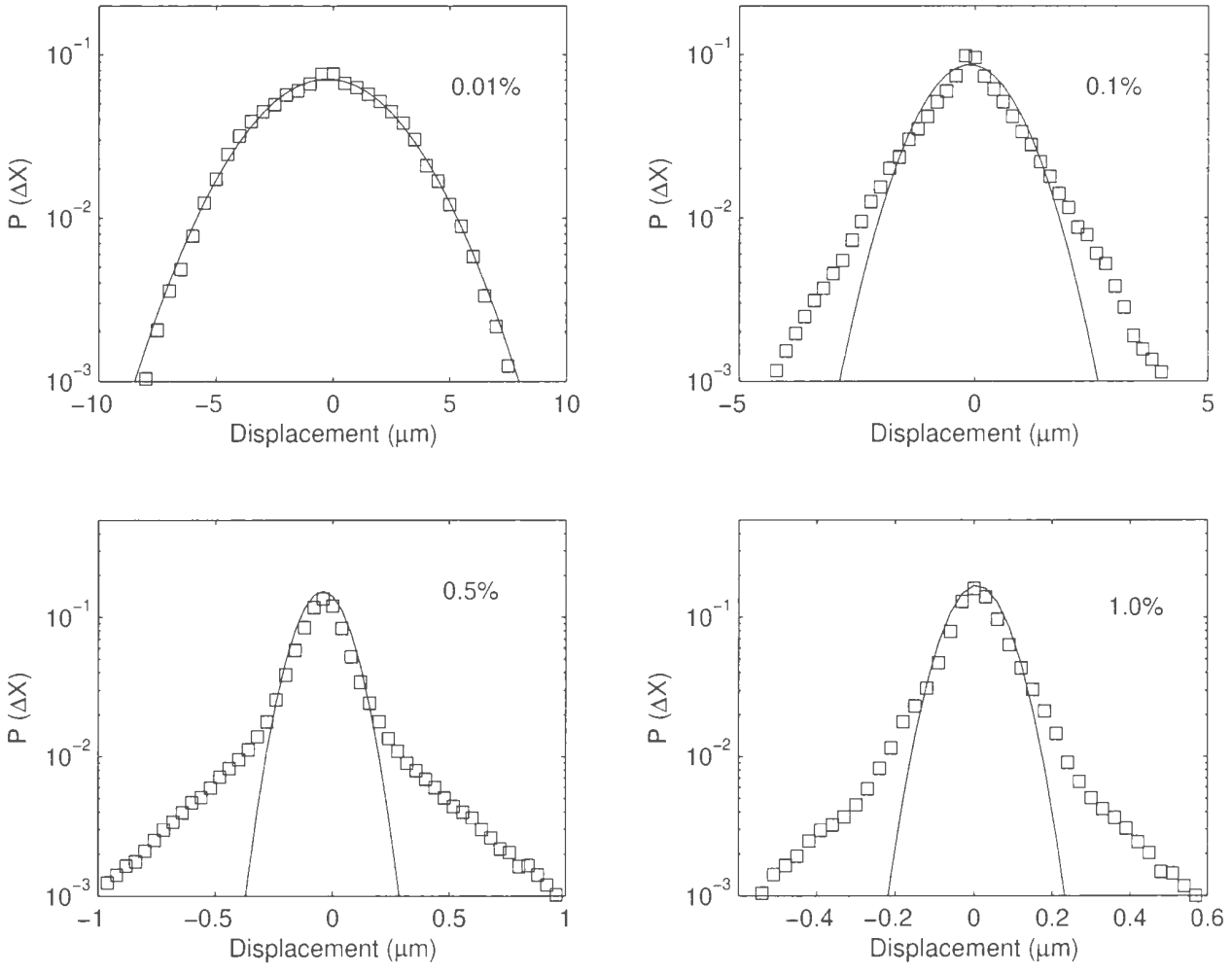

Figure 4.12: The van Hove correlation function for the 0.49 μm spheres as a function of carbopol concentration at a lag time of 10 s. The solid lines are Gaussian fits to the data.

Carbopol Sample	Diffusion Constant ($\mu m^2/s$)
0.01%	0.7494 ± 0.0037
0.1%	0.0600 ± 0.0136
0.5%	0.0017 ± 0.0004
1.0%	0.0007 ± 0.0002

Table 4.2: Diffusion coefficients for the 0.49 μm spheres in different concentrations of carbopol calculated from the width of the Gaussian fits to the van Hove Correlation Function at a lag time of 3 s.

and concentration. At higher concentrations, the distributions begin to deviate from Gaussian behaviour. For very small displacements the distribution function can be fairly well described by a Gaussian but the deviation sets in at higher displacements. Thus while the majority of the particles move only short distances, the number of large steps is much larger than would be expected if the distribution were purely Gaussian. The degree of deviation grows with concentration and lag time. This shows that the fluid becomes more structured at higher concentrations as it becomes heterogeneous. As the lag time increases, the distances travelled by the spheres increase and the probability of the spheres bumping into these structures or being restricted from further motion also increases. This explains the increased deviation from Gaussian behaviour with lag time. As discussed in Chapter 2, the width of the distributions is directly proportional to the diffusion coefficient. The diffusion coefficients calculated from the width of the distributions are shown in Table 4.2. We observe that the diffusion coefficient decreases with concentration showing that the spheres become less mobile due to increasing viscosity of the fluid.

The distributions of the displacements for the 1.0 μm spheres at lag times of 10

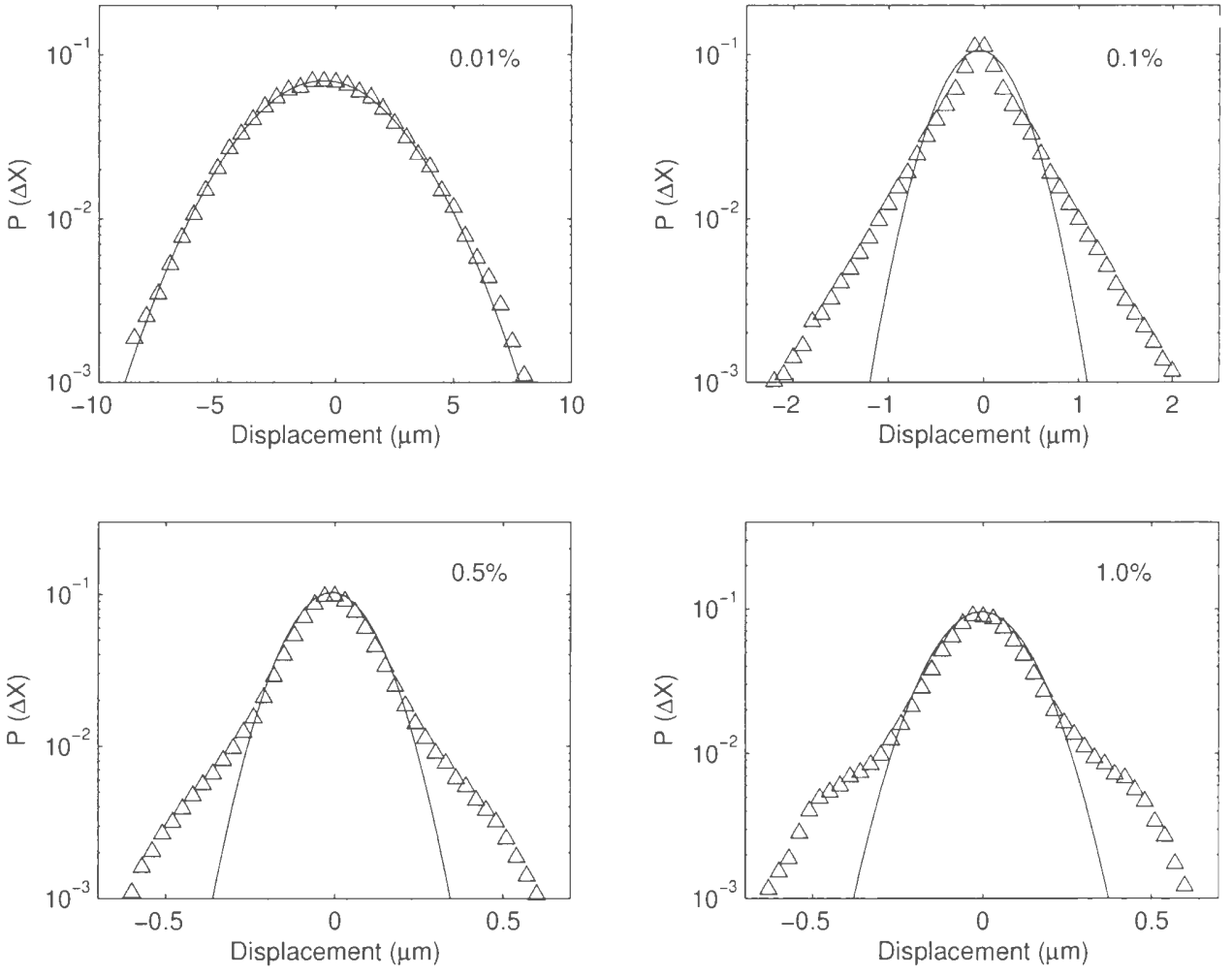

Figure 4.13: The van Hove correlation for the 1.0 μm spheres as a function of carbopol concentration at a lag time of 10 s. The solid lines are Gaussian fits to the data.

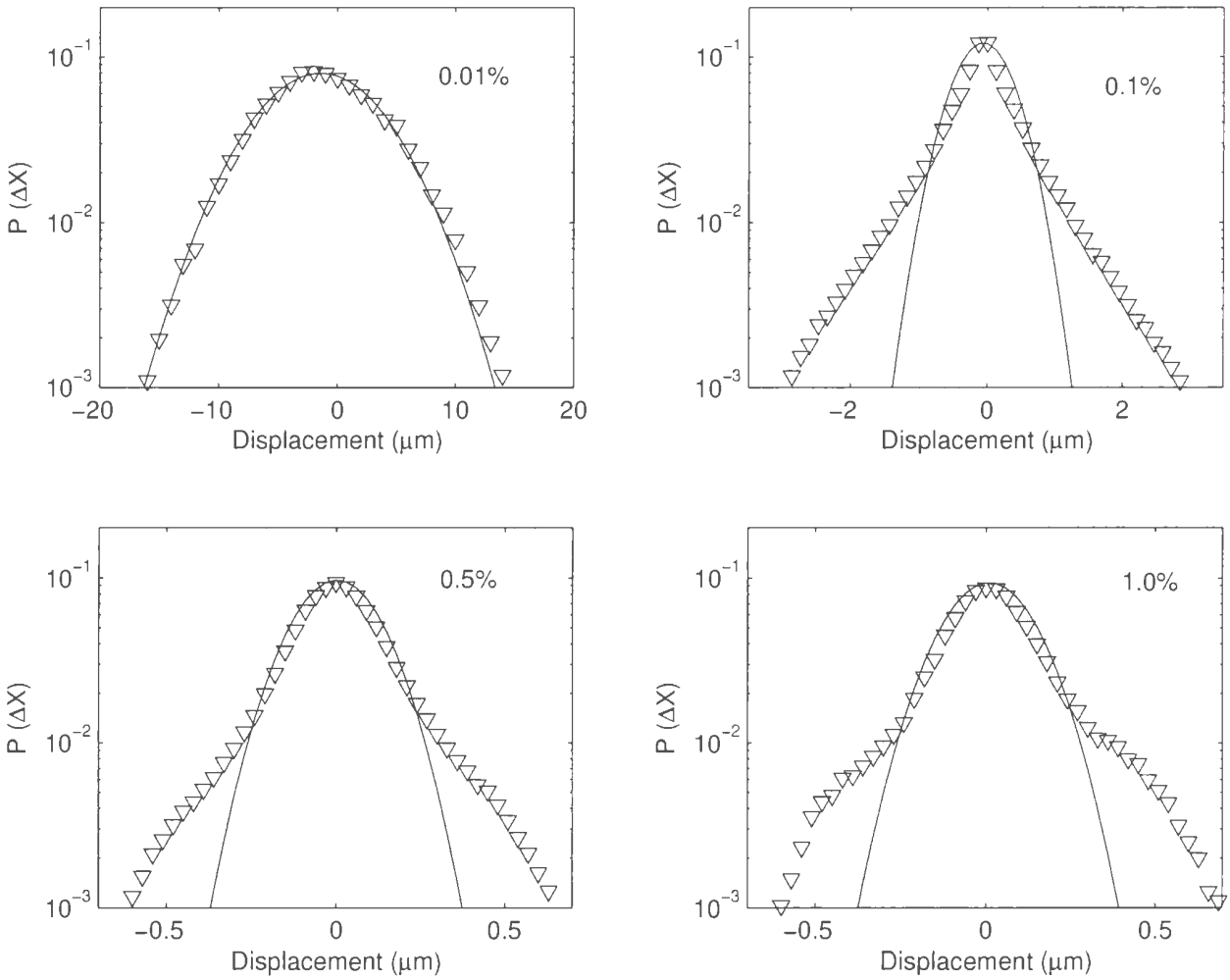

Figure 4.14: The van Hove correlation function for the 1.0 μm spheres as a function of carbopol concentration at a lag time of 30 s. The solid lines are Gaussian fits to the data.

Carbopol Sample	Diffusion Constant ($\mu m^2/s$)
0.01%	0.3900 ± 0.0131
0.1%	0.0070 ± 0.0073
0.5%	0.0007 ± 0.0004
1.0%	0.0008 ± 0.0006

Table 4.3: Diffusion coefficients for the 1.0 μm spheres in different concentrations of carbopol calculated from the width of the Gaussian fits to the van Hove Correlation Function. The lag time for the 0.01% and 0.1% samples is 3 s while that for the 0.5% and 1.0% samples is 10 s.

and 30 s are shown in Figures 4.13 and 4.14 respectively. At a concentration of 0.01% the distributions are Gaussian at both lag times, again indicating that the fluid is homogenous on this length scale as well. Deviations from Gaussian behaviour are again observed at higher concentrations for the same reasons as given above. The distribution for the 0.1% concentration exhibits peculiar behaviour at both lag times. At this concentration the distribution is non-Gaussian even at the smallest displacements and is approximately described by an exponential distribution. Similar behaviour has been observed experimentally in agarose gels by Valentine et al. [8] A theoretical prediction of this behaviour has been made by Metzler and Klafter [23], who reported that such a distribution is a signal of subdiffusive motion with a diffusive exponent of 0.5. We find that at this concentration the diffusive exponents at lag times of 10 and 30 s are 0.67 and 0.60 respectively which is higher than the theoretical prediction. As in the case of the smaller spheres, the width of the distributions decreases with concentration showing that the spheres become more restricted by the structure of the fluid with increasing concentration. The estimates for the

diffusion coefficients are given in Table 4.3. The diffusion coefficient decreases with concentration as the viscosity of the fluid increases.

By comparing the distributions for the two spheres at lag time of 10 s (Figs. 4.12 and 4.13). we observe that the 0.49 μm data are characterized by relatively higher displacements. This is due to the higher mobility of the smaller spheres as discussed above. Deviations in the 0.49 μm spheres are also higher than those in the 1.0 μm distributions. This will be quantified in the next section. As before this is due to the fact that the more mobile spheres have a higher possibility of interacting more with the structures in the material and hence will probe the heterogeneities more.

4.5 The Non-Gaussian Parameter

In this section we seek to quantify the degree of deviation from Gaussian behaviour by calculating the non-Gaussian parameter (NGP) as a function of time and concentration. The NGP, which compares the fourth moment of the particle displacement to the second moment, is defined by [73]

$$NGP = \frac{\langle x^4(\tau)\rangle}{3\langle x^2(\tau)\rangle^2} - 1. \tag{4.3}$$

The NGP is related to the kurtosis, which measures how peaked (positive kurtosis) or broad (negative kurtosis) a distribution is. If we multiply the NGP by a factor of 3, we get the exact expression for the kurtosis. NGP > 0 indicates a sharper, more peaked distribution while NGP< 0 indicates a broader and flatter distribution. For a

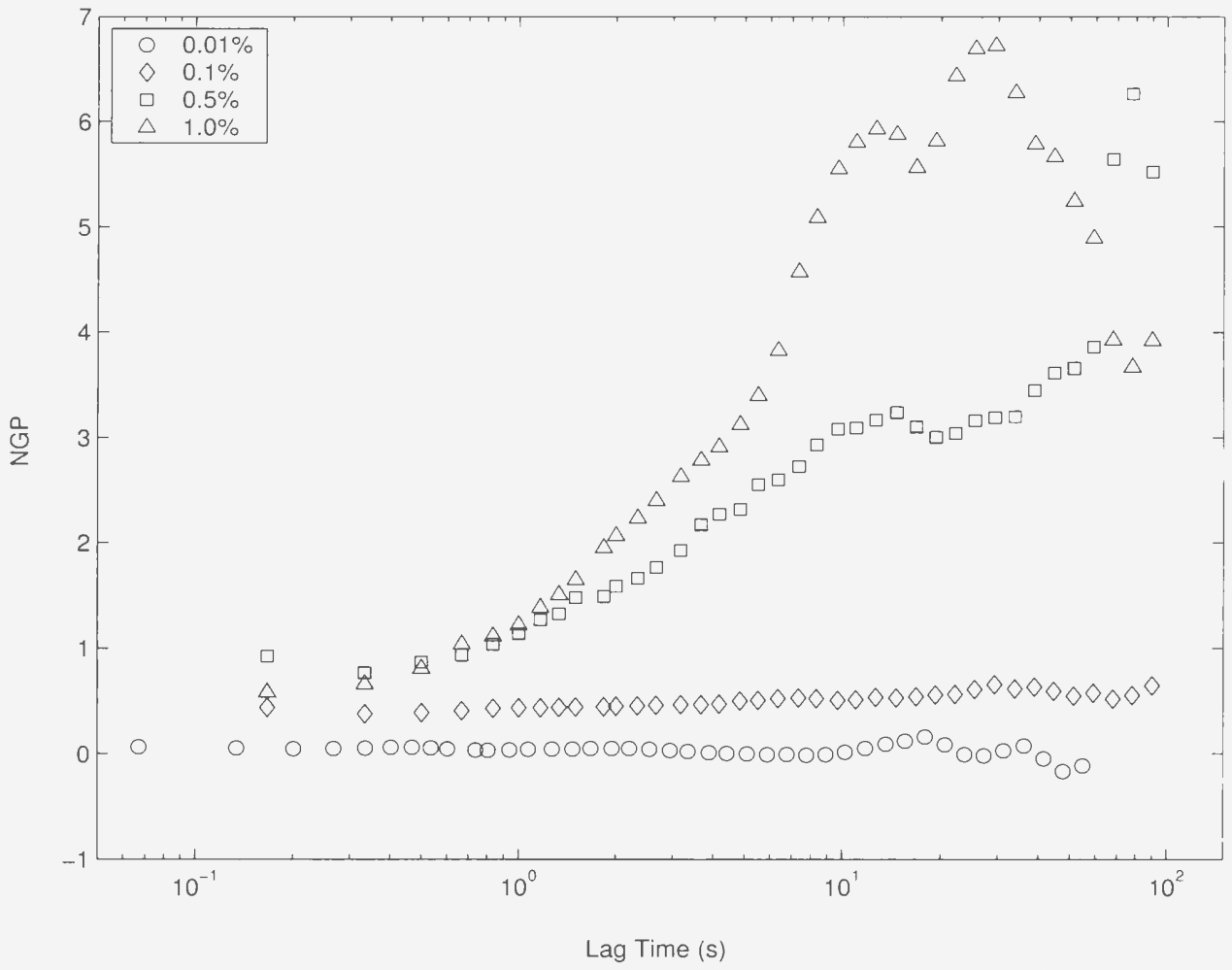

Figure 4.15: The non-Gaussian parameter for the 0.49 μm spheres as a function of lag time. The different symbols represent the different concentrations as indicated.

purely Gaussian distribution, $\langle x^4(\tau)\rangle = 3\langle x^2(\tau)\rangle^2$ and NGP is zero [74]. A non-zero value signifies a deviation from Gaussian behaviour, and the greater the value of the NGP, the greater the deviation.

Figure 4.15 shows the non-Gaussian parameter at different concentrations as a function of lag time for the 0.49 μm spheres. At 0.01%, the NGP is zero at all accessible times, confirming the fact that the motion is diffusive at this concentration.

At 0.1%, the NGP is slightly greater than zero but fairly constant at all times. This suggests that the effect of the fluid environment on the motion is mild and almost independent of the distance the particle travels. For the 0.5 and 1.0% concentrations, the NGP is highly dependent on lag time. At smaller lag times, the NGP increases steadily until after ~10 s where the increase is more rapid. At long times, the rise is far less rapid and for the 1.0% data, it actually begins to decrease. This can be interpreted to mean that at short lag times, the motion of the spheres is closer to being diffusive and they do not feel the effect of the pore walls much. At longer times, the pores constrain the motion, leading to higher values of the NGP. At very long times, the spheres may escape from the pores or the structure of the fluid may itself evolve. This leads to a decrease in the NGP at large lag times.

The NGP for the 1.0 μm spheres is shown in Fig. 4.16. At 0.01% the NGP is zero at all times, indicating diffusive motion and a homogeneous microenvironment. As before, the NGP is lag time dependent at higher concentrations. At higher concentration, the NGP is fairly constant for short lag times, then begins to grow at higher lag times for the reasons discussed above.

Figure 4.17 compares the NGP for the two sphere sizes at the two higher concentrations, where the structure effects are felt the most. The lag times at which the NGP for the 0.49 μm spheres starts to increase is about $1 - 3$ s. This is smaller compared to that of the 1.0 μm spheres, which is in the range $10 - 40$ s. This is consistent with the suggestions made above that the smaller spheres, by virtue of

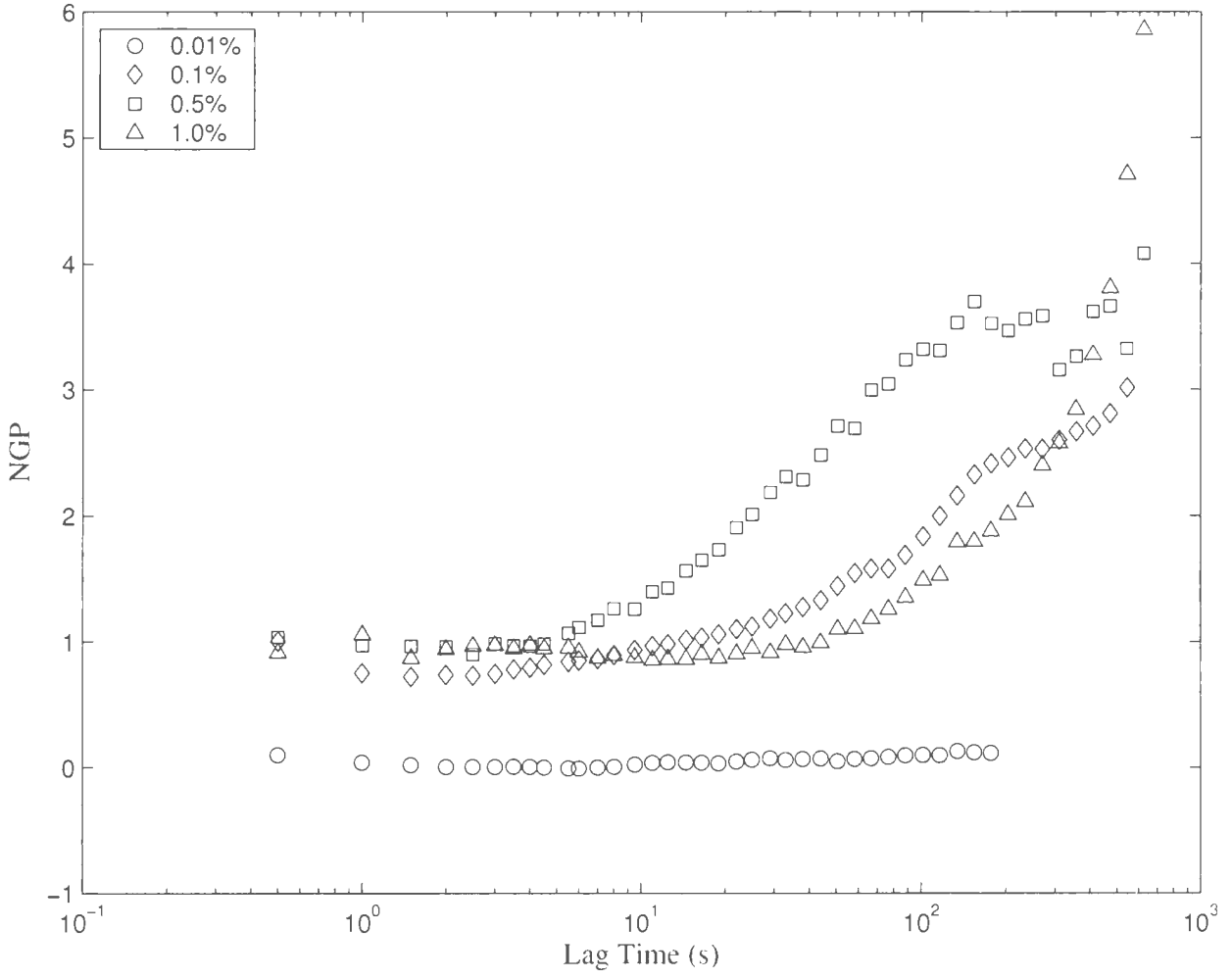

Figure 4.16: The non-Gaussian parameter for the 1.0 μm spheres as a function of lag time. The different symbols represent the different concentrations as indicated.

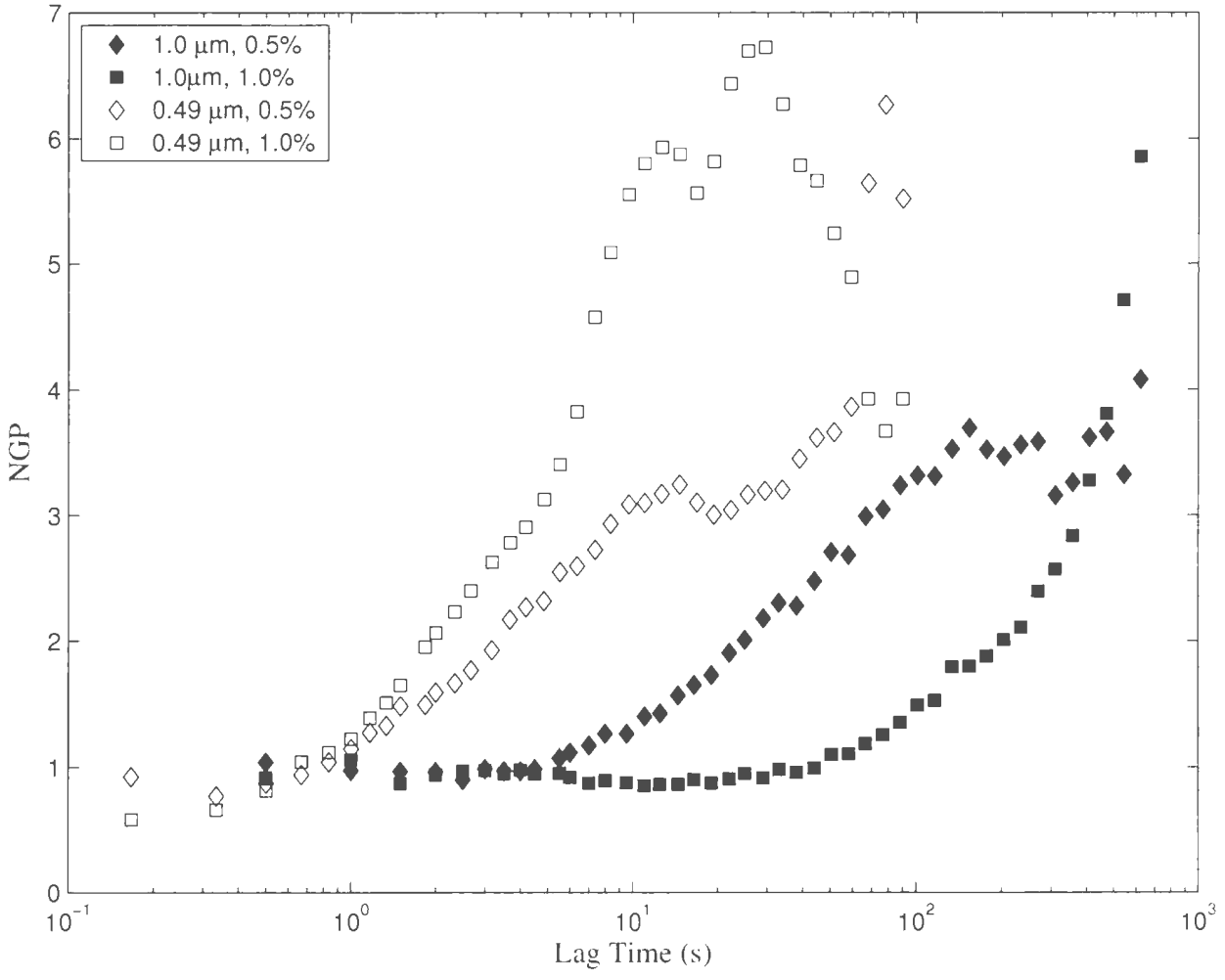

Figure 4.17: Comparison of the non-Gaussian parameters for the two spheres in 0.5 and 1.0% carbopol samples. The closed symbols represents 1.0 μm spheres while the open symbols represent 0.49 μm spheres.

their higher mobility, experience the effects of the pore walls earlier.

4.6 Temporal Correlations In Particle Motion

From the results discussed above, we have established that at higher concentrations, plateaus in the MSD signify caging of the spheres in fluid-filled pores in the material. In this section, we study in detail this caging effect, following the method developed by Doliwa and Heuer [75].

We consider two successive displacements $\vec{r}_{01}$ and $\vec{r}_{12}$ with equal lag times Δt, and determine to what extent $\vec{r}_{12}$ depends on $\vec{r}_{01}$. The displacement is defined by

$$\vec{r}_{mn} = \vec{r}(n\Delta t) - \vec{r}(m\Delta t)\,. \tag{4.4}$$

We compute the quantity $x_{12} \equiv \vec{r}_{12} \cdot \hat{r}_{01}$, which is the component of $\vec{r}_{12}$ parallel to $\vec{r}_{01}$. Here $\hat{r}_{01}$ is a unit vector. We then find the average value $\langle x_{12} \rangle$ as a function of r_{01}, where $r_{01} = |\vec{r}_{01}|$. The averaging is done over all particles and initial times [17, 75]. For dilute samples where caging does not occur, we expect $\langle x_{12} \rangle = 0$. On the other hand $\langle x_{12} \rangle$ should be negative if caging occurs. This is because in the presence of cages, particles which move in one direction during the first time interval will on average move in the opposite direction during the subsequent time interval. As the particle comes close to the walls of the pores, it is prevented from moving any further toward the walls, and will therefore tend to move in the opposite direction, away from the walls. For particles with small displacements, $\langle x_{12} \rangle$ will be linearly

proportional to r_{01}. For larger r_{01}, $\langle x_{12} \rangle$ is no longer proportional to r_{01}. There is a gradual deviation from the linear dependence. The size of the cage or pore can be estimated from r^*, the crossover point from linear to non-linear dependence [17, 75]. Particles with $r_{01} < r^*$ remains caged, and the effect of the cage is to push the particle back toward its original position. Particles with $r_{01} > r^*$ still tend to be pushed back, but not as far as predicted by the linear extrapolation from the small r_{01} behaviour. Such particles may move far enough to escape from the cage, and therefore their subsequent motion is not necessarily due only to the cage. The size of the cage, d can be estimated as $d \approx 2a + r^*$ where a is the radius of the sphere. The strength of the cage c^*, which measures the degree to which the fluid structure opposes the motion of the spheres, is defined by

$$\langle x_{12} \rangle = -c^* r_{01}. \tag{4.5}$$

Figures 4.18 and 4.19 give the distribution of x_{12} as a function of r_{01} at different concentrations of carbopol for the two particle sizes. The lag time for the 0.01% data are 1 s. All the other concentrations have a lag time of 10 s. We observe that the distributions are symmetric about $\langle x_{12} \rangle = 0$ at low concentrations, but a significant negative correlation is observed for the higher concentrations. As suggested by Doliwa and Heuer [75], the pore effect can be separated into two parts: a deterministic part which tends to drive the particle back to its previous position and a stochastic part, allowing for stochastic motion around the new equilibrium position.

Figure 4.20 shows the relationship between $\langle x_{12} \rangle$ and r_{01} for both spheres in

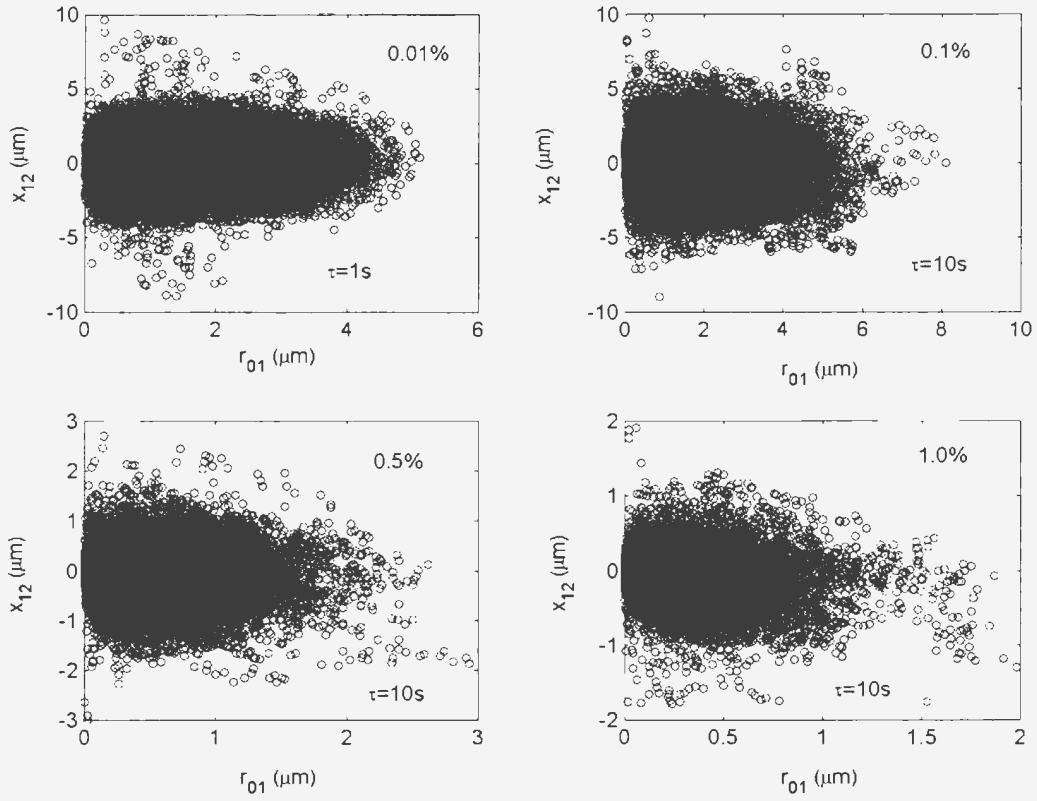

Figure 4.18: Distribution of x_{12} as a function of r_{01} for the 0.49 μm spheres at different carbopol concentrations. The lag time for the 0.01% data is 1 s while for all the other runs it is 10 s.

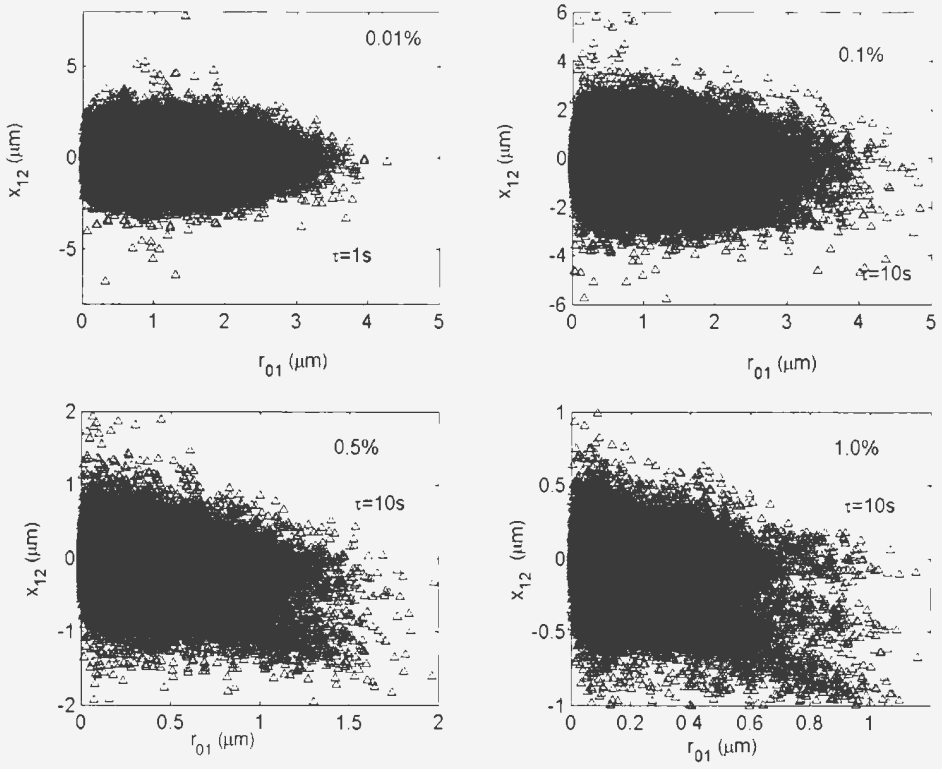

Figure 4.19: Distribution of x_{12} as a function of r_{01} for the 1.0 μm spheres at different carbopol concentrations. The lag time for the 0.01% data is 1 s. All the other concentrations have a lag time 10 s.

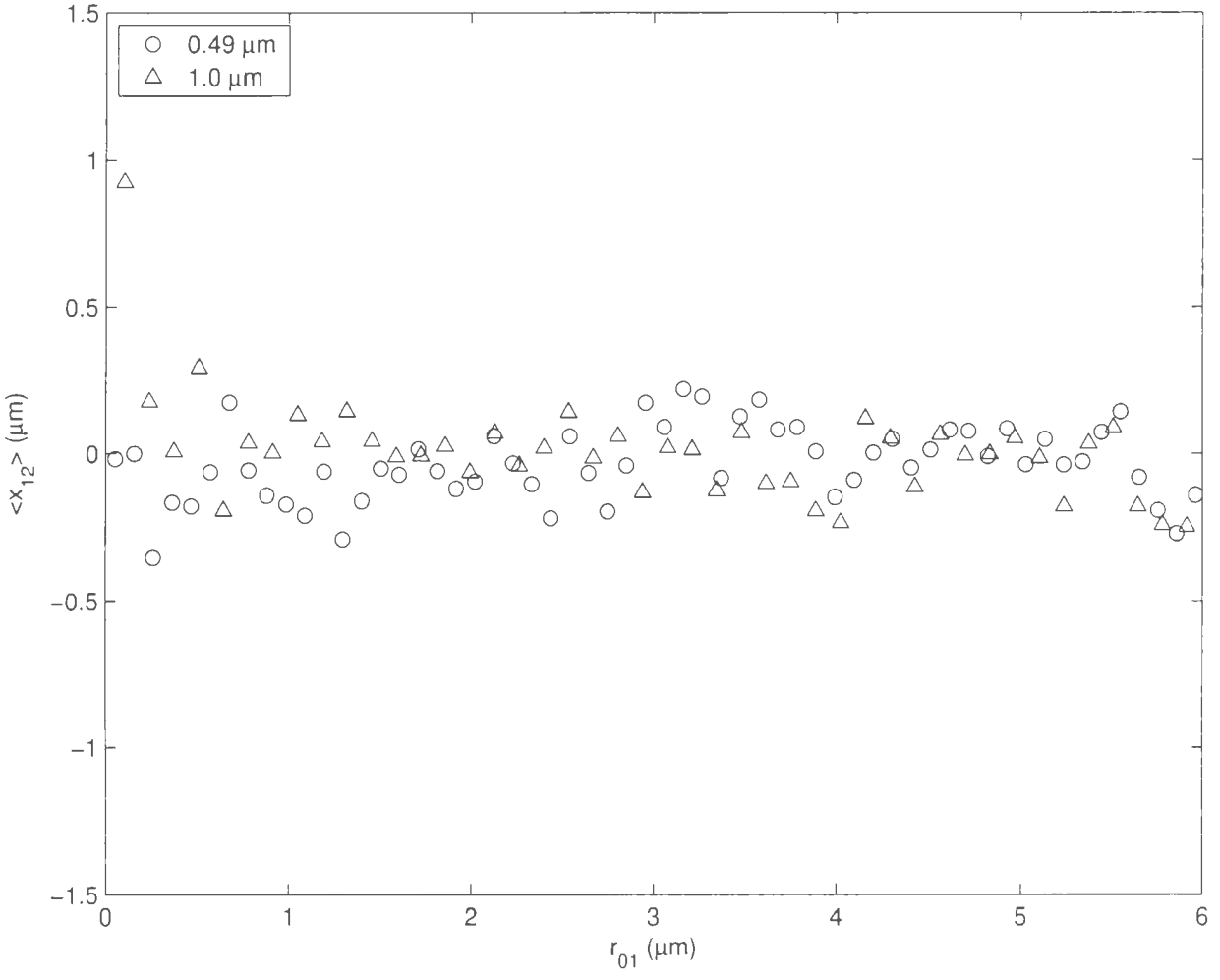

Figure 4.20: Dependence of $\langle x_{12} \rangle$ on r_{01} for the two sphere sizes in 0.01% carbopol. The lag time is 1 s.

Carbopol	Pore Size (μm) 0.49 μm spheres		Pore Size (μm) 1.0 μm spheres	
(%)	Correlation Analysis	MSD Plateau	Correlation Analysis	MSD Plateau
0.1	1.80 ± 0.08	-	1.82 ± 0.37	-
0.5	0.73 ± 0.06	0.79 ± 0.01	1.51 ± 0.02	1.20 ± 0.01
1.0	0.73 ± 0.04	0.73 ± 0.01	1.32 ± 0.02	1.22 ± 0.01

Table 4.4: Estimates of the pore size calculated from the point at which the data in Figs. 4.21 to 4.23 start to deviate from the linear behaviour shown at low displacements. These values are compared with those calculated earlier from the MSD plateaus.

0.01% carbopol at a lag time of 1 s. $\langle x_{12} \rangle$ for both spheres is zero without the scatter which may be due to decreasing data points. This shows that the probability of the sphere moving in the negative or positive direction relative to the initial displacement r_{01} is the same, and there is no dependence on r_{01}. Hence we conclude that at this concentration, the motion of the spheres is random and the influence of the structure on the motion of the spheres is negligible.

Figures 4.21 to 4.23 show the same relationship for the higher concentrations. We observe that in all cases and for all r_{01}, $\langle x_{12} \rangle$ is negative. This implies that on average, the sphere moves in opposite direction to the direction of the preceding step. This is a clear signature of the pore effect. The spheres in the fluid are confined within pores, and as they hit the walls of the pores, they bounce back in the opposite direction. We can estimate the pore size using the method described above. We fit a straight line to the data for small r_{01} and determined the point r^* at which the linear correlation breaks down. A comparison of the results obtained using this method and those calculated earlier using the MSD plateaus discussed in Sec. 4.3 are shown

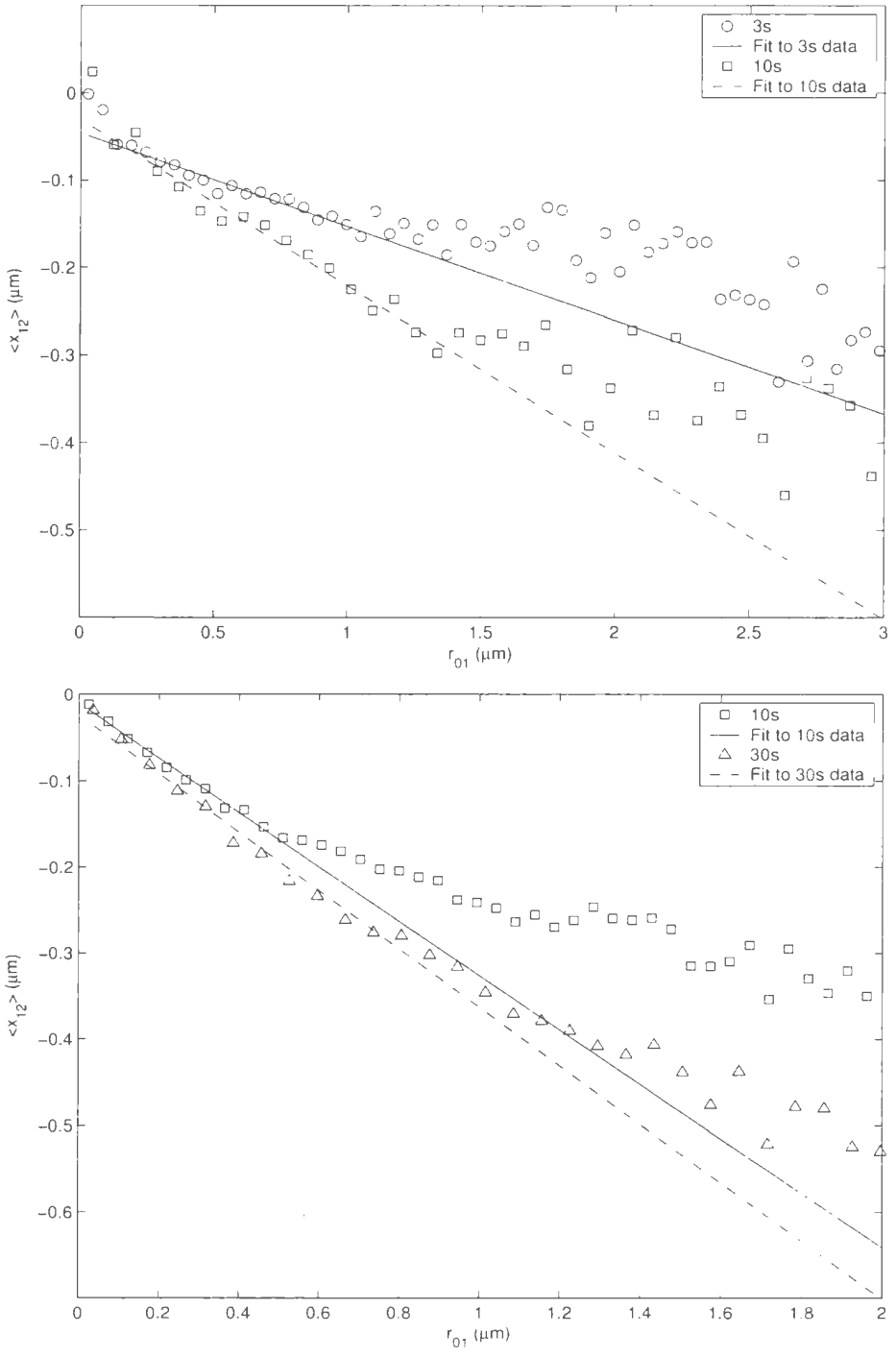

Figure 4.21: $\langle x_{12} \rangle$ as a function of r_{01} for both sphere sizes in 0.1% carbopol. The top graph is for the 0.49 μm spheres. The bottom plot is for the 1.0 μm spheres. Different lag times are indicated by different symbols as shown.

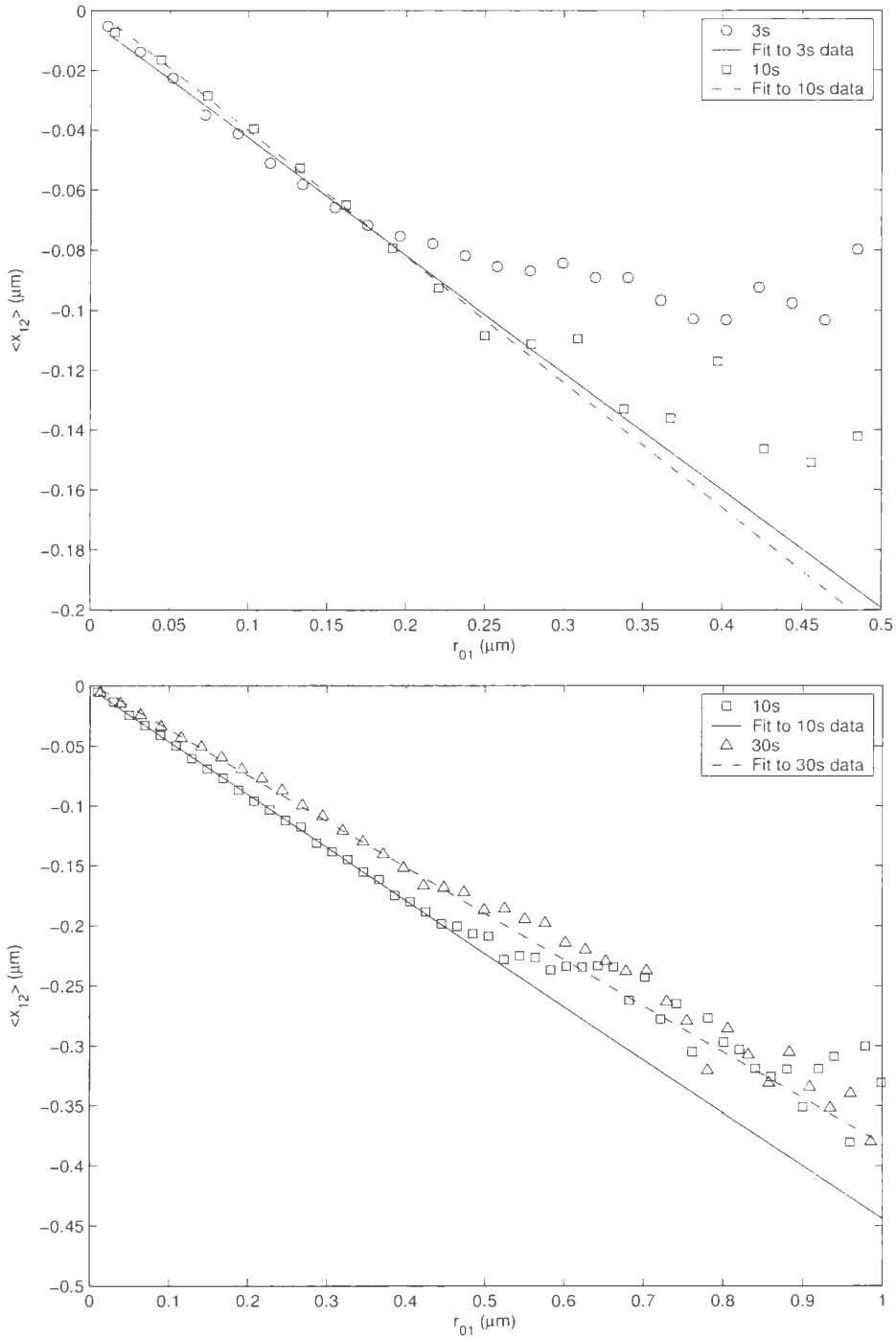

Figure 4.22: $\langle x_{12} \rangle$ as a function of r_{01} for both sphere sizes in 0.5% carbopol concentration. The top graph is for the 0.49 μm spheres. The bottom plot is for the 1.0 μm spheres. Different lag times are indicated by different symbols as shown.

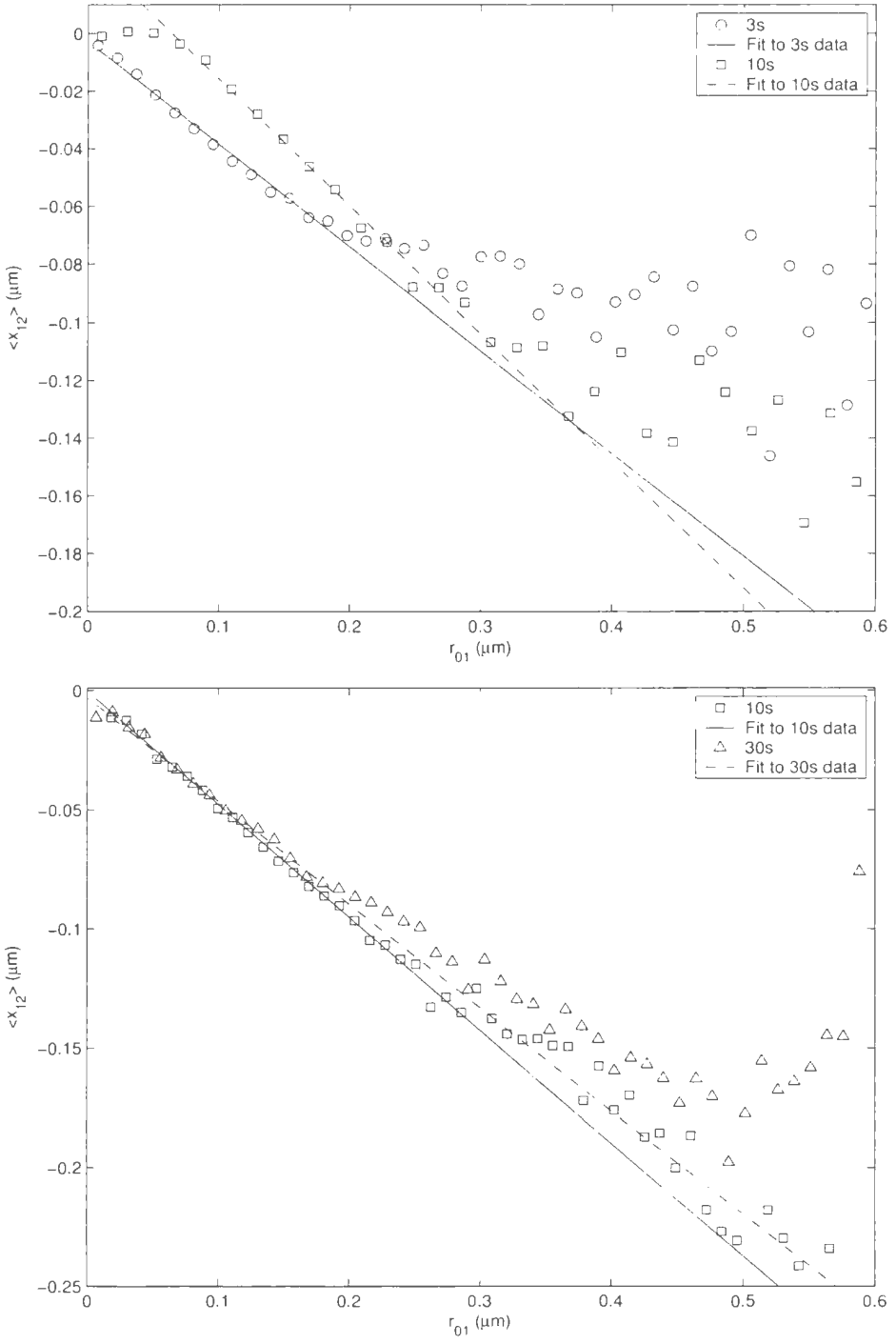

Figure 4.23: $\langle x_{12} \rangle$ as a function of r_{01} for both sphere sizes in 1.0% carbopol. The top graph is for the 0.49 μm spheres. The bottom plot is for the 1.0 μm spheres. Different lag times are indicated by different symbols as shown.

in Table 4.4. The estimates from the two methods are in good agreement. To the nearest micron, we infer from our results that the pore size is about 2 μm for the 0.1% concentration and about 1 μm for the 0.5% and 1.0% concentrations. We observe that the pore size decreases with increasing concentration. As the concentration increases, the swollen microgels fill more volume of the fluid, leading to smaller pores. For the 0.5% and 1.0% concentrations, the pore size is very comparable to the size of the sphere. This confirms our earlier assertion that the spheres are likely completely trapped at these concentrations. Again we see that at these concentrations, there is a large difference between the pore size estimates calculated from the two sphere sizes. This may be due to the fact that the spheres can only probe pores larger or comparable to their own size, and will not feel any pores smaller than themselves. Hence the pore size estimates at these concentrations are biased by the particle size.

The pore strength c^* is determined from the slope of the linear portion of the data. The results are shown in Figure 4.24. The pore strength tends to increase with concentration as the pores becomes smaller and their constraining effect increases. In all cases, the pore strength as measured by the 1.0 μm spheres is slightly higher than that for the 0.49 μm spheres, indicating that the larger spheres feel the constraining effect of the pores more strongly.

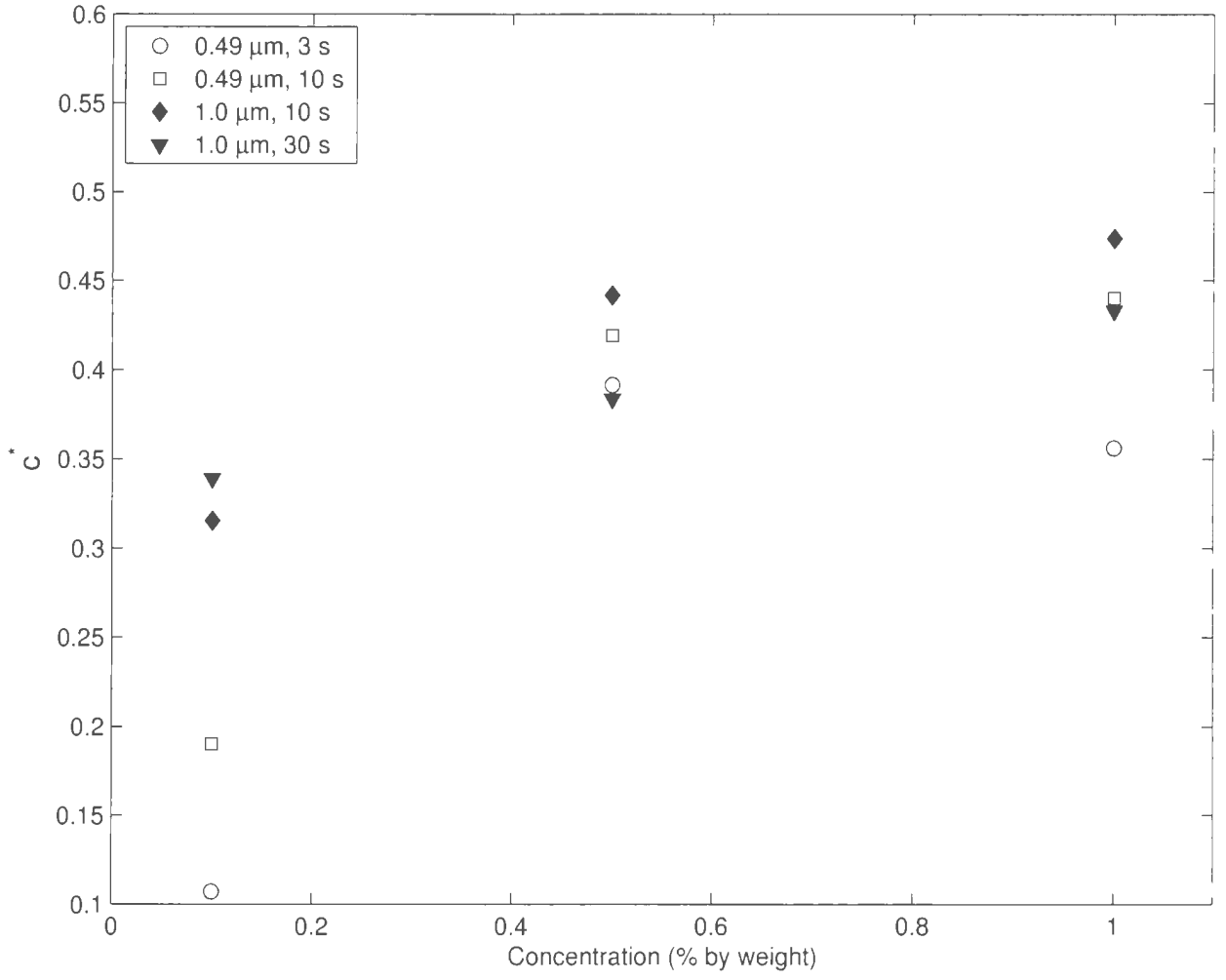

Figure 4.24: The pore strength calculated from the slope of the fits to the linear dependence of $\langle x_{12} \rangle$ on r_{01} for the two spheres sizes at the lag times shown.

Chapter 5

Results and Discussion: Laponite

5.1 Introduction

Laponite was studied using two sets of samples. First, laponite samples of a fixed concentration were studied as a function of time after preparation. Measurements of the tracer particle positions were made at 3 to 6 hour intervals for a 24 hour period using laponite at a concentration of 1.5%. Measurements were started 30 minutes after sonication. Second, samples of different concentrations were prepared, sonicated, and allowed to stand for approximately 48 hours before measurements were made. These measurements allowed us to investigate how the colloidal particle concentration affects the fluid properties, while the first set of measurements enabled us to study the changes that occur as the laponite gels. In both cases, only the 0.49 μm spheres were suspended in the fluid. The same techniques used in analysing the carbopol data and described in detail in Chapter 4 were also used in the work presented in this chapter. We discuss results for laponite as a function of sample age

at a fixed concentration in Sec. 5.2 and as a function of concentration at fixed age in Sec. 5.3.

5.2 Laponite as a Function of Age at Fixed Concentration

5.2.1 Particle Trajectories

Figures 5.1 and 5.2 show the trajectories of the spheres in a 1.5% suspension at different times. With time, the trajectories become more compact, signaling reduced motion as the fluid evolves from the sol to the gel state. The individual trajectories for times $t = 0$ and 6 hours (Figs. 5.1B and 5.1D) indicate random motion. However, as can be seen from the scales of the axes in the figures, (20 μm for $t = 0$h and 8 μm for $t = 6$h), the motion of the spheres decreases with time as the colloidal particles aggregate. At $t = 9$h (Fig. 5.2 A and B), the trajectories have become quite localized. The individual trajectories show that the particles remain in one region for longer times than other regions. This is a signal of trapping effects due to the formation of the structures in the fluid. After 24 hours (Fig. 5.2 C and D), the gel structure has developed to the point that the spheres are completely trapped and almost immobile.

When the samples are prepared, they are sonicated after mixing overnight. The sonication breaks down all structures in the fluid and it becomes just a suspension of individual particles. At this initial time the fluid will have a low viscosity and approximately Newtonian behaviour. With time, the colloidal particles begin to

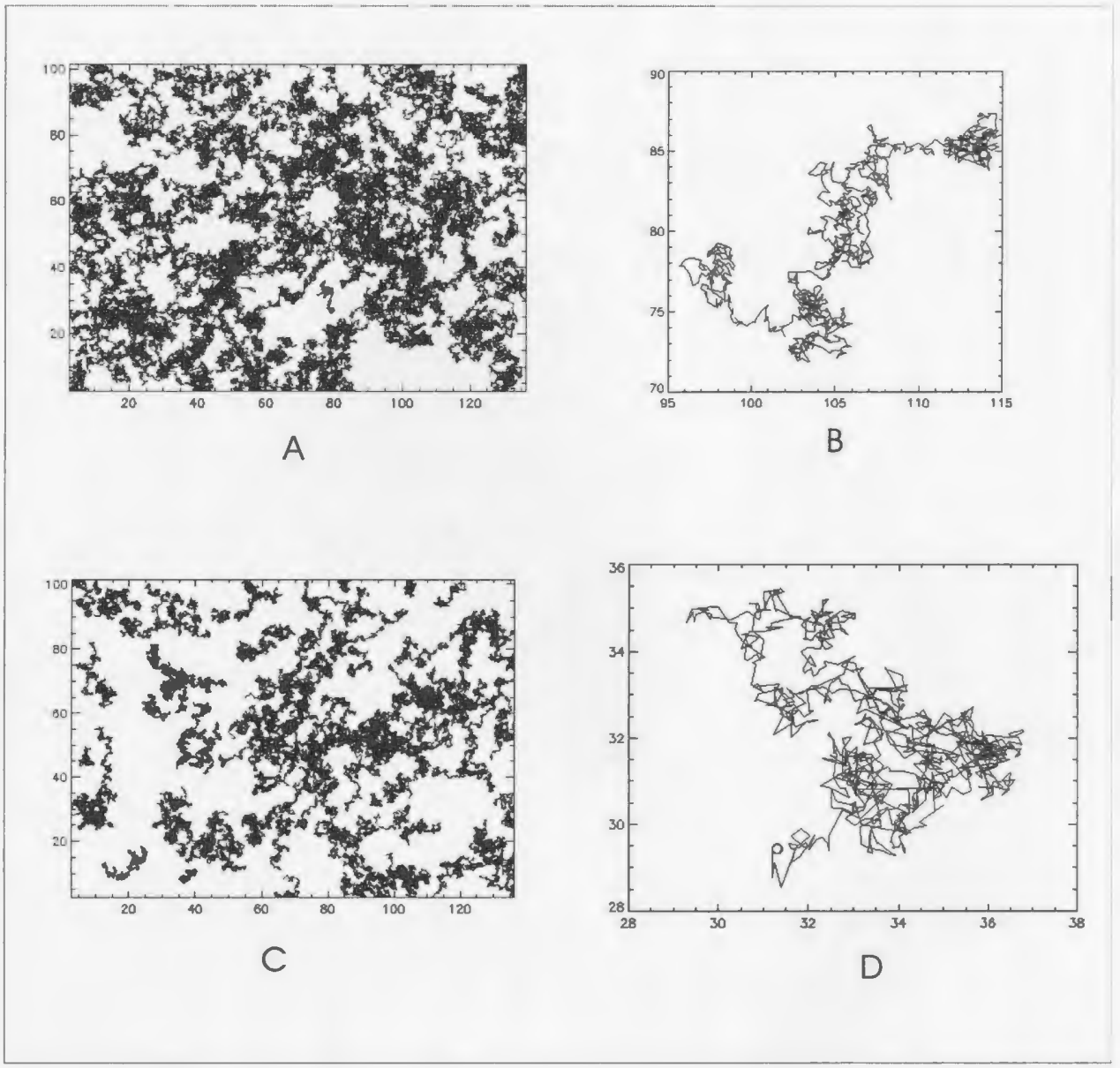

Figure 5.1: Trajectories for 0.49 μm spheres in laponite samples of ages 0h (A and B) and 6h (C and D) at a fixed concentration of 1.5%. A and C give the trajectories for all the spheres in the field of view while B and D are typical trajectories for single spheres. All the axes are in μm.

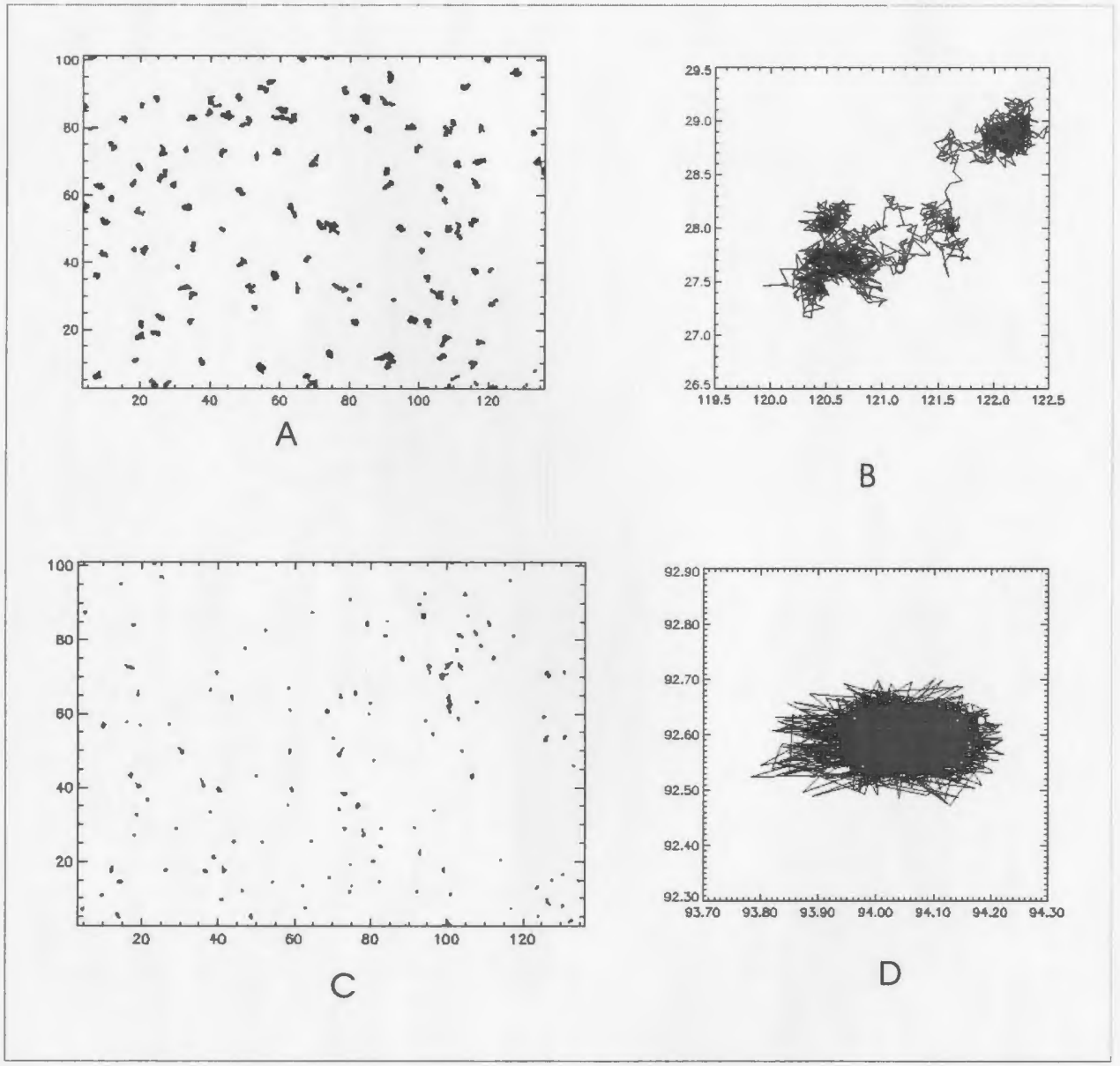

Figure 5.2: Trajectories for 0.49 μm spheres in laponite samples of ages 9h (A and B) and 24h (C and D) at a fixed concentration of 1.5%. A and C give the trajectories for all the spheres in the field of view while B and D are typical trajectories for single spheres. All the axes are in μm.

aggregate as a result of interaction between them, initiating a gradual transition from the sol to the gel state. The aggregation increases with time leading to a stiffening of the gel. These aggregates or structures trap the probe particles. As a result of the formation of the gel the motion of the spheres becomes more restricted at longer times.

5.2.2 The Mean Square Displacement (MSD)

Data for the ensemble averaged mean square displacement of the spheres in the 1.5% concentration as a function of time are shown in Figure 5.3. For samples up to the age of 6 h the MSD increases linearly with lag time, indicating diffusive motion on all time scales. However the magnitude of the MSD decreases with the age of the sample. This indicates that with time, the interactions between the suspended particles increase the viscosity of the suspension which in turn reduces the mobility of the spheres. At 9 hours, we observe that the logarithmic slope of the MSD for lag times less than about 6 s is lower than for long lag times. This indicates that at this age, structure in the fluid obstructs the motion of the spheres at short lag times, while at long lag times, the spheres are able to escape from the structures. The onset of trapping may be a signal of the sol-gel transition. After 15 hours, the MSD is independent of lag time, indicating that the gel structure is very stiff to the extent that the probe particles are almost immobile.

The MSD plateau at long times may be either a measure of the local elasticity

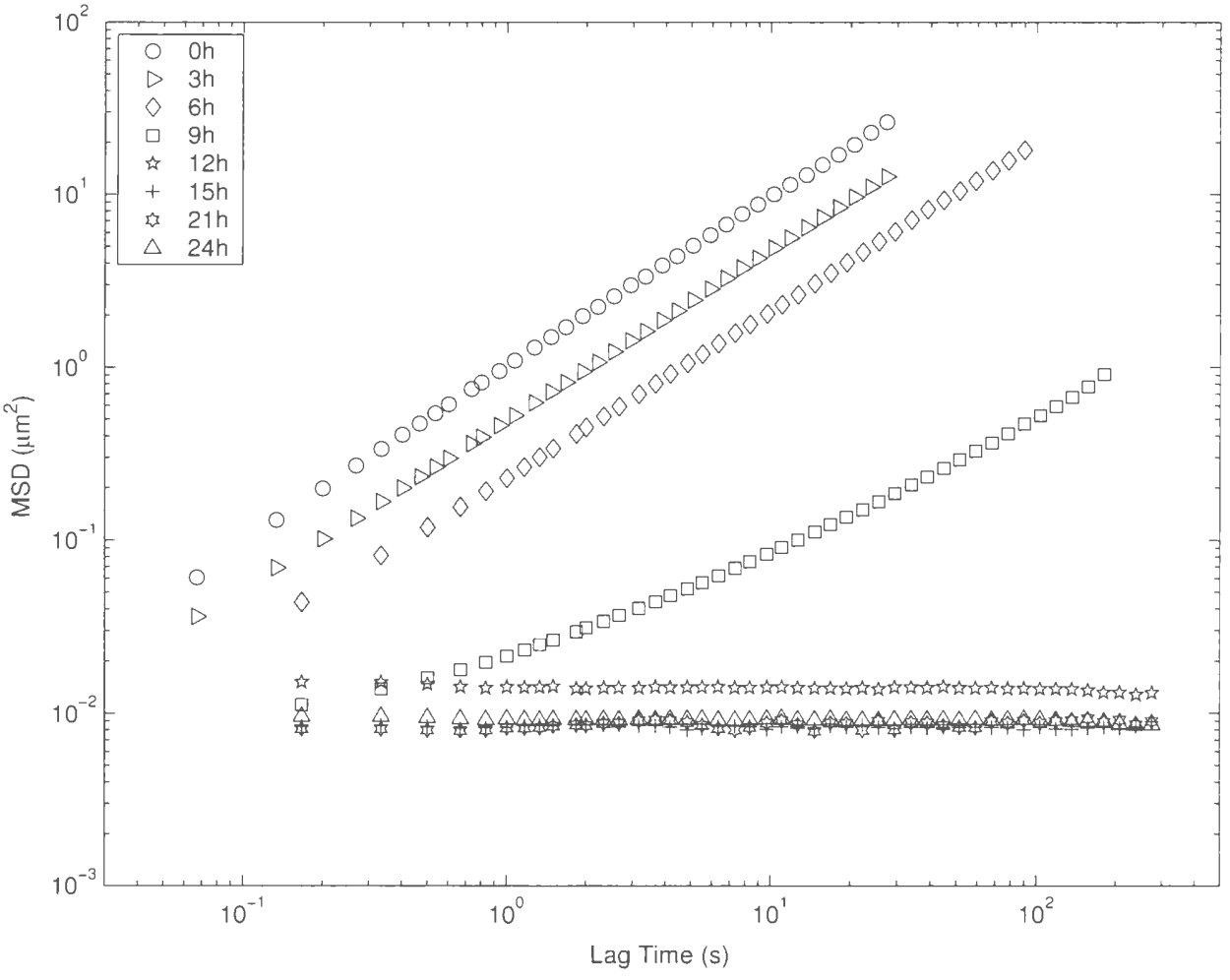

Figure 5.3: The ensemble averaged MSD as a function of age for 1.5% laponite suspension.

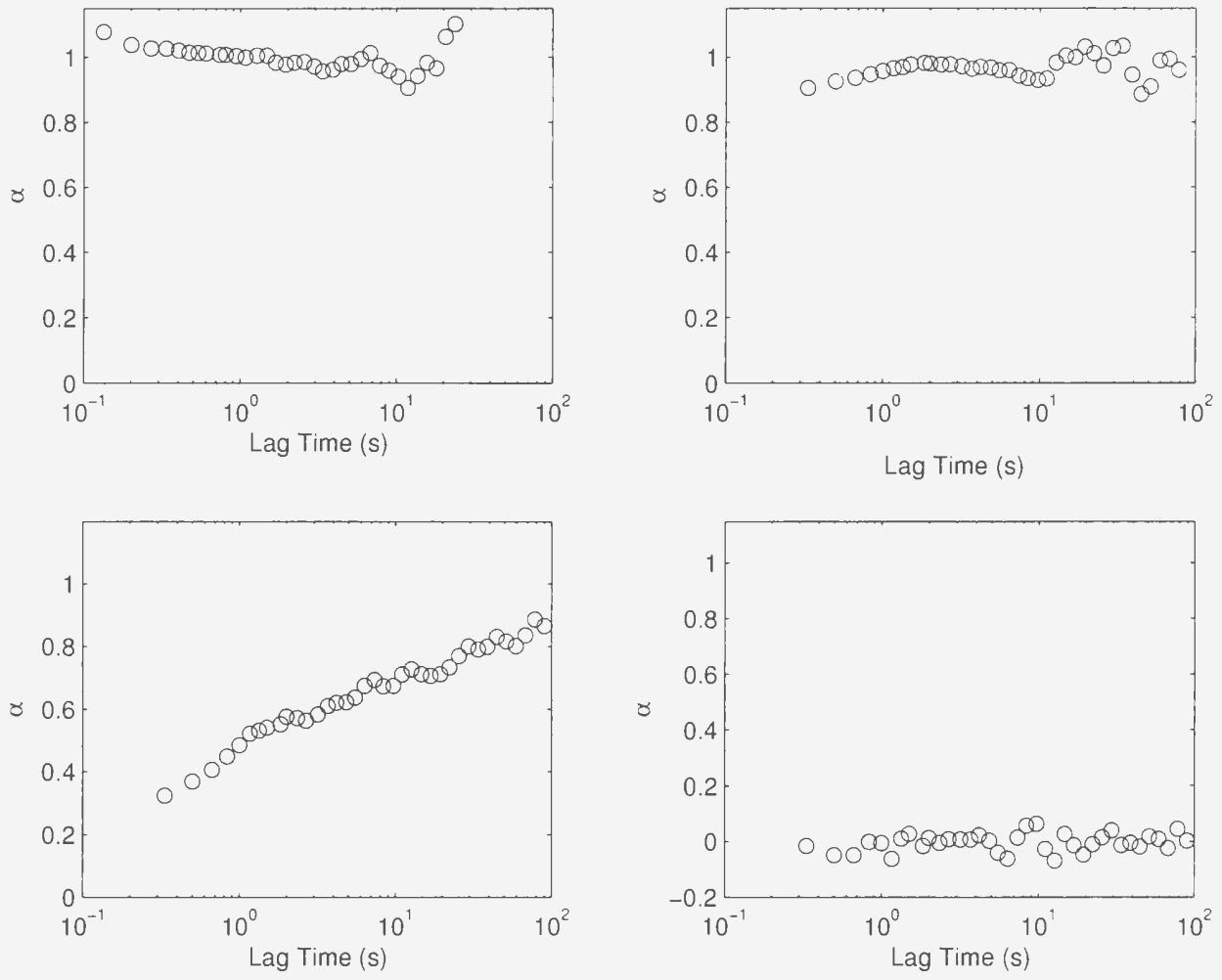

Figure 5.4: The diffusive exponent as a function of age for 1.5% laponite. From left to right, the two top plots are for 0h and 6h and the lower plots are for 9h and 24h respectively.

or length scales of the fluid microstructure. Since only one size of probe particle was used in this set of experiments, we are unable to determine which of the two quantities the MSD plateau measures.

5.2.3 The Diffusive Exponent

Plots of the diffusive exponent vs. lag time for various ages of laponite at a fixed concentration of 1.5% is shown in Fig. 5.4. We observe that at 0 hours, $\alpha(\tau)$ has a value close to 1 at all lag times, indicating diffusive motion at this age. The variations in $\alpha(\tau)$ for lag times greater than about 10 s are likely due to poor statistics, since at this sample age, the high mobility of the spheres means that only a few spheres can stay in focus for that long.

At 6 hours, we observe that $\alpha(\tau) \approx 1$ for $\tau \geq 2$ s, although is slightly lower than 1 for $\tau < 2$ s. At a sample age of 9 hours, $\alpha(\tau)$ increases from about 0.3 at short lag times to 0.8 at long lag times, indicating the spheres are more mobile over longer lag times. This means that with increasing lag time, the motion of the spheres becomes closer to diffusive behaviour. This trend implies that at short lag times, structures in the fluid inhibit the movement of the spheres, but at longer lag times, the effect of the structures on their motion decreases and their mobility increases. As indicated earlier this may be an indication of the sol-gel transition point. At 24 hours, $\alpha(\tau) \approx 0$ at all lag times. This indicates that the spheres are trapped in the gel and do not move appreciably.

5.2.4 The van Hove Correlation Function

The van Hove correlation function for laponite as a function of sample age at lag times of 1 s and 10 s are shown in Figures 5.5 and 5.6 respectively. The distribution of

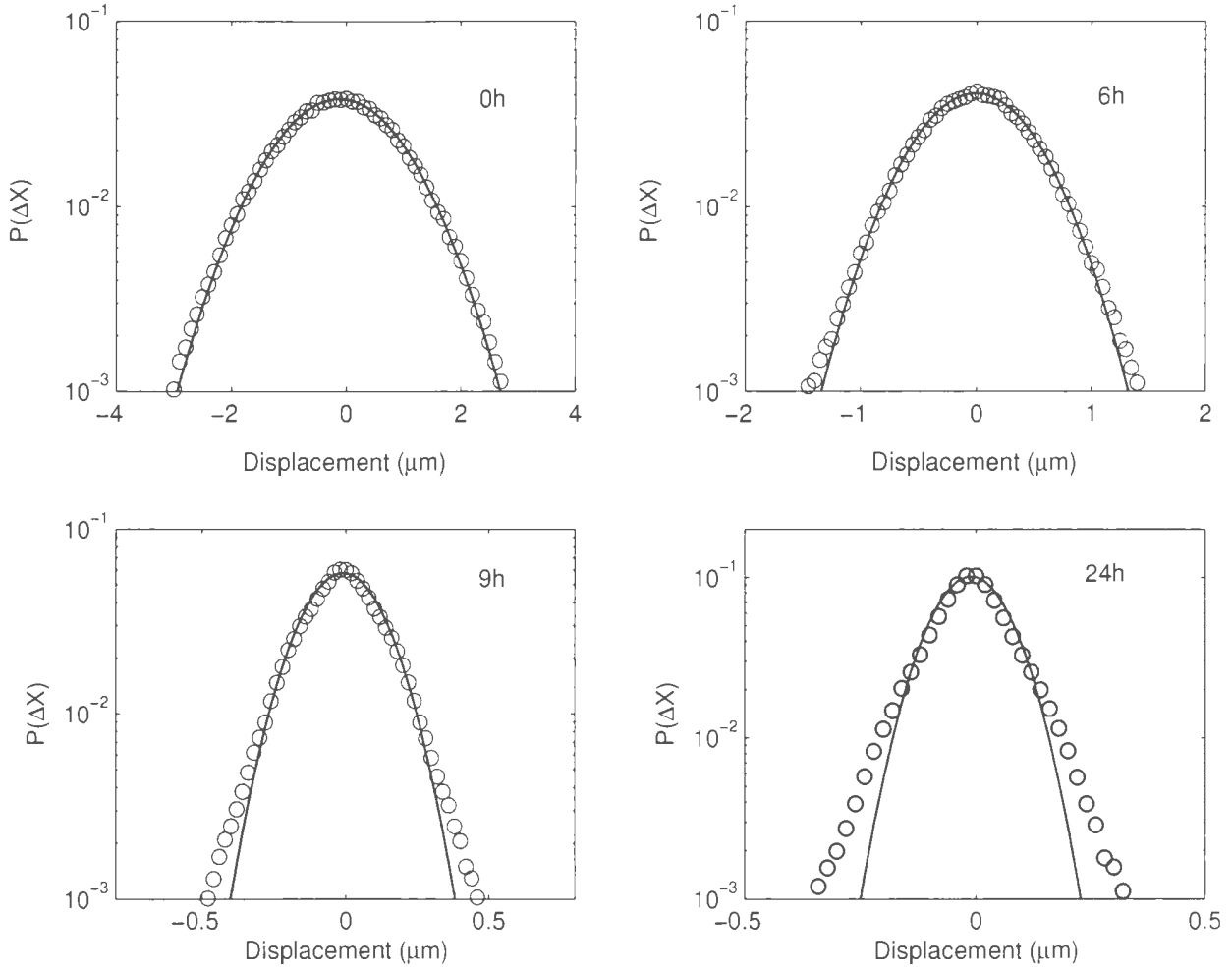

Figure 5.5: The van Hove correlation function for 0.49 μm spheres in different ages of 1.5% laponite. The lag time is 1 s. The solid lines are Gaussian fits to the data.

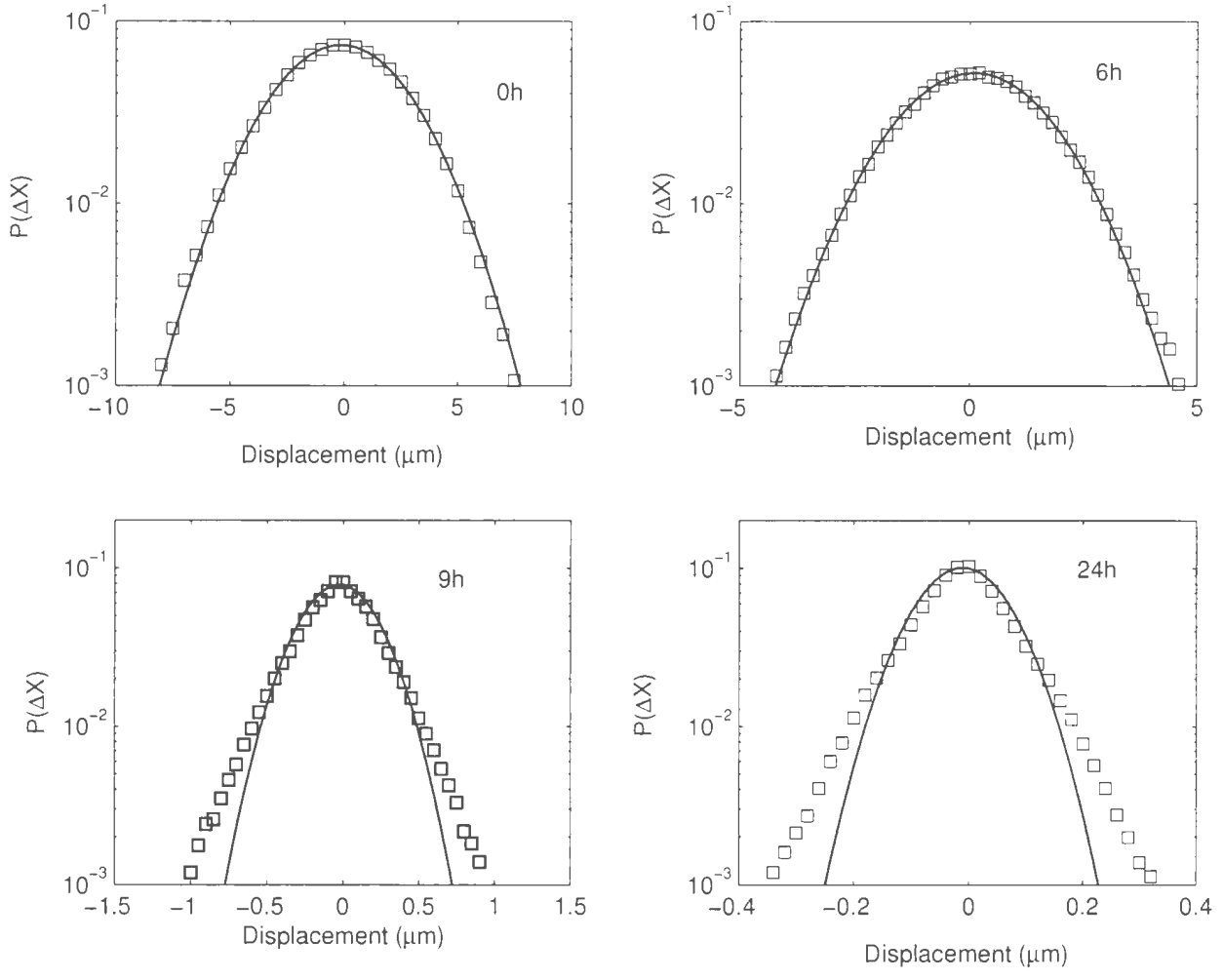

Figure 5.6: The van Hove correlation function for 1.0 μm spheres in different ages of 1.5% laponite. The lag time is 10 s. The solid lines are Gaussian fits to the data.

Laponite Sample	Diffusion Constant ($\mu m^2/s$)
0h	0.5459±0.0050
6h	0.1193±0.0014
9h	0.0095±0.0003
24h	0.0032±0.0002

Table 5.1: Diffusion Constants for the various ages of 1.5% laponite suspensions calculated from the width of the Gaussian fits to the van Hove Correlation Function.

step sizes for 0 and 6 hours are well described by Gaussian fits at both lag times. This implies that at these ages, the fluid environment is homogeneous on the length scale of the particle size. As the colloidal particles interact, they form aggregates which result in structures in the fluid. The fact that the spheres are probing a homogeneous environment at these ages may indicate that the aggregates formed to this point have length scales much smaller than the probe particles. The fact that the distribution is narrower at 6 h than at 0 h indicates that the viscosity of the fluid has increased so the motion of the spheres is reduced. At 9 and 24 hours we observe deviations from Gaussian behaviour. This means that at these ages, the spheres begin to feel the effects of the structures in the fluid. This inhibits their motion, resulting in the non-Gaussian behaviour, and the fluid becomes heterogeneous on the length scale of the particles. As discussed in Chapter 2, the width of the Gaussian distribution can be used to calculate the diffusion coefficient, D. Values of D for the different ages of laponite are shown in Table 5.1. For cases where the distribution deviates from Gaussian behaviour, D is only approximate and it describes the smaller displacements (slower subset of the particles) rather than the whole distribution. The results in

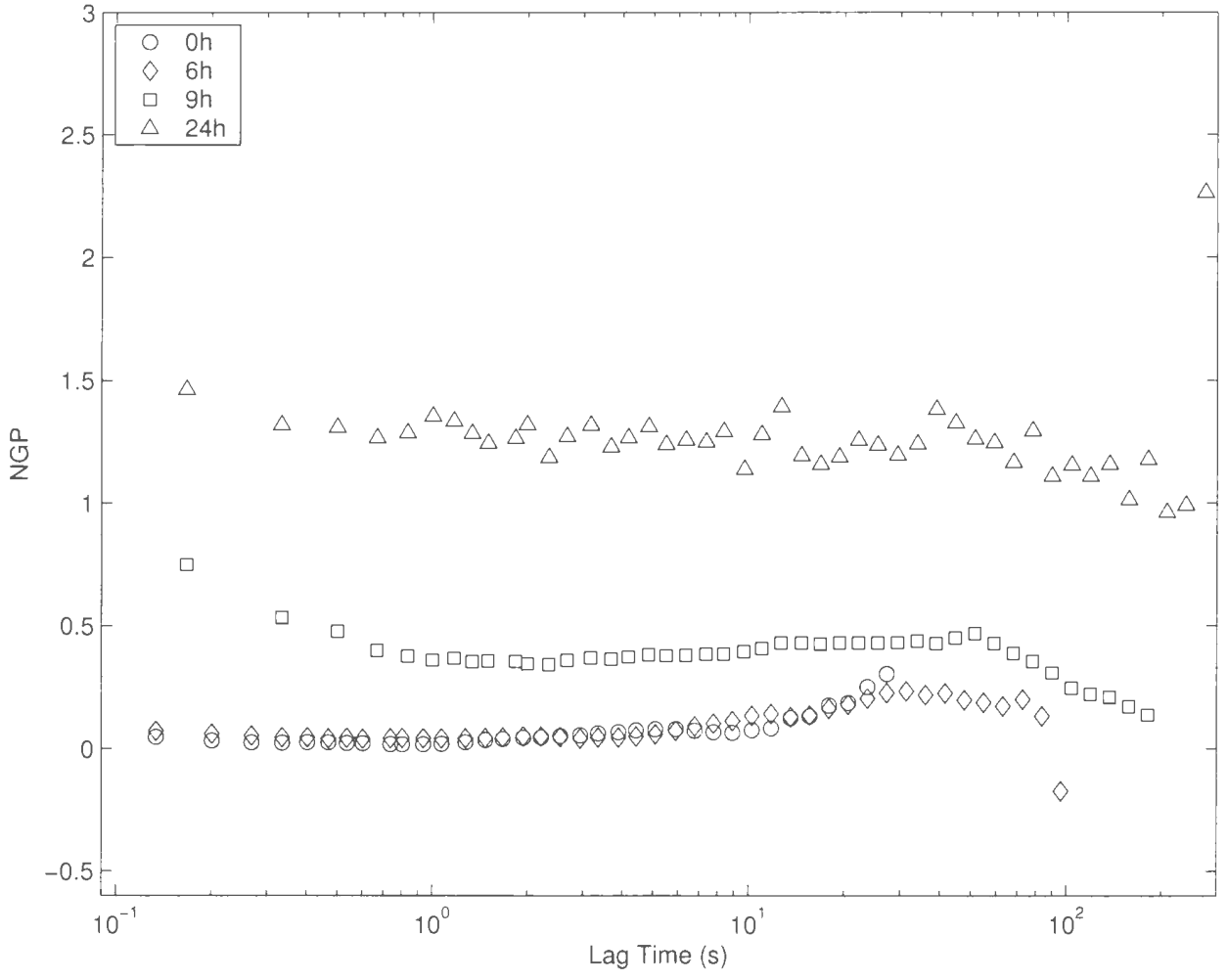

Figure 5.7: The non-Gaussian parameter as a function of age of 1.5% laponite suspensions.

Table 5.1 show that D decreases with increasing sample age. This is in agreement with our observations that with increasing age, the motion of the spheres becomes more and more hindered and confined.

5.2.5 The Non-Gaussian Parameter

The NGP for laponite as a function of sample age is shown in Figure 5.7. At 0 and 6 hours, the NGP is approximately 0 at all lag times suggesting a purely diffusive motion of the probe particles, consistent with the results presented above. As explained above, the upturns in the NGP at lag times beyond 10 s may be due to poor statistics. The 9h NGP decreases with increasing lag time up to about 1 s, then is constant up to $\tau \approx 50$ s. At very long lag times ($\tau > 50$ s), the NGP approaches zero. This means that on long time scales, the particles escape from the structures in the fluid or the structures themselves rearrange, the obstructions to the motion of the particles decrease and the NGP correspondingly decreases. This behaviour is consistent with our earlier suggestion that at this age, the spheres are temporary trapped in structures in the fluid, but escape from them at longer lag times. The fact that the NGP approaches zero at longer lag times indicates the motion becomes almost purely diffusive. At 24 hours, the NGP is non-zero at all lag times. In line with our earlier observations, the particles are almost completely trapped at this age and so the NGP is relatively high on all time scales.

5.2.6 Correlation Analysis

The distribution of x_{12} as a function of r_{01} for different ages of 1.5% laponite suspension is shown in Fig. 5.8 for a lag time of 1 s. The distributions show that there is a large number of data points and hence averaging can be done with good

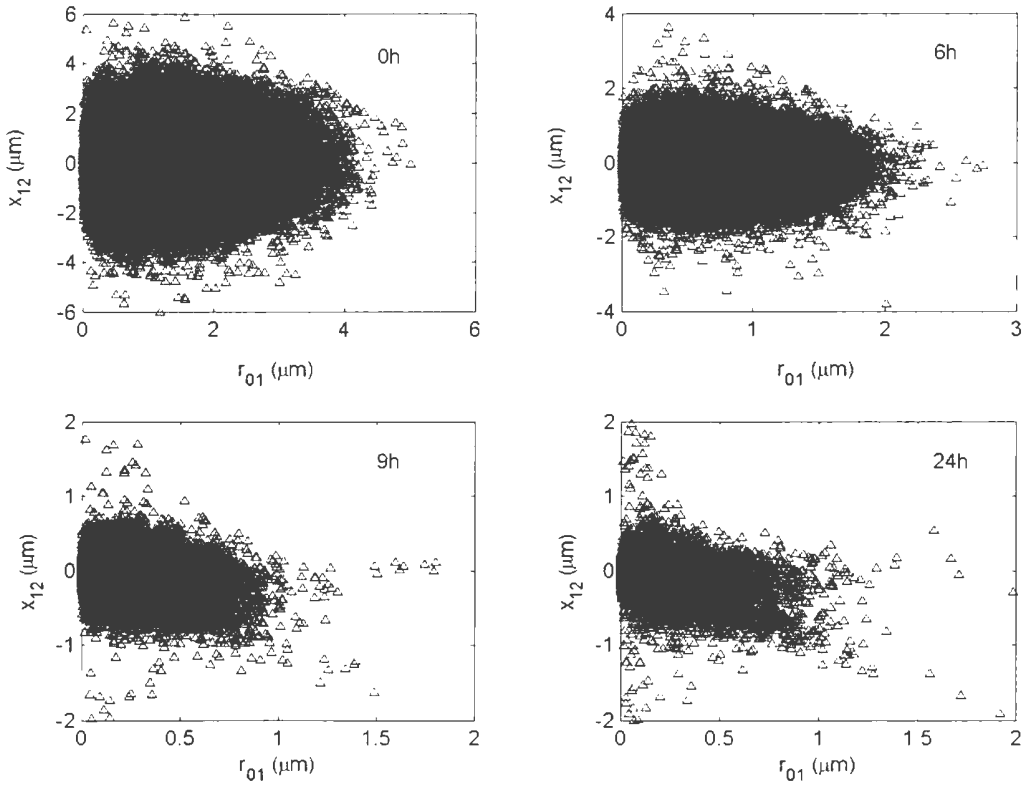

Figure 5.8: The distribution of x_{12} as a function of r_{01} for different ages of 1.5% laponite suspensions. The lag time is 1 s.

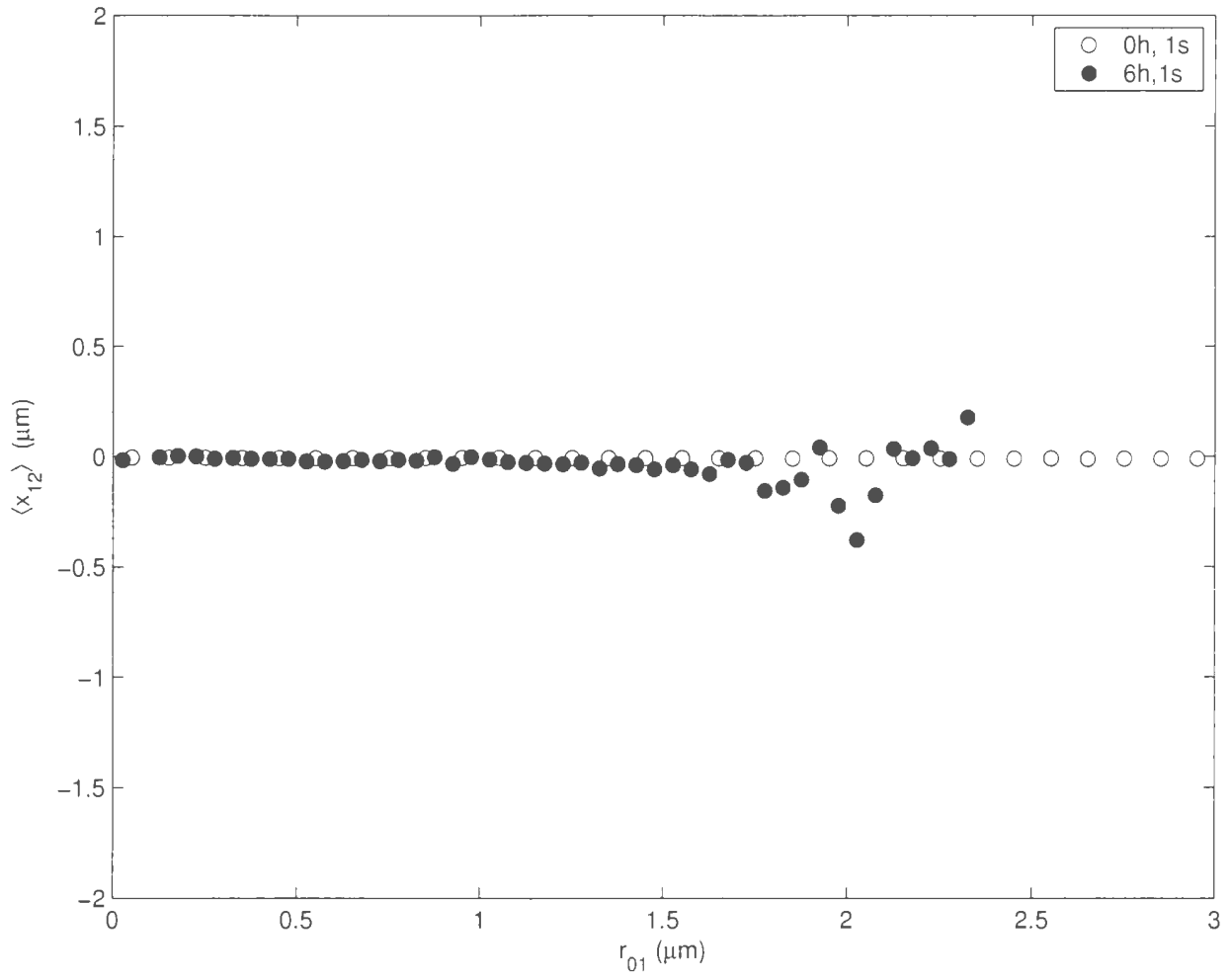

Figure 5.9: The plot of $\langle x_{12} \rangle$ vs r_{01} for the 0h and 6h laponite samples at a lag time of 1 s.

statistics. The distribution is symmetrical at smaller ages due to the random motion of the spheres, but as the sample ages it develops a clear negative slope as the motion of the spheres becomes affected by the structure in the fluid.

Plots of $\langle x_{12} \rangle$ vs r_{01} are shown in Figures 5.9 and 5.10. At small ages, (0 and 6 hours), $\langle x_{12} \rangle \sim 0$. This shows that there is no correlation between the initial and subsequent particle displacements, and that the particles move randomly and freely.

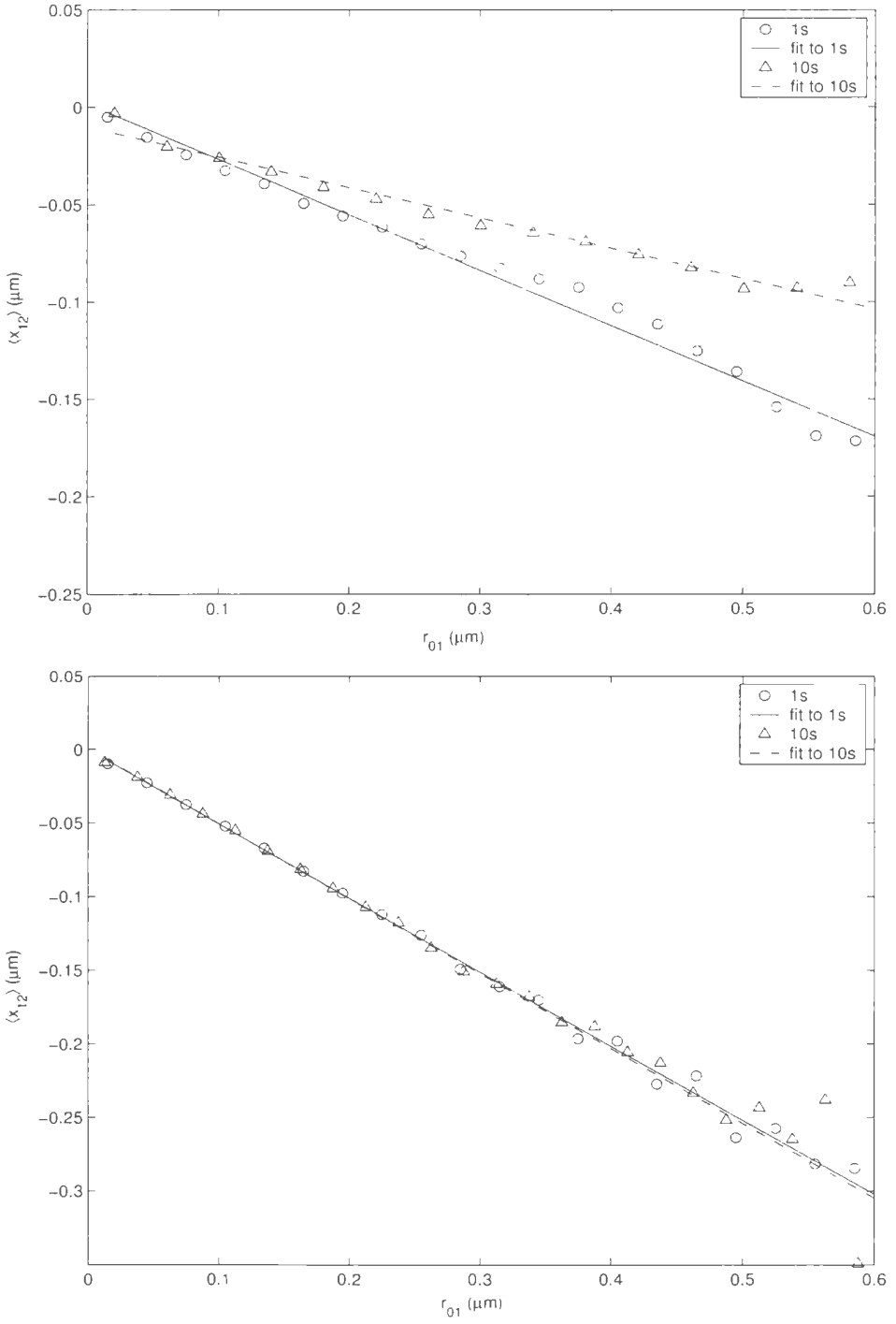

Figure 5.10: The plot of $\langle x_{12} \rangle$ vs r_{01} for 9h and 24h laponite samples. The top plot is for 9h while the bottom plot is for 24h at the lag times shown.

At higher ages, as more aggregates are formed due to the interactions between the colloidal particles, structures form which obstruct the free movement of the spheres, and consequently we see a negative correlation between $\langle x_{12} \rangle$ and r_{01}. In contrast to the results for carbopol presented in Chapter 4, there is no clear deviation from the linear relationship between $\langle x_{12} \rangle$ and r_{01} and so we are unable to estimate a length scale of the structures. It has been reported that unfiltered samples of laponite have a fractal structure [34]. If this is the case, then the structures will not have a specific characteristic length scale. This may be the reason for our inability to determine any length scale with this technique.

5.3 Laponite as a Function of Concentration at Fixed Age

5.3.1 Particle Trajectories

Figures 5.11 and 5.12 show the particle trajectories measured in laponite solutions of different concentrations 48 hours after the samples were prepared. The trajectories for all the particles in the field of view are shown in Figs. 5.11A, 5.11C, 5.12A and 5.12C. These figures show that the trajectories become more localized and the motion of the spheres become more restricted as the concentration of laponite is increased. At 0.3% and 1.0% laponite concentrations, the individual particle trajectories (Figs. 5.11B and 5.11D respectively) show that the particles move randomly. Although particularly at 1% there are certain regions where the particles tend to spend more

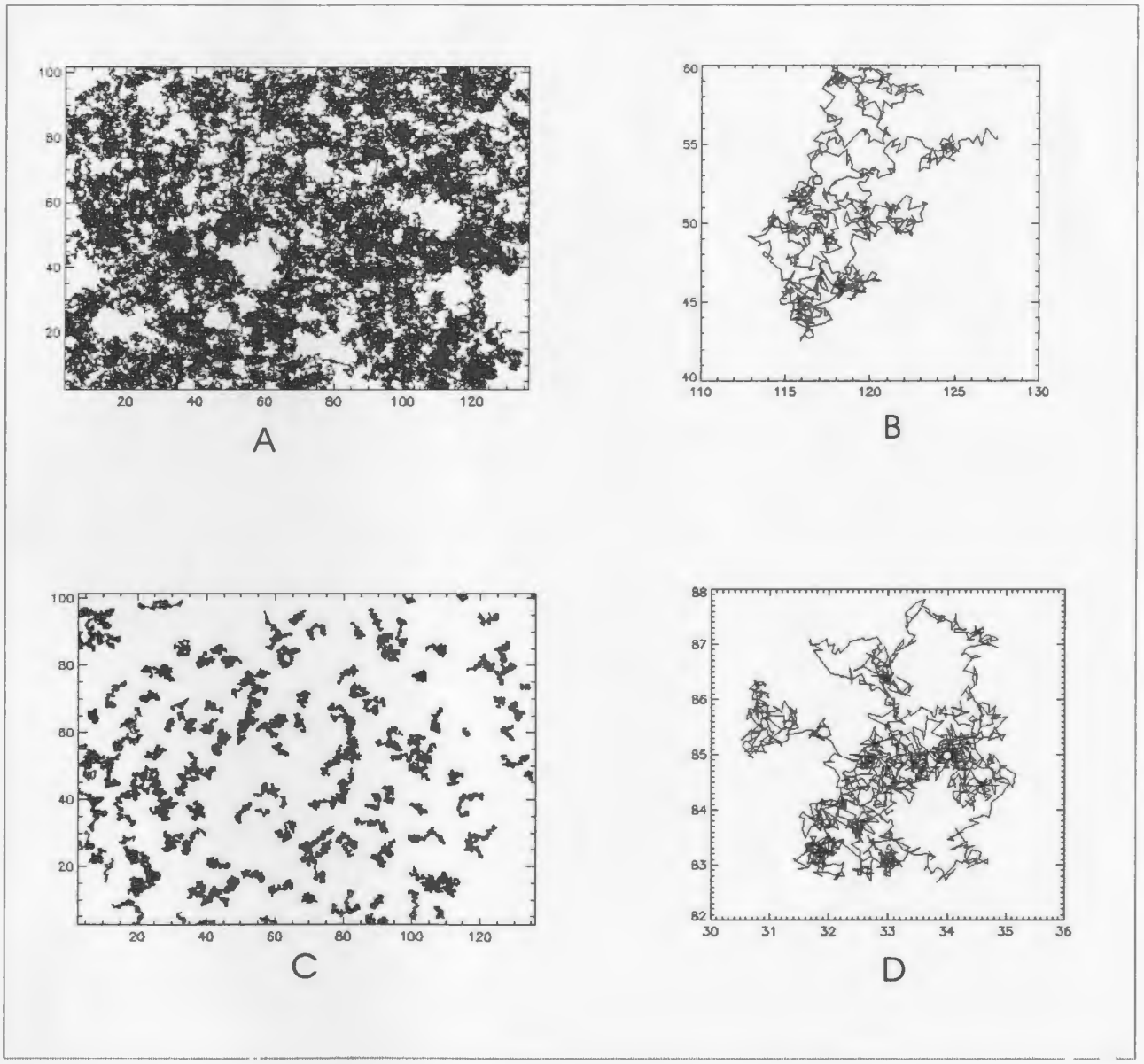

Figure 5.11: Trajectories for 0.49 μm spheres in 0.3% (A and B) and 1.0 % (C and D) laponite suspensions. A and C gives the trajectories for all the spheres in the field of view while B and D are typical trajectories for single spheres. All the axis are in μm. The age of the samples is 48 hours.

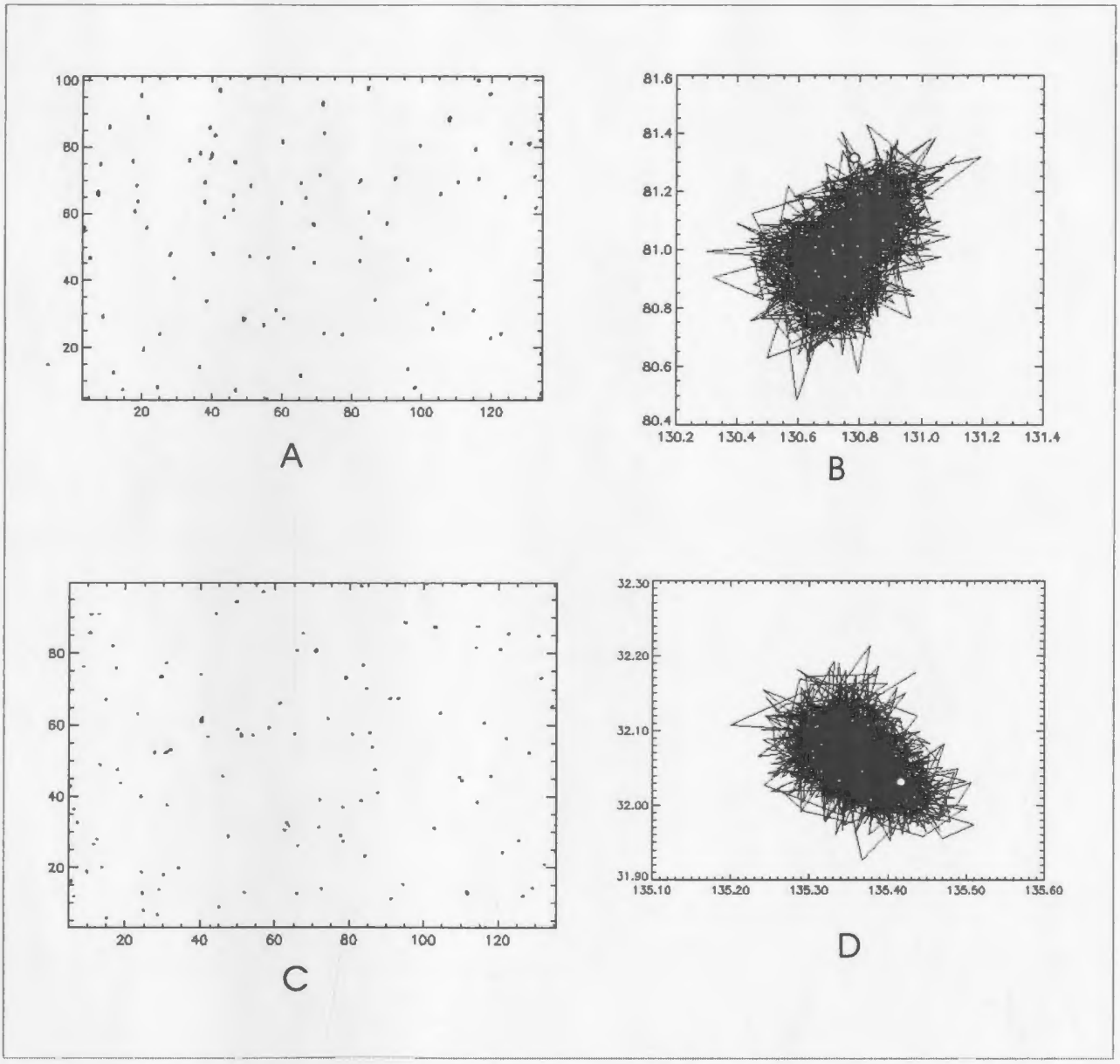

Figure 5.12: Trajectories for 0.49 μm spheres in 1.5% (A and B) and 2.5% (C and D) laponite suspensions. A and C gives the trajectories for all the spheres in the field of view while B and D are typical trajectories for single spheres. All the axis are in μm. The age of the samples is 48 hours.

time, the trajectories do not show any long term trapping. At these concentrations the increased concentration of laponite particles reduces the motion of the spheres, but they are still able to move about randomly. For the 1.5% and 2.5% concentrations, in contrast, the individual trajectories (Figs. 5.12B and 5.12D) span only 0.5 and 0.2 μm on the x axis respectively, indicating that the spheres are trapped and unable to diffuse freely. At 1.5%, the length scale of the trajectory is comparable to the sphere size, indicating that though the spheres may be trapped, they are able to jiggle about slightly. At 2.5%, the spheres are constrained to the point that they are almost immobile. At these concentrations, the interactions between the colloidal particles are strong enough that the suspension gels, leading to a highly reduced sphere mobility compared to the lower concentrations.

5.3.2 The Mean Square Displacement (MSD)

Figure 5.13 shows the ensemble average MSD as a function of laponite concentration at a fixed age of 48 hours. The MSD decreases with increasing concentration, showing that the motion of the spheres is reduced as the concentration of the colloidal particles is increased. Increasing the concentration of the colloidal particles leads to a higher degree of interaction between the particles which eventually leads to the formation of a gel. At a concentration of 1.0%, the slope of the MSD is lower for lag times less than about 1 s, but steeper for longer lag times. This behaviour is similar to what was observed in the 9h data in Figure 5.3, and may again signal the start of

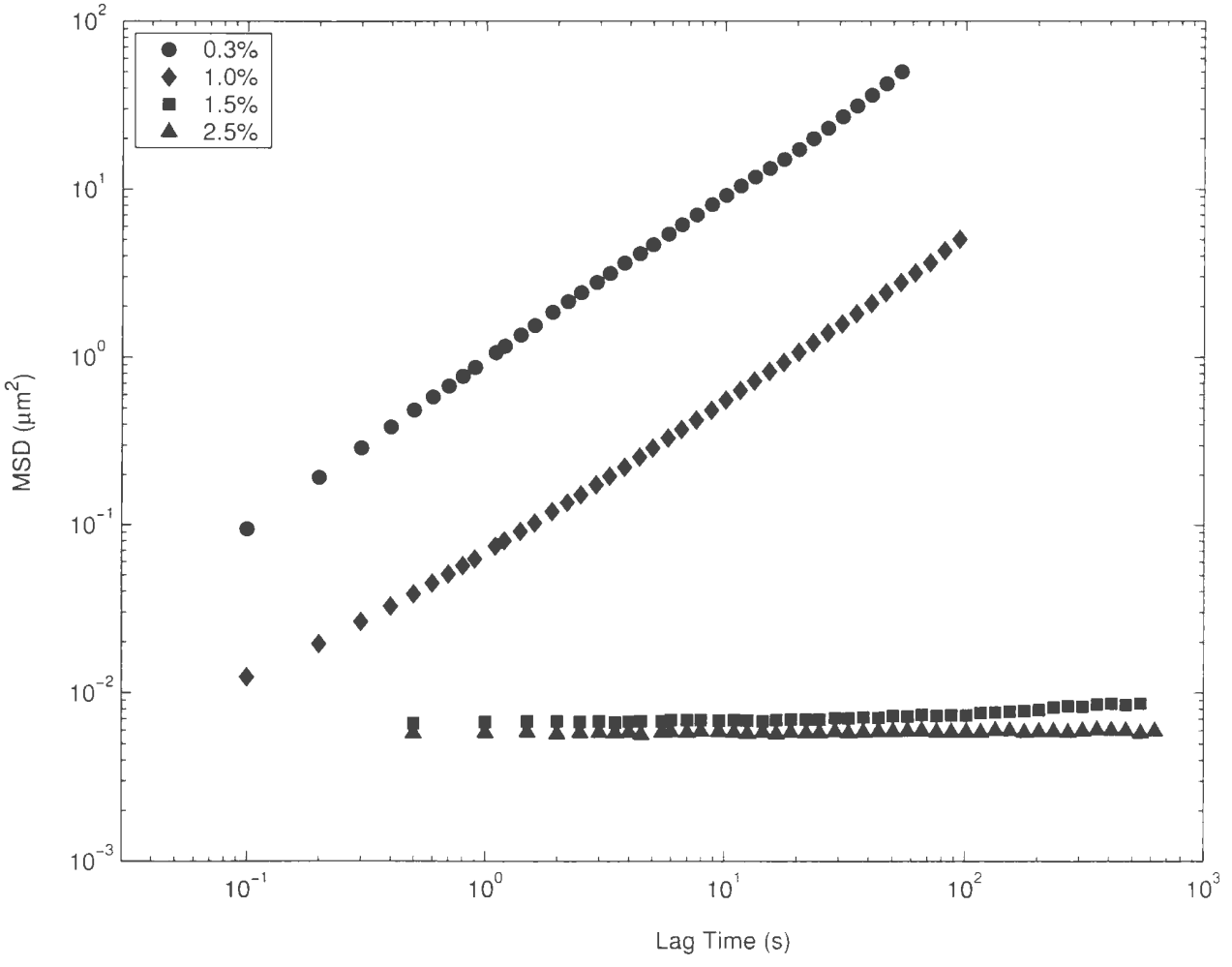

Figure 5.13: The ensemble averaged MSD as a function of laponite concentration at a fixed age of 48 hours.

sol-gel transition. At higher concentrations (1.5% and 2.5%) the MSD is very much reduced, indicating the formation of a stronger gel which restricts the motion of the tracer spheres. The MSD for the 1.5% concentration increases slightly at longer lag times (about 100 s) indicating the spheres are able to move slightly on this time scale. The MSD at 2.5% concentration is flat at all lag times indicating complete trapping of the spheres.

The plateaus in the MSD at higher sample ages may be a measure of either local elasticity or pore size, but because we used only one size of the probe particle in this set of experiments, we are unable to determine which of the two quantities it measures.

5.3.3 The Diffusive Exponent

Plots of the diffusive exponent vs. lag time for various concentrations of laponite are shown in Fig. 5.14. All the samples were allowed to age for 48 hours before measurements were made. At 0.3% concentration, $\alpha(\tau)$ has a value close to 1 at all lag times, indicating diffusive motion at this concentration. As observed previously, the variation in $\alpha(\tau)$ around $\tau = 10$ s is likely due to poor statistics, since only a few particles stay in view for this long due to their high mobility at this concentration.

For the 1.0% concentration, $\alpha(\tau)$ increases from about 0.6 to about 1.0, indicating that with increasing lag time, the motion of the spheres changes from subdiffusive to diffusive. At short lag times, structures in the fluid inhibit the movement of the

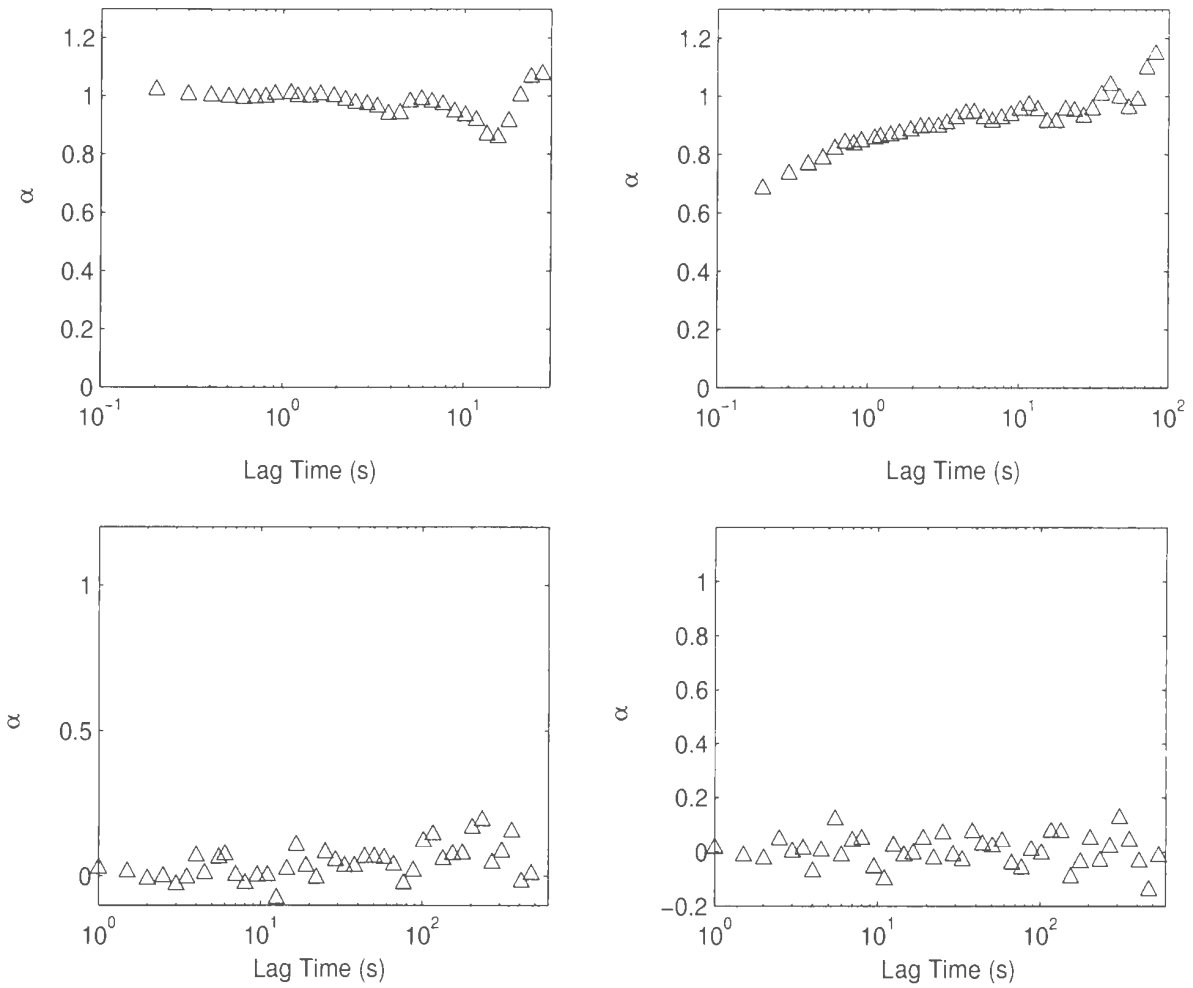

Figure 5.14: The diffusive exponent as a function of laponite concentration at a fixed sample age of 48 hours. From left to right, the two top plots are for 0.3% and 1.0% and the lower plots are for 1.5% and 2.5% respectively.

spheres, but at longer lag times, the spheres are able to move more freely as they escape from the constraining structures. This increase in α may also be due to rearrangements of the structure itself on this time scale [17]. A similar transition from subdiffusive to diffusive behaviour has been observed by Weeks et al. in other colloidal systems [17]. As indicated earlier this may be an indication of the sol-gel transition. At 1.5 and 2.5% concentrations, $\alpha(\tau) \sim 0$ at all lag times. This indicates the spheres are trapped.

As the concentration of the colloidal particles is increased, interactions between them also increase. This results in the formation of a gel beyond some threshold concentration. From our results, developing fluid structure begins to affect the motion of the spheres at a concentration of 1.0%, and a stiff gel forms at 1.5%.

5.3.4 The van Hove Correlation Function

Figures 5.15 and 5.16 show the distributions of the particle displacements as a function of laponite concentration for lag times of 1 s and 10 s respectively. We observe that at 0.3% and 1.0%, for both lag times, the distribution is well described by a Gaussian, indicating a homogeneous environment on the length scale of the particles. Any structures in the fluid are not large enough to restrict the motion of the spheres to any greater extent. At 1.5% and 2.5%, the increased concentration of the colloidal particles results in a greater degree of interaction between them, leading to the formation of stiff gels. The width of the distributions decreases with increas-

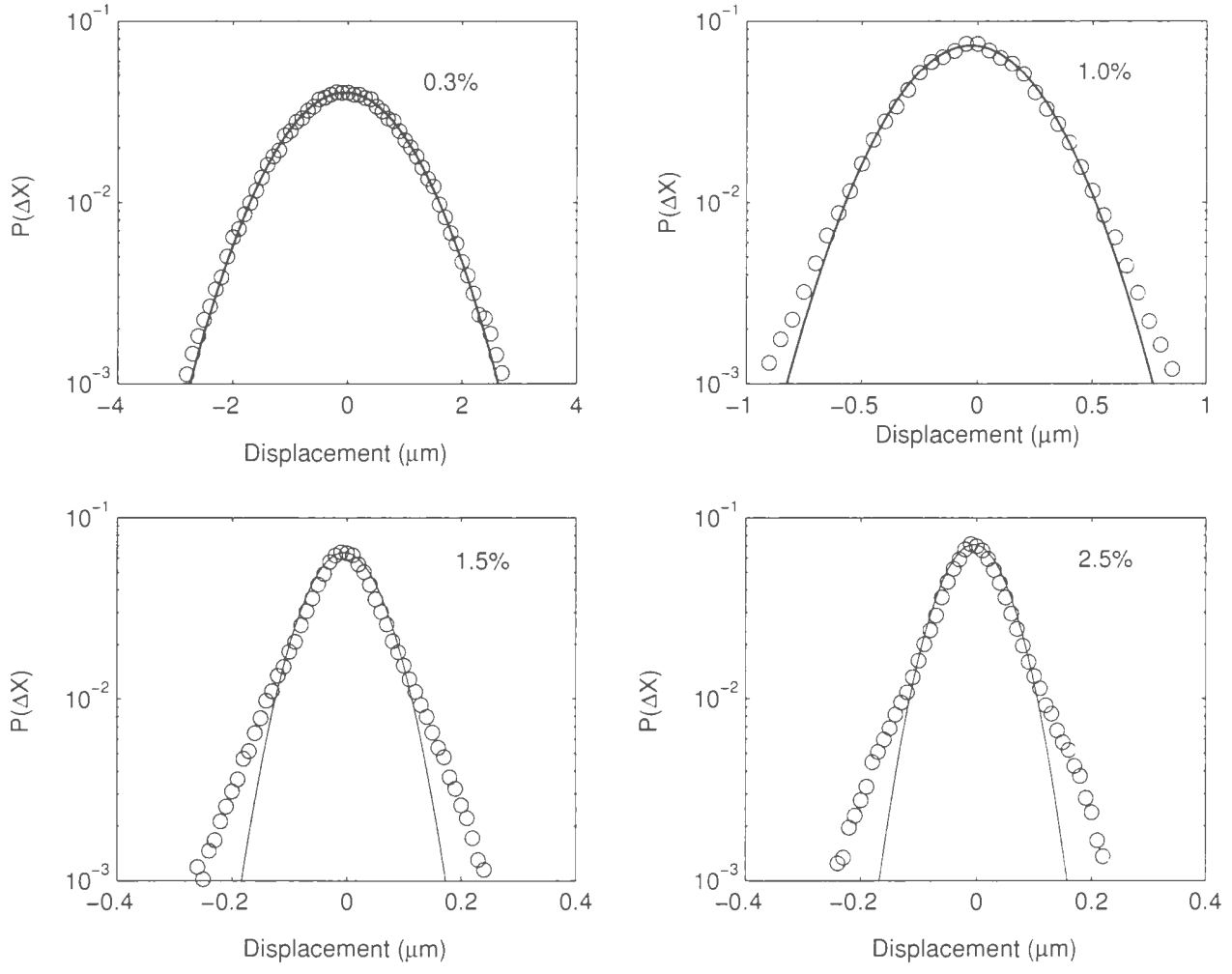

Figure 5.15: The van Hove correlation function for different concentrations of laponite. The lag time is 1 s. The solid lines are Gaussian fits to the data.

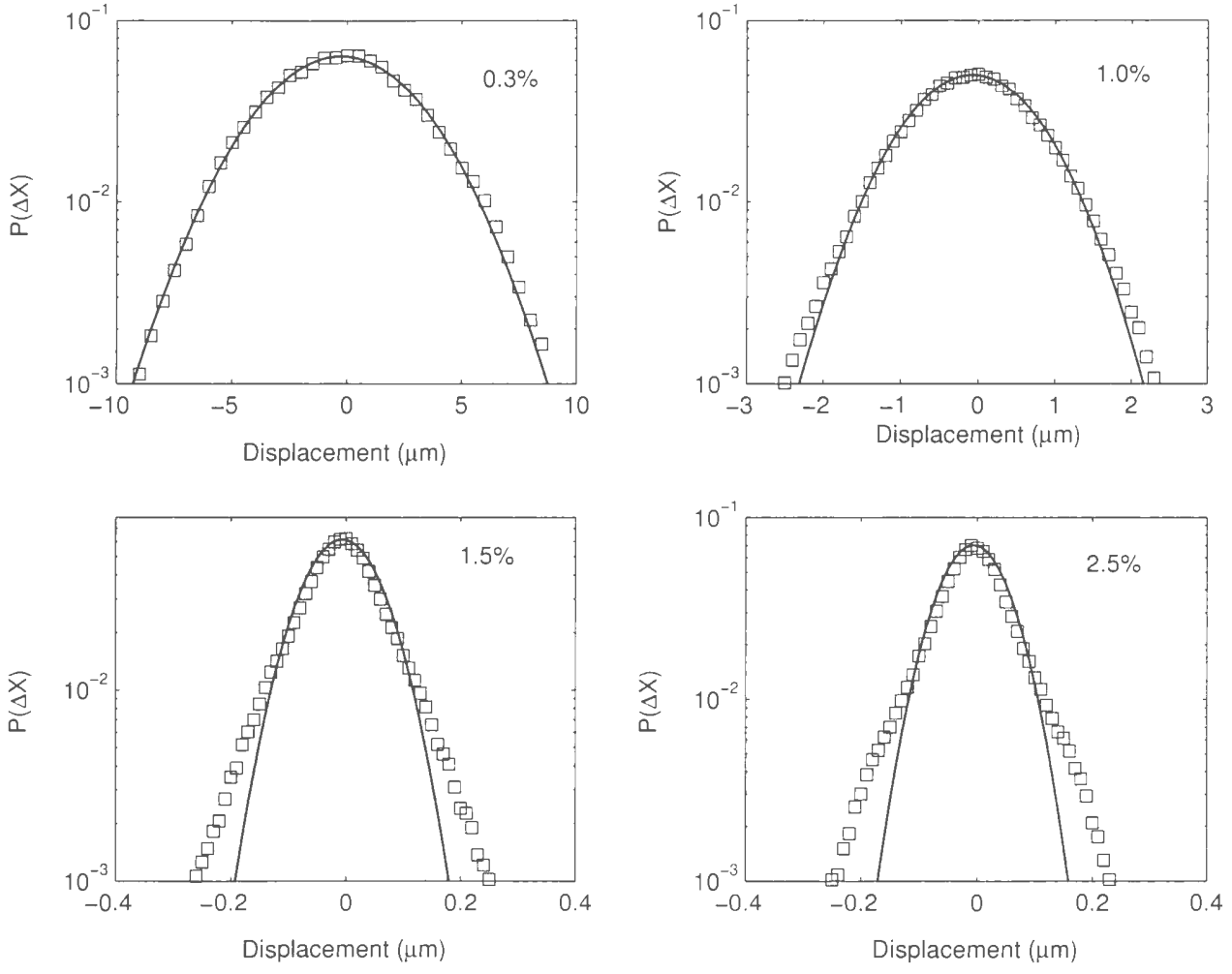

Figure 5.16: The van Hove correlation function for different concentrations of laponite. The lag time is 10 s. The solid lines are Gaussian fits to the data.

Laponite Sample	Diffusion Constant ($\mu m^2/s$)
0.3%	0.4894 ± 0.0050
1.0%	0.0368 ± 0.0007
1.5%	0.0020 ± 0.0001
2.5%	0.0016 ± 0.0001

Table 5.2: Diffusion coefficients for the 0.49 μm spheres in different concentrations of laponite calculated from the width of the Gaussian fits to the van Hove Correlation Function.

ing concentration implying that the viscosity of the fluid increases with increasing concentration.

The diffusion constants for the spheres in the different concentrations of laponite are shown in Table 5.2. These results show that D decreases with increasing concentration, as expected.

5.3.5 The Non-Gaussian Parameter

Figure 5.17 shows the plot of the non-Gaussian parameter (NGP) vs. lag time for the various concentrations of laponite at a fixed age of 48 hours. At 0.3%, we see that the NGP is zero for all lag times up to $\tau \sim 20$ s and therefore we infer that at this concentration, the particles diffuse freely without any hindrance from the suspended colloidal particles. The downturn in the NGP at longer times is due to poor statistics, as the particles move fast enough that only a few stay in view for $\tau > 20$ s. The NGP for the 1.0% concentration decreases rapidly for small lag times ($\tau < 1$ s) and is close to 0 thereafter. The initial decrease in the NGP suggests that there is some small scale structure that affects the motion at short time scales, but

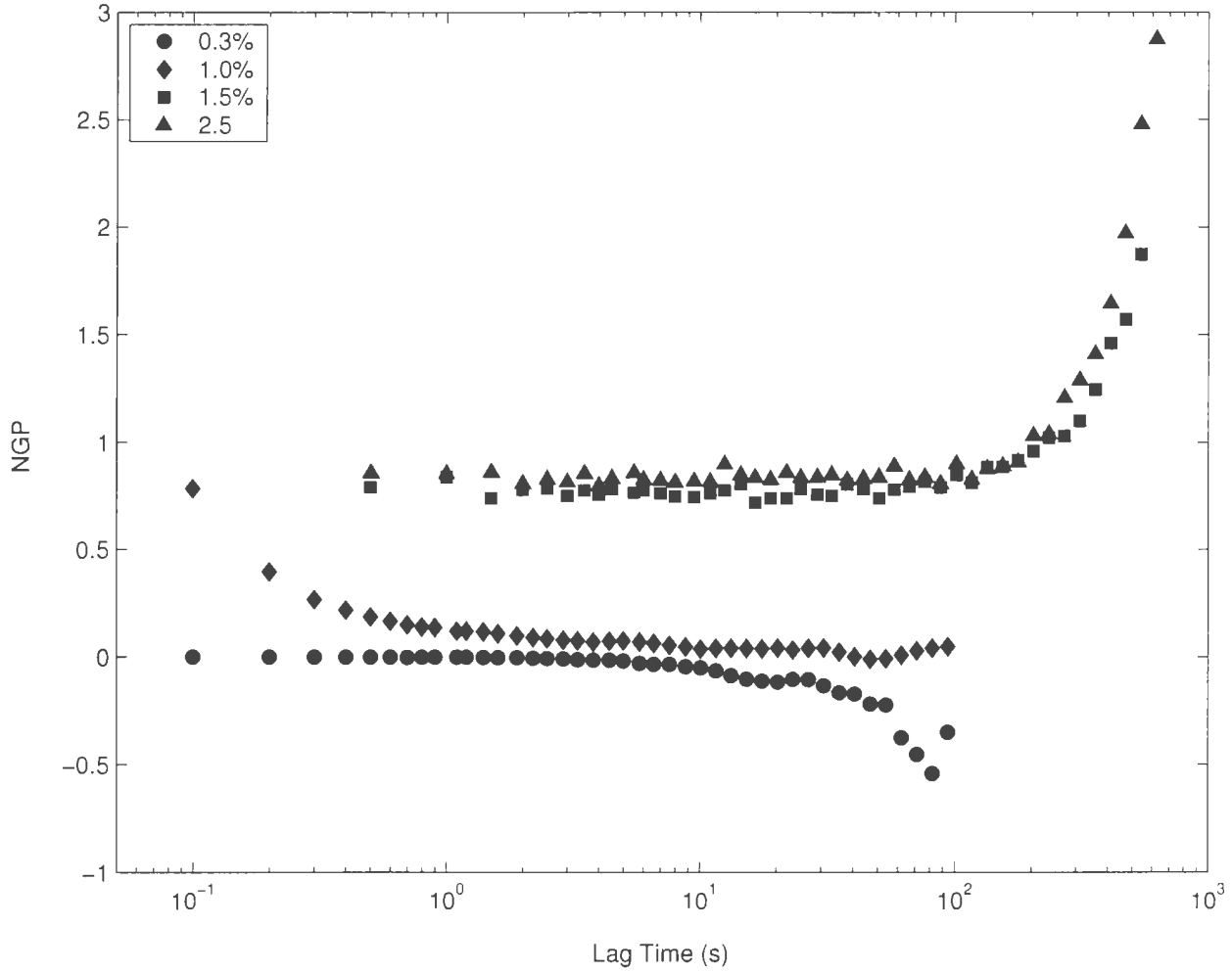

Figure 5.17: The non-Gaussian parameter as a function of laponite concentration.

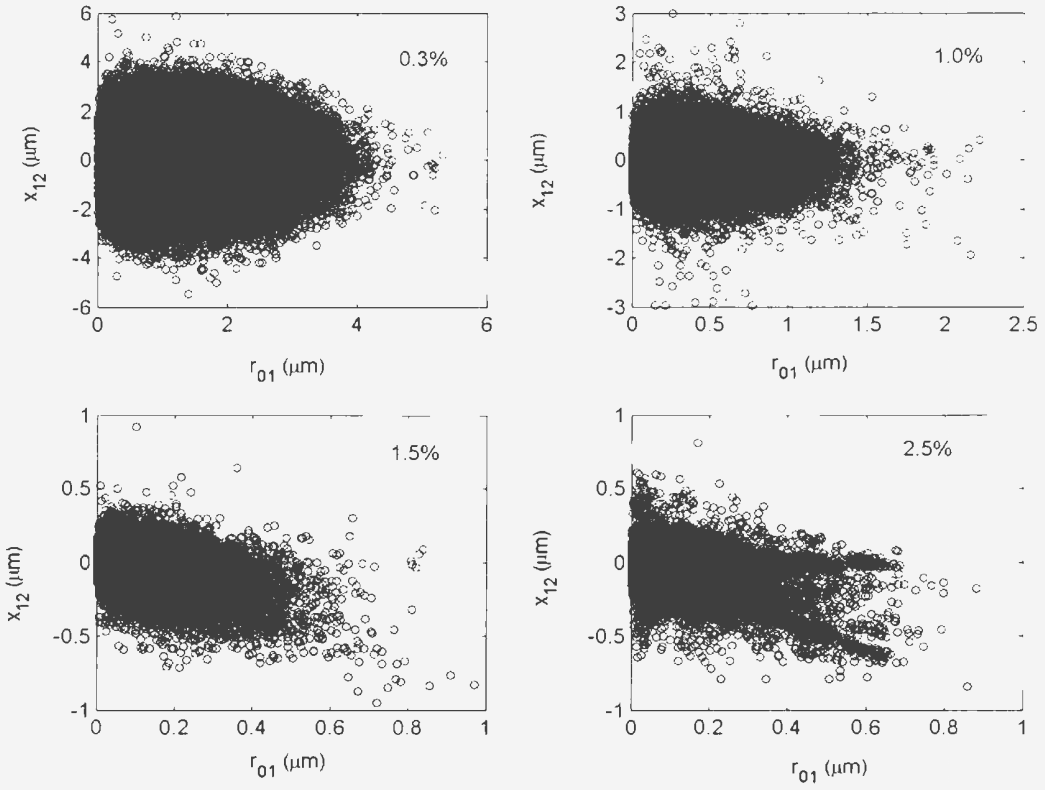

Figure 5.18: The distribution of x_{12} as a function of r_{01} for different concentrations of laponite. The lag time is 1 s.

that these are not significant over time scales greater than 1 s. However the fact that the NGP is not exactly zero means that though they may be moving freely, the probe particles still feel the effect of the fluid. The NGP values are highest for the higher concentrations (1.5% and 2.5%) as the spheres are confined by the fluid structures. Beyond $\tau \approx 300$ s, the NGP increases rapidly as the probe particles feel the effect of the fluid structures more strongly.

5.3.6 Correlation Analysis

The distribution of x_{12} as a function of r_{01} for the different concentrations of laponite at fixed sample age is shown in Figure 5.18. The lag time is 1 s. The distributions show that there is a large number of data points and hence averaging can be done with good statistics. The distribution is symmetrical at low concentrations, due to the random motion of the spheres, but becomes distorted with negative slope at higher concentration as the motion of the spheres become less random. Figures 5.19 and 5.20 show $\langle x_{12} \rangle$ vs r_{01} for various concentrations of laponite at the specified lag times. At 0.3%, $\langle x_{12} \rangle \sim 0$ for all r_{01}, showing that the motion of the spheres is random and the second displacement is not correlated with the first. At higher concentrations, however, we see a negative correlation between $\langle x_{12} \rangle$ and r_{01}, indicating that the spheres will on average move in the opposite direction relative to the initial displacement. This is consistent with the above observations that the structures begin to inhibit the free movement of the spheres. There is however no obvious deviation from the linear relationship between $\langle x_{12} \rangle$ and r_{01} and consequently the length-scales of the structures cannot be estimated from this analysis. If indeed the structures are fractals, then there is no characteristic length scale, which may explain this behaviour.

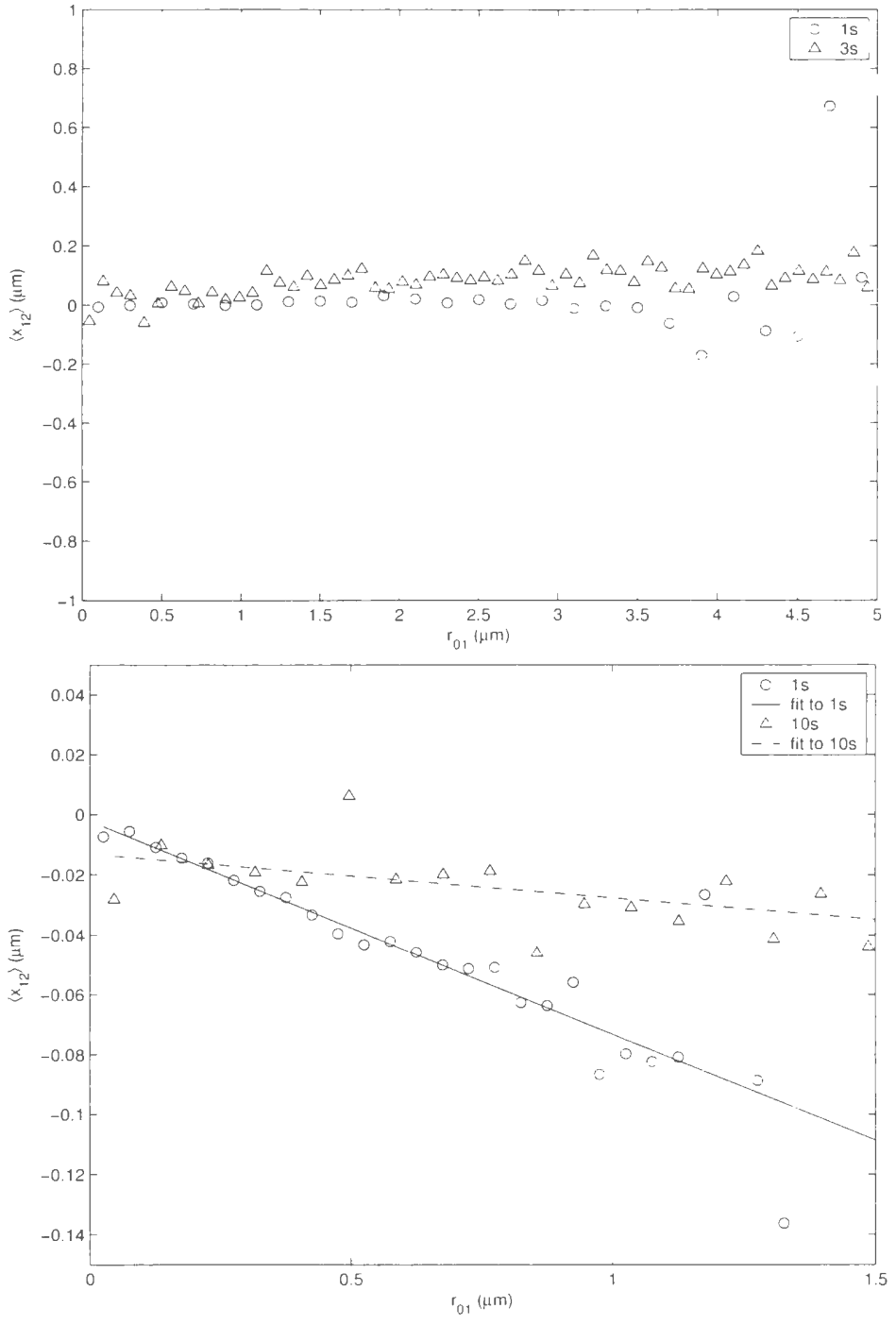

Figure 5.19: The plot of $\langle x_{12} \rangle$ vs r_{01} for 0.3% and 1.0% laponite suspensions. The top plot is for 0.3% while the bottom plot is for 1.0% at the lag times shown.

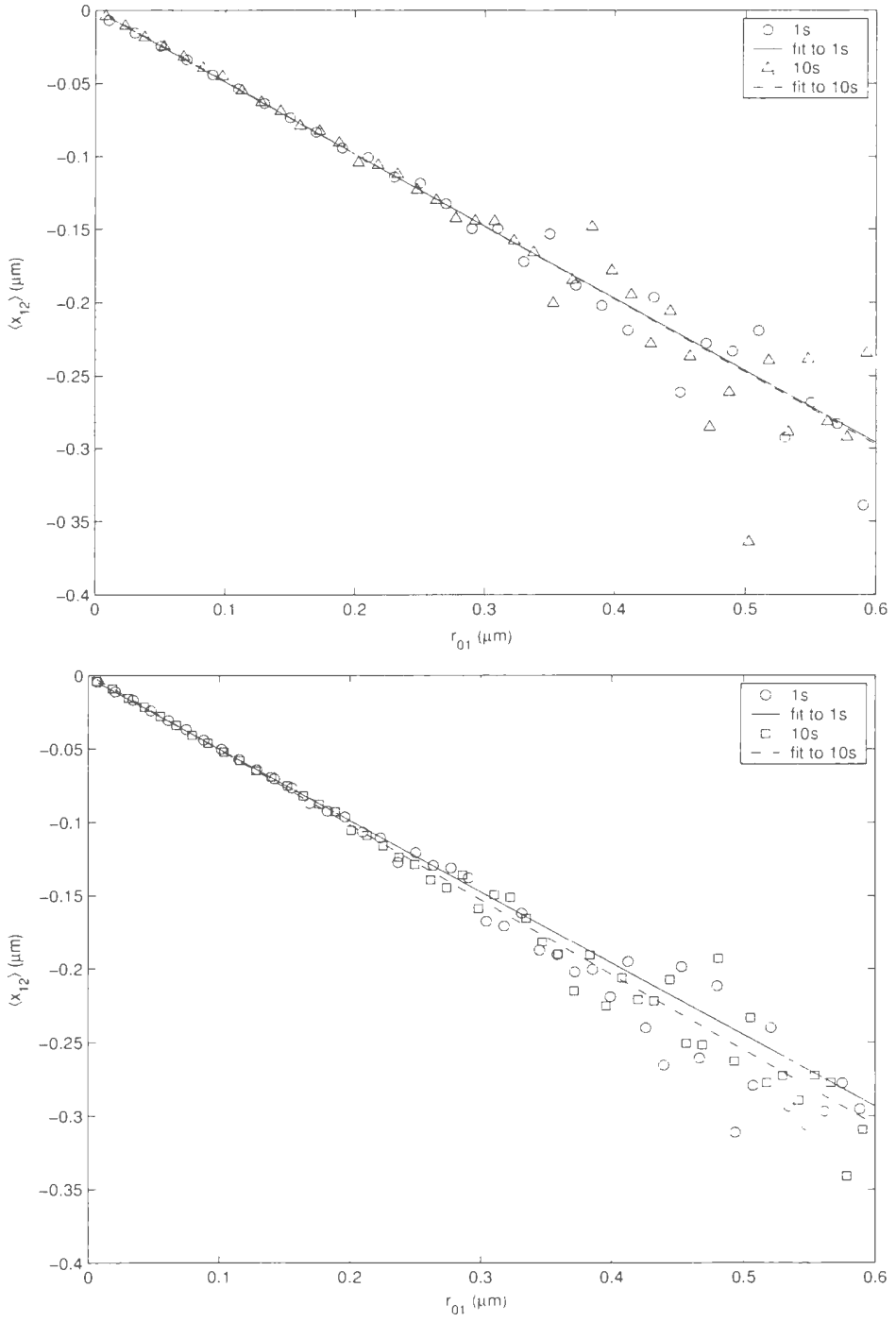

Figure 5.20: The plot of $\langle x_{12} \rangle$ vs r_{01} for 1.5% and 2.5% laponite suspensions. The top plot is for 1.5% while the bottom plot is for 2.5% at the lag times shown.

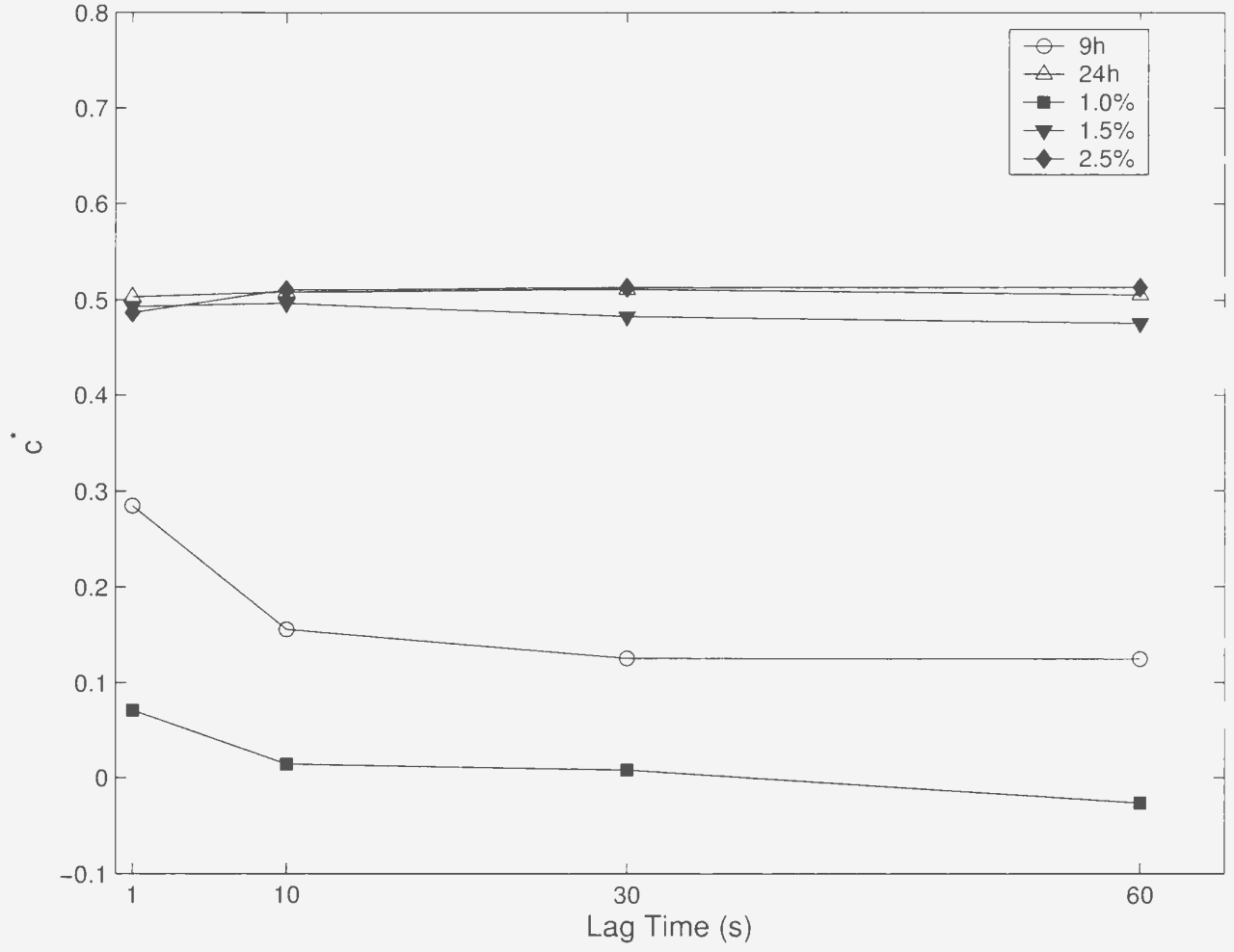

Figure 5.21: The pore strength (opposition to sphere motion) as a function of lag time for various samples of laponite as indicated.

5.4 The Pore Strength (c^*) as a Function of Lag Time

To investigate the degree to which structures in the fluid affect the motion of the spheres, we show in Figure 5.21 how c^* evolves with lag time. c^* quantifies the degree to which the structures in the fluid oppose or inhibit the motion of the spheres and is the absolute value of the slope of the plots of $\langle x_{12} \rangle$ against r_{01} discussed in the previous section. We chose the various ages (9h and 24h at a concentration of 1.5%)

and concentrations (1.0%, 1.5%, 2.5% at a time of 18h) because these are the data for which the motion of the spheres is most restricted. For the 9h and the 1.0% data . c^* decreases with increasing lag time. This means the spheres move more freely at longer lag times as the degree to which the structures oppose its motion decreases. It is for these samples that we observe an increase in the diffusive exponent with lag time as shown in Figs. 5.4 and 5.14. At 24h, 1.5% and 2.5%, where laponite forms a gel, c^* has values in the range 0.48-0.51 and remains fairly constant with lag time. This shows that the laponite gels formed under these conditions are thick enough such that their effect on the spheres is independent of lag time as the particles are completely trapped by the gel.

Chapter 6

Summary and Conclusion

6.1 Introduction

In this work, we have used multiple particle tracking to investigate the microstructure of two types of yield-stress fluids, laponite and carbopol. Both materials form a gel in water at sufficient concentration.

The positions of fluorescent microspheres suspended in the fluids were measured with fluorescence video microscopy. The particles were tracked over a period of time and the trajectories analyzed to extract information about the microscopic properties of the fluid. The ensemble-averaged mean square displacement (MSD) was calculated as a function of lag time. From the nature of the MSD, the motion of the spheres can be classified as diffusive, subdiffusive or confined, and a long lag-time plateau in the MSD gives an estimate of the length scale of the structure in the fluids. The distribution of particle displacements was useful in determining whether the fluids were homogeneous or heterogeneous on the length scale of the particles. Deviations from a

Gaussian distribution signaled a heterogeneous environment, which we quantified by calculating the non-Gaussian parameter (NGP). From an analysis of the correlation between successive particle displacements, we were able to further quantify the effect of the fluid structure on motion of the spheres and the length scale of the structures.

We present below a summary of our results and conclusions for the two fluids studied. This is followed by a suggestion for future work in this area.

6.2 Carbopol

We studied carbopol as a function of concentration using 0.49 and 1.0 μm probe particles.

The particle trajectories in low concentrations of carbopol suggest that the spheres move freely. At intermediate concentrations, we observed that the trajectories were localized in certain regions more than others, indicating a trapping effect due to structure in the fluid. At high concentrations and especially for the bigger spheres, the trajectories were highly compact, signifying complete trapping of the spheres by the stiff gel structure. We observed a linear increase of the MSD with lag time at the lowest concentration (0.01% carbopol by weight) for both sphere sizes, showing that at this concentration, the spheres undergo normal diffusion with no obstruction. At intermediate concentrations, the MSD becomes non-linear in lag time, with a logarithmic slope less than one, indicating that the motion of the spheres becomes subdiffusive as the carbopol structures restricts their motion more strongly. At high

concentrations, the MSD is further reduced, indicating a more restricted motion of the spheres. The MSD for the 0.49 μm spheres reaches a plateau at long lag times whereas that of the 1.0 μm spheres is essentially constant at all times. This means the bigger spheres are more strongly confined by the fluid structure than the smaller spheres. At 0.01% concentration, the distribution of particle displacements is well described by Gaussian, but we see deviations from the Gaussian distribution at high concentrations. The NGP is close to 0 for low concentrations, but increases with lag time at higher concentrations, as the spheres feel the effect of the structures more. The correlation analysis we performed showed that there is no correlation between successive particle displacements at low concentrations, but there is a negative correlation between the displacements at high concentrations due to the influence of the fluid structures.

From our results, we conclude that at low concentrations (0.01% by weight) the fluid is homogeneous and Newtonian on the length scale of the probe particles. At high concentrations, the fluid is heterogeneous on the length scale of our measurements due to the formation of pores as the fluid gels. From our estimates, the pore size is of the order of 1-2 microns and decreases with increasing concentration. Since we cannot measure pore sizes smaller than our probe particles, our estimates at high concentrations are biased by the particle size.

6.3 Laponite

Laponite was studied as a function of age at fixed concentration and as a function of concentration at fixed age using one probe particle size (0.49μm). We observed that the change in behaviour of laponite with increasing age and concentration were very similar.

At small sample age and low concentrations, the particle trajectories are random, but the diffusion constant decreases with both increasing sample age and increasing concentration. Trapping by developing structures in the fluid sets in at intermediate ages and concentrations as indicated by the localization of the trajectories in certain regions. At high ages and concentrations, we observe highly compact trajectories showing that the spheres become trapped as stiffer gels are formed. The MSD at small sample ages and low concentrations is linear in lag time indicating diffusive motion. For the intermediate samples, the logarithmic slope of the MSD is less than one for short lag times but approaches a value of one at longer lag times, showing a transition from subdiffusive to near diffusive behaviour with increasing lag time. The MSD is low and almost independent of time for higher sample ages and concentrations because of the constraining effects of the stiff gels. The distribution of the particle displacements is Gaussian at small ages and low concentrations but become less Gaussian as age and concentration increase. The correlation analysis of the particle displacements shows that at small ages and low concentrations the motion of the particles is random, while at higher ages and concentrations there is a negative correlation between successive

displacements due to the constraining effects of the fluid structure. However we observed no deviation from the negative correlation for large step size and so the length scale of the fluid structure could not be determined.

Our results show that laponite at small ages and low concentrations is a homogeneous Newtonian fluid on the length scale of the probe particles. The change from subdiffusive to diffusive behaviour at intermediate sample ages and concentrations may be an indication of the sol-gel transition. At higher sample ages and concentrations, the suspensions gel and the fluid becomes more heterogeneous on the length scale of the probe particles. The absence of a characteristic length scale in the correlation analysis may be an indication of the fractal structure of laponite gels.

6.4 Future Work

This work has been centered on investigating the microstructure of the fluids, but in order to relate the bulk properties to the microstructure, we need to extract the bulk parameters from our data. This can be done by using the two-point microrheology technique which involves analyzing correlations between the trajectories of different particles [15]. We will also measure the bulk properties using a conventional shear rheometer. The microscopic properties of the fluid depend on the length scale on which they are measured, and hence the size of probe particle used, so it would be of interest to use different particle sizes to see how the properties of the fluid vary. Individual particle trajectories will be examined to see how they compare with the

average behaviour of the fluid.

Bibliography

[1] M. Kroon, G. H. Wegdam, and R. Sprik, Phys. Rev. E **54**, 6541 (1996).

[2] B.F.Goodrich Company, *Thickening Properties* (April 1995).

[3] I. S. Sohn and R. Rajagopalan, J. Rheol. **48**, 117 (2004).

[4] T. G. Mason, K. Ganesan, J. H. van Zanten, D. Wirtz, and S. C.Kuo, Phys. Rev. Lett. **79**, 3282 (1997).

[5] R. G. Larson, *The Structure and Rheology of Complex Fluids* (Oxford University Press, New York, 1999).

[6] W. B. Russel, D. A. Saville, and W. R. Schowalter, *Colloidal Dispersions* (Cambridge University Press, Cambridge, 1989).

[7] G. Dietler, C. Aubert, D. S. Carnnell, and P. Wiltzius, Phys. Rev. Lett. **57**, 3117 (1986).

[8] M. T. Valentine, P. D. Kaplan, D.Thota, J. C. Crocker, T. Gisler, R. K. Prud'homme, M. Beck, and D. A. Weitz, Phys. Rev. E **64**, 061506 (2001).

[9] F. C. MacKintosh and C. F. Schmidt, Curr. Opin. Coll. Interf. Sci. **4**, 300 (1999).

[10] M. J. Saxton, Biophys. J. **64**, 1766 (1993).

[11] M. P. S. Hong Qian and E. L. Elson, Biophys. J. **60**, 910 (1991).

[12] M. J. Saxton and K. Jacobson, Annu. Rev. Biophys. Struct. **26**, 373 (1997).

[13] M. L. Gardel, M. T. Valentine, J. C. Crocker, A. Bausch, and D. A. Weitz, Phys. Rev. Lett. **91**, 158302 (2003).

[14] I. Y. Wong, M. L.Gardel, D. R. Reichman, E. R. Weeks, M. T. Valentine, A. R. Bausch, and D. A. Weitz, Phys. Rev. Lett. **92**, 178101 (2004).

[15] J. C. Crocker, M. T. Valentine, E. R. Weeks, T. Gisler, P. D. Kaplan, A. G. Yodh, and D. A. Weitz, Phys. Rev. Lett. **85**, 888 (2000).

[16] V. Breedveld and D. J. Pine, J. Mater. Sci. **38**, 4461 (2003).

[17] E. R. Weeks and D. A. Weitz, Chem. Phys. **284**, 361 (2002).

[18] P. Habdas and E. R. Weeks, Curr. Opin. Coll. Interf. Sci. **7**, 196 (2002).

[19] Y. Tseng, T. P. Kole, and D. Wirtz, Biophys. J. **83**, 3162 (2002).

[20] M. J. Saxton, Biophys. J. **70**, 1250 (1996).

[21] M. J. Saxton, Biophys. J. **66**, 394 (1994).

[22] J. P. Bouchaud and A. Georges, Phys. Rep. **195**, 127 (1990).

[23] R. Metzler and J. Klafter, Phys. Rep. **339**, 1 (2000).

[24] Y.-C. Liu, Q. Wang, and L.-H. Lu, J. Chem. Phys. **120**, 10728 (2004).

[25] G. P. Roberts and H. A. Barnes, Rheol. Acta **40**, 499 (2001).

[26] J. O. Carnali and M. S. Naser, Coll. Polymer Sci. **270**, 183 (1992).

[27] C.-X. Lin and S.-Y. Ko, Int. Commun. Heat Mass Transf. **22**, 157 (1995).

[28] G. Lu and H. W. Jun, Int. J. Pharm. **160**, 1 (1998).

[29] A. Ramirez, M. J. Frenso, M. M. Jimenez, and E. Selles, Pharmazie **54**, 531 (1999).

[30] K. Edsman, J. Carlfors, and K. Harju. Int. J. Pharm. **137**, 233 (1996).

[31] M. J. Hernández, J. Pellicer, J. Delegido, and M. Dolz, J. Disper. Sci. Tech. **19**, 31 (1998).

[32] J.-Y. Kim, J.-Y. Song, E.-J. Lee, and S.-K. Park, Coll. Polym. Sci. **281**, 614 (2003).

[33] S. J. Curran, R. E. Hayes, A. Afacan, M. C. Williams, and P. A. Tanguy, J. Food Sci. **67**, 176 (2002).

[34] F. Pignon, J.-M. Piau, and A. Magnin, Phys. Rev. Lett. **76**, 4857 (1996).

[35] D. Bonn, H. Kellay, H. Tanaka, G. Wegdam, and J. Meunier, Langmuir **15**, 7534 (1999).

[36] B. Abou, D. Bonn, and J. Meunier, Phys. Rev. E **64**, 021510 (2001).

[37] M. Kroon, W. L. Vos, and G. H. Wegdam, Phys. Rev. E **57**, 1962 (1998).

[38] N. Willenbacher, J. Coll. Interf. Sci. **182**, 501 (1996).

[39] D. Bonn, H. Tanaka, G. Wegdam, H. Kellay, and J. Meunier, Europhys. Lett. **45**, 52 (1998).

[40] J. D. F. Ramsay, J. Coll. Interf. Sci. **109**, 441 (1986).

[41] D. J. Amit, Y. Verbin, and R. Tzafriri, *Statistical Physics, An Introductory Course* (World Scientific, New Jersey, 1999).

[42] M. F. Sclesinger, J. Klafter, and G. Zumofen, Am. J. Phys. **67**, 1253 (1999).

[43] P. Nakroshis, M. Amoroso, J. Legere, and C. Smith, Am. J. Phys. **71**, 568 (2003).

[44] F. Reif, *Fundamentals of Statistical and Thermal Physics* (McGraw-Hill, New York, 1965).

[45] J. C. Crocker and D. G. Grier, J. Coll. Interf. Sci. **179**, 298 (1996).

[46] L. P. Faucheux and A. J. Libchaber, Phys. Rev. E **49**, 5158 (1994).

[47] R. Metzler, E. Barkai, and J. Klafter, Phys. Rev. Lett. **82**, 3563 (1999).

[48] M. J. Saxton, Biophys. J. **81**, 2226 (2001).

[49] M. J. Saxton, Biophys. J. **72**, 1744 (1997).

[50] M. J. Saxton, Biophys. J. **69**, 389 (1995).

[51] B. Schnurr, F. Gittes, F. C. MacKintosh, and C. F. Schmidt, Macromolecules **30**, 7781 (1997).

[52] A. Klemm, R. Metzler, and R. Kimmich, Phys. Rev. E **65**, 021112 (2002).

[53] F. Amblard, A. C. Maggs, B. Yurke, A. N. Pargellis, and S. Leibler, Phys. Rev. Lett. **77**, 4470 (1996).

[54] M. J. C. Fresno, A. D. Ramirez, and M. M. Jimenez, Euro. J. Pharm. Biopharm. **54**, 329 (2002).

[55] *Neutralizing Carbopol and Pemulen Polymers in Aqueous and Hydroalcoholic Systems*. Tech. Rep. TDS-237, Noveon (1998).

[56] D. Solomonidou, K. Cremer, M. Krumme, and J. Kreuter, J. Biomater. Sci. Polym. Educ. **12**, 1191 (2001).

[57] `http:// www.laponite.com`.

[58] R. G. Avery and J. D. F. Ramsay, J. Coll. Interf. Sci. **109**, 448 (1986).

[59] G. Birk, *Instrumentation and Techniques for Fluorescence Microscopy* (Wild Leitz Australia Pty. Limited, Sydney, 1984).

[60] D. L. Taylor and E. D. Salmon, *Methods in Cell Biology* (Academic Press Inc., San Diego, 1989).

[61] F. W. D. Rost, *Fluorescence Microscopy*, vol. 1 (Cambridge University Press, Cambridge, 1992).

[62] http://www.dukescientific.com.

[63] http://www.fishersci.ca.

[64] http://www.scprod.com.

[65] http://www.sigmaaldrich.com/Area_of_Interest/The_Americas/Canada.html.

[66] http://www.surgipath.com/catalog/index.htm.

[67] http://www.dowcorning.com/applications/product_finder.

[68] http://sine.ni.com/apps/we/nioc.vp?cid=11352&lang=US.

[69] http://www.physics.emory.edu/∼weeks/idl/index.html.

[70] http://www.rsinc.com/idl.

[71] D. S. Martin, M. B. Forstner, and J. A. Kas, Biophys. J. **83**, 2109 (2002).

[72] H. G. Kirksey, J. Chem. Educ. **65**, 1091 (1988).

[73] W. K. Kegel and A. van Blaaderen, Science **287**, 290 (2000).

[74] A. Rahman, Phys. Rev. **136**, A405 (1964).

[75] B. Doliwa and A.Heuer, Phys. Rev. Lett. **80**, 4915 (1998).